芝浦工業大學
SHIBAURA INSTITUTE OF TECHNOLOGY

GLOBAL MAXIMUM POWER POINT TRACKING UNDER SHADING CONDITION AND HOTSPOT DETECTION ALGORITHMS FOR PHOTOVOLTAIC SYSTEMS

a Thesis Submitted to the
GRADUATE SCHOOL OF ENGINEERING AND SCIENCE
SHIBAURA INSTITUTE OF TECHNOLOGY

by

JIRADA GOSUMBONGGOT
Student ID: na17505

in Partial Fulfillment of the Final Defense
for the Degree of

DOCTOR OF PHILOSOPHY

SEPTEMBER 2020

Acknowledgements

First of all, I would like to express my gratitude to my supervisor Professor Goro Fujita for his enthusiastic guidance, helpful advice, and technical supports throughout my research. Without his motivation and instructions, the thesis would have been impossible to be done effectively.

I would like to place my sense of gratitude to Japan International Cooperation Agency (JICA) for supporting the scholarship. Additionally, I would like to thank Thai-Nichi Institute of Technology (TNI) for all supports during the doctoral degree course.

My sincere thanks also go to the thesis committee, professors and doctoral degree colleagues for their great feedback to improve this thesis; also, with the help of all Power Systems Laboratory members.

With great friendship, I would like to thank all of my friends who encourage me throughout this journey; especially my two best friends, Nuey and Xiu.

The most important; to Gosumbonggot's family, my parents Weerapan, Jaruwan and my sister Jan. The achievement I received belongs to you.

JIRADA GOSUMBONGGOT

September 2020

Abstracts

Renewable energy becomes an emerging trend in many countries. Photovoltaic (PV) technology has been gaining an increasing amount of attention due to unlimited power resources, unpolluted operation, and installation flexibility. Irradiation and temperature are the two main factors which impact on PV system performance. Diminishing of irradiation from weather conditions reduces the generated power. Shading also reduces the efficiency of the maximum power point tracking system by distributing non-uniform irradiation, leading to more than one power peak on the PV characteristic curve.

Designing the effective maximum power point tracking algorithm is a promising solution for enhancing the efficiency of the PV system. To overcome the problem of the multiple power peaks existence, the solution is to locate the local and global maximum power points in the characteristic curve. Therefore, the proposed algorithm is designed to track accurate global MPPT under shading conditions. The algorithm is distributed into three parts, (1) the Main Program (2) Shading Detection and Irradiance Estimation, and (3) Global MPPT using Slope Calculation. Details of the algorithm are shown by the full mathematical equations. The performance is verified by the simulation tests with the real weather data. Graphical and numerical results from the dynamic case study prove the effectiveness of tracking time within 3.40 seconds and the accuracy of 98.62%. Also, the long-term test results show an accurate tracking result, and the system can enhance the total energy generated by 8.55% compared to the conventional scanning method. The experimental test using the DC-DC boost converter proves the success of the proposed algorithm.

In consequence of partial shading, a problem of the hotspot is investigated. Hotspot takes place with the mismatch in the irradiation of the cells in the PV module. Under this condition, the unshaded part of the module operates at a current level higher than the shaded cells. As a result, the affected cells start to dissipate power leading to an increase in the temperature. Hotspot reduces performance and brings damage to the PV module. Conventionally, the detection uses the infrared camera to detect the hotspot; however, the high cost and workforce are necessary.

The algorithm is designed based on the simplified PV module structure, before improving by the practical PV cluster model. The method uses the concept of characteristic curves analysis and the rate of current changes under reversed bias condition to detect the hotspot. Apart from detection, the algorithm presents the status indicator to show the PV system's status after detection completes. Not only detecting the hotspot but the proposed algorithm can also differentiate the hotspot from the shading conditions. The proposed method provides collaboration between the detection and proposed global MPPT into one system. The implementations in different cases, including sizing, irradiation levels, and defection rates, prove the efficiency of the hotspot detection algorithm. Results confirm the performance of the proposed algorithm, showing the accuracy with fast detection. Furthermore, the discussion of temperature estimation is shown for representing the potential step after detecting the hotspot, also providing further understanding of the thermal model from material science's perspective.

Contents

List of Figures

List of Tables

List of Abbreviations

Acronyms

Symbol	Description
AC	Alternative current
ANN	Artificial Neural Network
AWIPSO	Adaptive Inertia Weight Particle Swarm Optimization
DC	Direct Current
DSP	Digital signal processor
GMPPT	Global Maximum Power Point Tracking
I-V	Current-Voltage
IEC	International Electrotechnical Commission
InC	Incremental Conductance
JPY	Japanese Yen
MOSFET	Metal-Oxide-Semiconductor Field-Effect Transistor
MPP	Maximum Power Point
MPPT	Maximum Power Point Tracking
P-V	Power-Voltage

P&O	Perturb and Observe
PC	Personal Computer
PSO	Particle Swarm Optimization
PV	Photovoltaic
PWM	Pulse Width Modulation
SEPIC	Single-Ended Primary-Inductor Converter
SLIC	Simple Linear Iterative Clustering
STC	Standard Test Condition

Subscripts

Symbol	**Description**
γ	Shading ratio
a	Diode Ideality Constant
A_{HS}	Sizing of the defected area
C_{TH-HS}	Thermal capacitance of the defected area
C_{THcell}	Thermal capacitance of the defected area
d	Duty Cycle
$D_{REF[k]}$	Duty cycle reference point
G	Solar Irradiation
G_{irr}	Solar irradiation of the PV cell
G_n	Nominal Solar Irradiation
I_{MPP}	PV module's current at the maximum power point
I_{ph}	PV's current source

$I_{PV,STC}$	PV's current at standard test condition
I_{PV}	PV's current
I_{SC}	PV module's short-circuit current
K_I	Temperature coefficient of the PV's current
K_V	Temperature coefficient of PV's voltage
M	Number of PV string in the array
m	PV's hotspot slope coordinate index
N	Number of series-connected PV modules
P_{DIFF}	Ratio of power difference
P_{LOCAL}	Local Power Peak
$P_{REF[k]}$	Power tracking reference point
R_p	PV's parallel resistor
R_s	PV's series resistor
R_{lr}	PV's hotspot small resistor
R_{TH-HS}	Thermal resistance of the defected area
R_{THcell}	Thermal resistance of the whole cell area
$Slope[m]$	Calculated slope of each coordinate pair
T_{amb}	Ambient temperature
T_{HS}	Temperature of the defected area
T_{STC}	Temperature at standard test condition
$V_{OC,STC}$	PV module's open-circuit voltage at standard test condition
V_{OC}	PV module's open-circuit voltage

V_O	Load Voltage
V_T	PV's voltage constant

Chapter 1

Introduction

1.1 Introduction to the Photovoltaic System

Renewable energy is currently at the main concern in the less carbon-intensive situation. The installation of renewable energy systems such as photovoltaic, wind, and bioenergy has grown rapidly in recent years. Due to the expansion, researches in renewable energy have been received great attention, especially in the past ten years.

Renewable power lead by photovoltaic (PV) technology has gained popularity as one of the potential avenues. PV's expansion increases due to unlimited power resources from the sunlight and unpolluted operation with no emission. Moreover, the technology is also capable to use in wide ranges of applications for both residential and commercial infrastructures, providing energy to the areas where the grid is difficult to access. According to the report by the International Energy Agency (IEA) [1], in 2017 the cumulative PV capacity reaches approximately 398 GW and generated over 460 TWh. The calculation represents the ratio of 2% of PV generation over the global power output. PV is expected to lead the growth of renewable electricity capacity and to reach 580 GW over the next five years. Figure 1.1 shows the graph of solar PV generation and cumulative capacity by region, which occurs between 2017 and 2023.

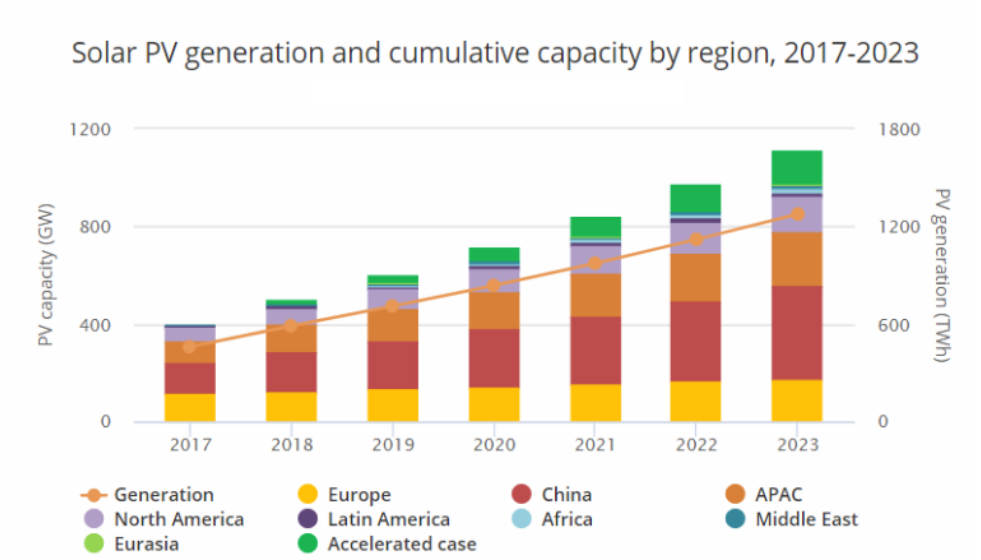

Figure 1.1: PV generation and cumulative capacity by region from 2017 to 2023 [1]

Focusing on Japan, the country continues to move toward a low-carbon society. Reported by New Energy and Industrial Technology Development Organization [2], PV cell production has increased significantly at the annual rate of 30%-50% since 2003. Japanese government continuously supports the PV installation on large-scale, commercial and residential areas since 2009. Furthermore, Asian Insider [3] reports that Japan's renewable energy will increase to approximately 40 % in 2030 compared to 2017. Observing the status of each power generation facility, PV is planned to be increased by approximately 25 GW, from 39.1 GW of 2017 to 64 GW of 2030, and further expanding the market size is expected. The statistic data supports the potential of PV as a strong rebound in renewable capacity additions.

1.2 Basic Principle of the Photovoltaic System

Researches in renewable energy receive great attention. Since PV has dynamic performance depending on the weather condition, it is vital to understand how

PV operates. In fundamental, PV can generate electricity using the photon from sunlight. As the photon knocks the electron inside the Silicon layers inside the PV cell, the electric field will push that electron out of the Silicon junction [1]. The generated power from the PV has a proportional relationship to the solar irradiation level; the more irradiation incidents to the PV cell, the higher the generated power can achieve.

The main electrical characteristics of PV cell are represented by the current, voltage, and power, in the form of PV's current-voltage (I-V) and power-voltage (P-V) characteristic curves. Figure 1.2 presents the example of I-V and P-V curves under different irradiation and temperature conditions.

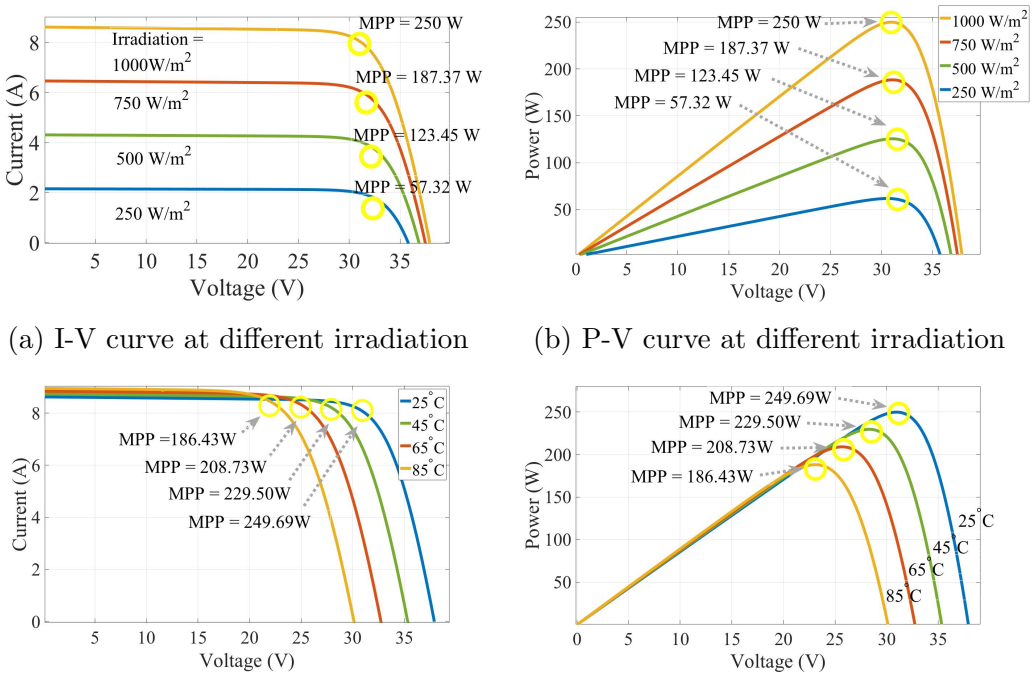

(a) I-V curve at different irradiation (b) P-V curve at different irradiation

(c) I-V curve at different temperature (d) P-V curve at different temperature

Figure 1.2: Example of the I-V and P-V curves at different irradiation and temperature

The highlighted circles indicate the maximum power point (MPP) for each condition. The condition includes the power at standard test condition (STC) (under

1000 W/m^2 of the irradiation and 25 °C of the temperature), and at other levels shown.

As shown in figure 1.2, the irradiation and temperature have an impact on the PV's output power. From figures 1.2(a) and 1.2(b), each irradiation (consists of 250, 500, 750 and 1000 W/m^2) presents the different levels of generated power in a directly proportional relationship. On the other hand, figures 1.2(c) and 1.2(d) present the temperature impact on the PV's performance. The curves present the reduction of PV's voltage when the temperature keeps increasing, in consequence, the generated power decreases. Because the suitable irradiation and temperature are available on short-timescales and depend on the weather conditions, it is important to investigate the enhancement of PV to achieve its highest potential.

1.3 Problem Statements

In this thesis, the considered problems related to the PV system are divided into two main points.

The first problem is how to determine the maximum power when the PV system operates under partial shading conditions. As stated in section 1.2, the irradiation and temperature are the two main parameters that affect the PV-generated power [4]. If shading from the environment or surroundings occurs on the PV panel's surface, not only the generated power reduces, shading also increases the difficulty level for the system to track the accurate maximum power. Figure 1.3 shows the example of characteristic curves under no shading and partial shading conditions.

From figure 1.3(a), if the irradiation across the PV array is equal and uniform, the curve shows one maximum power point and capable for normal maximum power point tracking (MPPT) system to locate. However, as shown in figure 1.3(b), when there's the non-uniform irradiation occurs across the array, the curve then shows more than one maximum power points. Because of this, the normal MPPT could not confirm the accuracy to allocate the correct maximum

power. Therefore, this thesis focuses on the analysis and design of the MPPT algorithm under shading conditions with high efficiency and low cost.

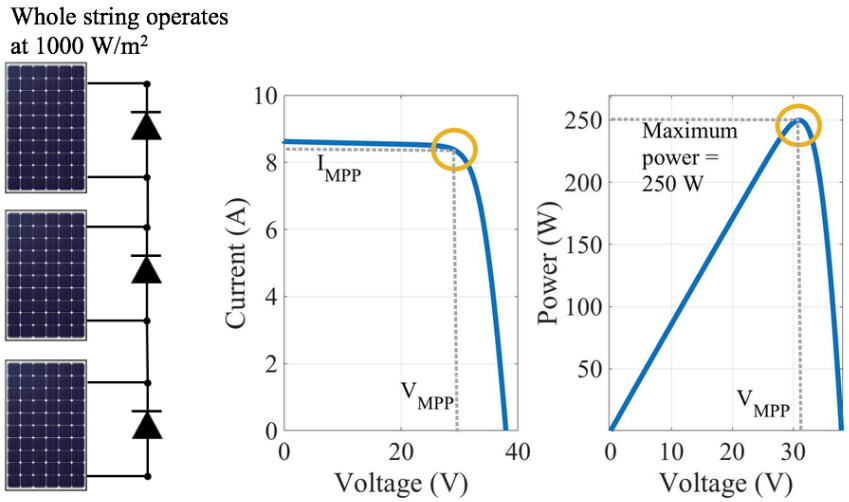

(a) Characteristic curves at no shading condition

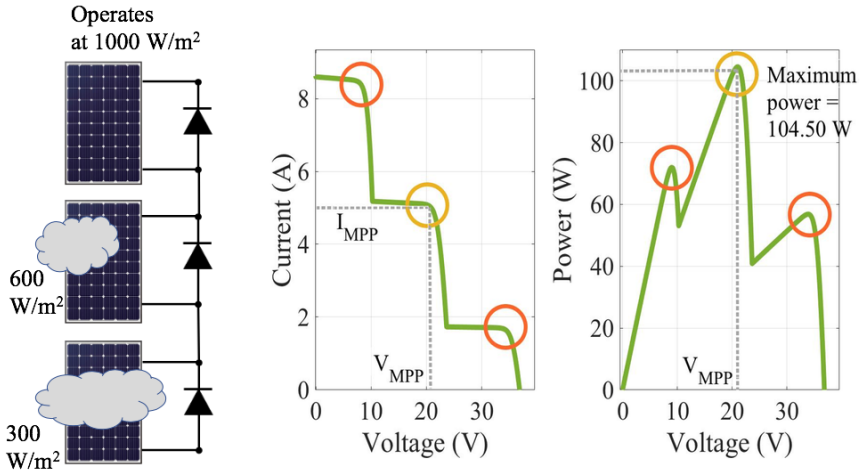

(b) Characteristic curves at partial shading condition

Figure 1.3: Example of the characteristic curves during no shading and partial shading conditions

The second problem is how to detect the occurrence of the hotspot on the PV panel. The hotspot is defined as the fault formed on the panel's

surface due to the high temperature, which happens from the consequence of shading on the PV panel's surface. Mentioned in IEC 61215 (the universal standard stated the design qualification and type approval of the manufactured PV module), the main cause of hotspot occurs when a PV cell's operating current exceeds the level of short-circuit current of normal condition cells [5]. The exceeded current induces the temperature in a cell, later on, reduces the generated power.

With clear observation, the form of hotspot presents as the burnt on the PV cell surface. Figure 1.4 shows the example of the hotspot on the PV panel's surface [6].

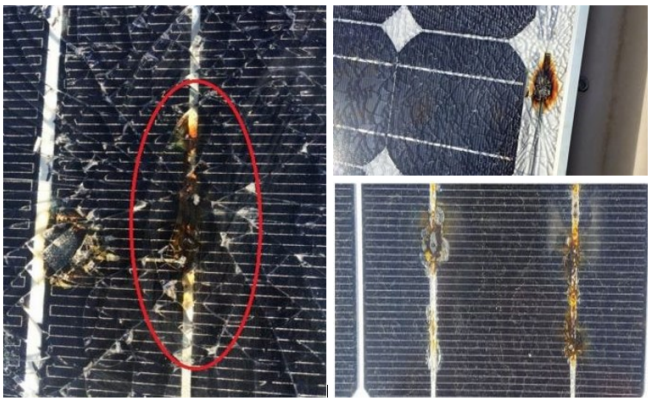

Figure 1.4: Example of the hotspot presence on the PV panel's surface [6]

Although IEC 61215 states the cause of hotspot and the testing standard of the manufactured panels, the standard does not specify the proper hotspot detection method. In the conventional process, the hotspot is detected using the infrared camera, which captures the thermal image of the hotspot. The captured result shows the acceptable detection accuracy; however, the main disadvantages include the high equipment cost and workforce. The hotspot is also considered as the hidden fault, which can reduce the generated power level of the PV system. In a real installation, the hotspot generally decreases the system's efficiency, shown by the performance ratio. The statistical data of the hotspot existence in PV site is shown by case studies and surveys [7, 8]. According to the effect of the hotspot, it is important to analyze the effects and design of the method to detect the

hotspot in the PV system. The model should be capable of the existed practical PV model.

1.4 Study Contributions

Study contributions arranged by chapters are shown as follows;

1. *Chapter 2: Partial Shading Detection and Global Maximum Power Point Tracking Algorithm for Photovoltaic with the Variation of Irradiation and Temperature.*
   This chapter presents the analysis of partial shading towards the different specifications of PV array. The main contributions consist of the proposed mathematical expressions for detecting the occurrence of shading and irradiation estimation. The ideas do not require either the irradiation sensor or the historical weather data, making the simple implementation. The proposed MPPT algorithm uses the concept of slope calculation on the PV characteristic curve. The method provides the accuracy for tracking the maximum power under shading conditions, with fast response and simple implementation.

2. *Chapter 3: Simplified Hotspot Model and Proposed Hotspot Detection Algorithms for Photovoltaic Systems.*
   In this chapter, the hotspot detecting algorithm is proposed. The algorithm is integrated with the proposed MPPT method in chapter 2, contributing not only to the algorithm's performance to track the maximum power but also it can accurately identify whether the hotspot is present in the PV system. The implementation in several hotspot cases confirms the effectiveness of the detection method.

3. *Chapter 4: Hotspot Model in Cluster's Structure with Hotspot Detection Algorithms and Temperature Estimation for Photovoltaic Systems.*
   This chapter presents a more detailed analysis of PV cell scale on the power dissipation of the hotspot. The detail shows the improvement of the hotspot

detection algorithm in chapter 3 to make the functional level compatible with the practical PV model. The chapter contributes to the successful hotspot detection in different weather scenarios. The improved method presents higher efficiency, which shows more compatibility with the practical PV module's structure.

1.5 Thesis Outline

In order to answer the questions stated in the problem statement, this research is divided into topics which arranged in chapters format. The followings are the outline of this thesis.

- **Chapter 2: Partial Shading Detection and Global Maximum Power Point Tracking Algorithm for Photovoltaic with the Variation of Irradiation and Temperature.**
  The main objective of this chapter is to analyze the effect of partial shading on the PV system. The study of characteristic curves is used to design the tracking algorithm, mainly divided into three parts; the main program, shading detection and irradiation estimation, and global MPPT using slope calculation. This chapter starts with the problem statement in section 2.1, together with the literature review in section 2.2. Section 2.3 shows the characteristic curve's analysis use for implementing the slope calculation method. Afterward, the system's description and the full algorithm is presented in section 2.4. The system implementation and results are shown in section 2.5, in which the results are achieved from the simulation and experiment.

- **Chapter 3: Simplified Hotspot Model and Proposed Hotspot Detection Algorithms for Photovoltaic Systems.**
  This chapter presents a description of the hotspot in the PV system. The DC circuit model is used to represent the hotspot's characteristics in a PV module. The chapter begins with the problem statement in section 3.1, introducing the occurrence of the hotspot, the degradation to the PV system

proved by the survey data, and the standard. Details are followed by the literature reviews of the hotspot modeling techniques and detection methods, including the advantages and disadvantages discussion in section 3.2. In addition, section 3.3 shows the simplified hotspot's modeling method and fundamental analysis using the characteristic curves; following by section 3.4 for the proposed hotspot detection algorithm. The tests of the proposed method are performed in section 3.5.

- **Chapter 4: Hotspot Model in Cluster's Structure with Hotspot Detection Algorithms and Temperature Estimation for Photovoltaic Systems.**
  The main context of this chapter is to present the improvement of the hotspot model and detection algorithm to continue from chapter 3. The improved model shows more capability to match with the practical PV standard, importantly the IEC 61215. The chapter starts with section 4.1 for the problem statement. This section includes the explanation of the hotspot in reversed bias conditions with the involved challenges and factors result in the acceleration of the hotspot in PV system. The chapter continues with the analysis of the improved hotspot model in section 4.2. Consequently, the improved hotspot detection algorithm using inclined current changes calculation is shown in section 4.3. The system's implementation and results are presented in section 4.4, dividing into several cases. The chapter ends with the discussion of temperature estimation in section 4.5 for indicating the damage level of the hotspot.

- **Chapter 5: Conclusions and Future Works.**
  Section 5.1 concludes the studies and contributions in this thesis. The main future works include the extension works of the MPPT tracking algorithm, hotspot's damage level identification, and maintenance are shown in section 5.2.

Chapter 2

Partial Shading Detection and Global Maximum Power Point Tracking Algorithm for Photovoltaic with the Variation of Irradiation and Temperature

Global climate change is considered as the biggest problem facing humanity. Dealing with climate change, clean energy technologies have been studied and developed to reduce pollution and protect the environment. Photovoltaic (PV) technology, as one of the renewable energy sources, achieves great interest especially in this decade due to the nonpolluting operation and good installation flexibility. There are various types of installation differ in size and location; starting from residential areas, commercial and industrial sectors, then expand to utility-scale for providing the electrical power.

To enhance the efficiency of PV, the effect of weather condition must be considered. There are two main parameters which affect the PV-generated power, irradiation and temperature; varies from location where the PV is installed. Since it is not possible to control these two parameters, the generated power then differ

from the expected value; therefore, the problem of **PV mismatch** can occur. It also causes the difficulties for PV system to generate the maximum potential power. In this chapter, the mismatch by external factor mainly the changes of irradiation and temperature from surroundings is the main consideration. Hence, it is necessary to determine the solution to enhance the efficiency of the PV system when operating during changes of irradiation and temperature. Researches explain the effect of mismatch towards the PV system that significant power losses occur if the maximum power is not tracked accurately [9, 10, 11, 12].

Published works also verify that the conventional MPPT methods cannot ensure successful and precise of the maximum power under changes of irradiation and temperature [13, 14, 15, 16]; consequently, the difficulties in implementing MPPT still exist. The challenges include the complexity of the algorithm, cost, and failure while operating in shading conditions [17]. Therefore, the preferences of the proposed method are to achieve the tracking method with high tracking accuracy, less power loss, simple and low cost.

The main objective of this chapter is to propose the new global MPPT under shading conditions, with the simple concept of searching the mountain's peak. The expected results consist of accurate global MPP in various irradiation and temperature conditions. Also, a further objective is to evaluate the performance of the proposed method under different weather conditions with real weather data. From the short and long term testing results, the proposed method can locate the maximum power in various irradiation and temperature conditions. This chapter proposes the original idea of characteristic curves studies to design the new MPPT method, representing in algorithm format. The algorithm mainly consists of three parts **(1) the main program (2) Shading Detection and Irradiation Estimation and (3) Global MPPT Using Slope Calculation.** The highlighted point is the proposed algorithm uses the simple concept of mountain climbing to search the mountain's peak, to locate the local and global power peaks without searching through the whole curves. This idea is new and has not been shown in other papers.

This chapter is outlined as follows. Firstly, section 2.1 states the problems of PV mismatch partial shading towards the PV system; continuing with the

literature reviews of selected published works about the global MPPT in section 2.2. Moreover, section 2.3 describes the analysis of the PV model and its characteristic curves, with section 2.4 presents the system‘s model, the proposed global MPPT algorithm and implementation details. For the results, section 2.5.1 shows the simulation results tested by dynamic, short-term and long-term cases; with section 2.5.2 presents the experimental results. Finally, the analysis in grid-connected system is shown in section 2.5.3.

2.1 Problems Statement

Stated in the introduction, shading causes significant power losses for the installed PV system. For example, studies by [11] show the practical case study through the PV rooftop systems installed in Germany. The installed panels had been affected by shading at 41%, with energy losses up to 10%. Hence, remarkable reduction of power generated is observed. In additional, research by [12] presents a case study of 13 different PV's power tracking systems operating under a shading condition, where the result shows up to 70% of power is a loss due to not detecting the correct maximum power.

As explained in section 1.2, electrical characteristic of PV cell can be modeled as the non-linear relationship of the I-V and P-V characteristic curves. In the case of PV mismatch, due to shading condition, more complexity can be observed using the characteristic curves. Figures 2.1(a) and 2.1(b) present the series-connected PV array with the bypass diodes. The standard test condition (irradiation of 1000 W/m^2 and temperature of 25 °C) is assigned for figure 2.1(a), while the partial shading with different irradiations level is assigned for figure 2.1(b). The P-V characteristic curve corresponding to each condition is shown in figure 2.1(c).

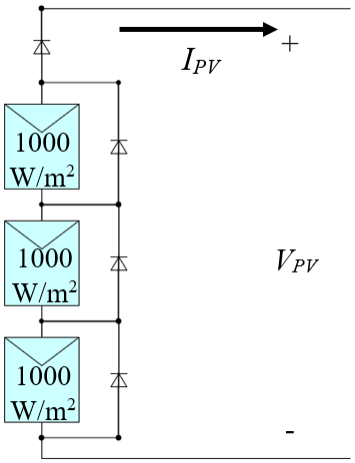

(a) PV array at normal irradiation at 25 °C

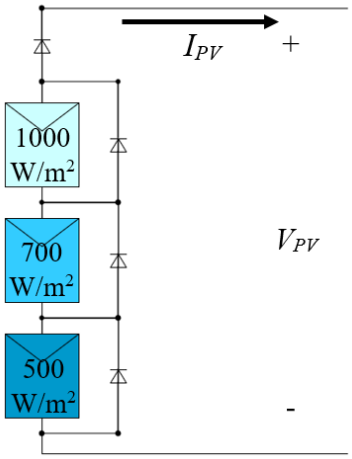

(b) PV array at partial shading condition at 25 °C

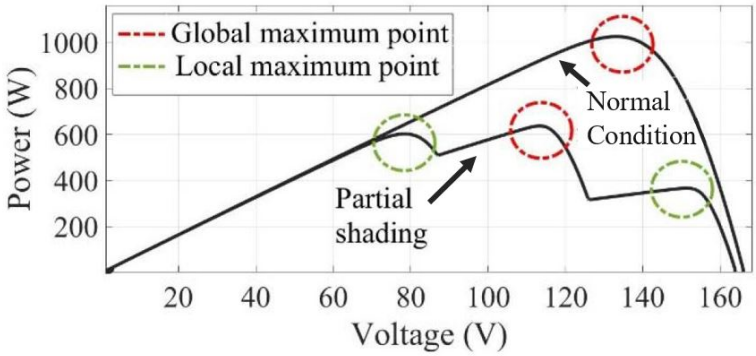

(c) P-V characteristic curves for normal and partial shading condition

Figure 2.1: Example P-V characteristic curves for normal and partial shading condition

We can observe the significant difference between the two conditions from the curve. From the mismatch of irradiations in the array, clearly by observation, shading exhibits three maximum power points aligned in different PV's voltage values, while the normal condition distributes only a unique maximum power point. From figure 2.1(c), the partial shading distributes three peaks while the highest is at approximately 630 W, compare to the normal condition with the

highest power of 1020 W.

In this chapter, the highest maximum power of the entire P-V curve at each irradiation and temperature is called as the **global maximum power point (Global MPP)** [18, 19, 20]. With more than one MPP in the curve, the challenge raises for the MPPT system to track and indicate the highest power that PV array generates. Supported by Patel and Agrawal [4], irradiation and temperature are the two main parameters which affect the PV-generated power. It is obvious we cannot control the two aforementioned parameters. For example, the generated power cloudy day is found less than the sunny day due to lower irradiation level from blockage of the cloud. In additional, the heavy rain and snow are significantly reduce the generation. As majority of the commercial PV inverter, the programmed MPPT algorithm embedded to the system does not have the function to support the MPPT under shading condition. In this case, the research of the MPPT algorithm under shading condition has become the interest for researchers and engineers. The designed algorithm named Global Maximum Power Point Tracking (Global MPPT) is used to emphasis the MPPT method that the MPPT is designed to track the highest power of the PV system according to the irradiation and temperature levels.

2.2 Literature Reviews

Mentioned in section 1.1, as the PV system receives great attention, researches in MPPT have been shown especially in the last decade. There are several proposed algorithms published. Mainly the algorithm can be distinguished into two categories, differentiated based on the method of implementation.

2.2.1 First Category: Conventional MPPT Algorithms with Modifications

The first category originates from the improvement of the existing conventional tracking method; these include the well-known MPPT techniques but with

further modification. The algorithm is designed based on the existing conventional MPPT with modifications. The conventional MPPT techniques include the perturb and observe (P&O) and incremental conductance (InC) . Research works propose the effectiveness of the first category methods in order to locate the correct global MPP [21, 22, 23].

Work performed by [24] introduces the conventional scanning method, which is one of the classical MPPT algorithms. The fundamental concepts for scanning are to scan through the whole P-V characteristic curves starts from zero to the PV's total open-circuit voltage (V_{OC}). By searching at the whole range of PV's voltage, the scanning has high global MPP locating accuracy. Figure 2.2 presents the conventional scanning for the example P-V characteristic curve.

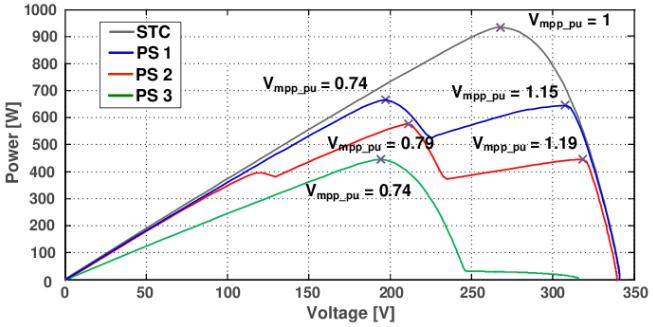

(a) Example of the P-V curves under partial shading

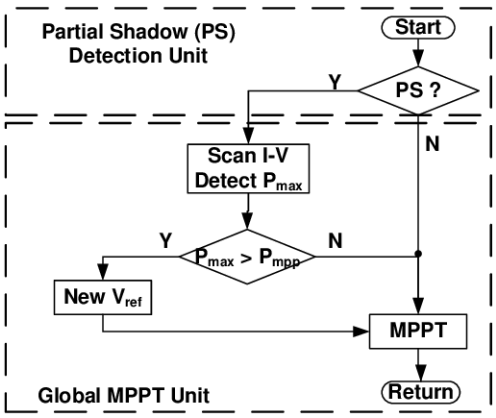

(b) Proposed scanning algorithm flowchart

Figure 2.2: Example of the conventional scanning algorithm reported in [24]

The algorithm uses the scanning method to scan the curve periodically to the curve in order to track the global MPP. Although the algorithm is capable to track the power, the drawbacks still occur. The main disadvantages of conventional scanning include

1. **Processing time consumption**: Since scanning requires every value sampling from the P-V curve in the whole voltage region, based on the sampling rate, many sampling data are necessary. The smaller the sampling rate, the more accuracy achieves. In this case, the algorithm requires more processing time to record the sampling data, also causes more tracking time.

2. **Loss of power during tracking**: Also, the consequence of the time consumption, whenever the algorithm tracks the power, there is a small quantity of power loss. This disadvantage is considered to be a minor for short-term tracking. However, for the long-term (in this case, whole operating day) small power loss can combine into the significant power loss.

3. **Mismatch scanning period setup in different weather conditions**: According to the technical specification of PV inverters, scanning is set to be every 15 minutes of the time interval [25, 26]. The mismatch setup interval is not matched with all types of weather conditions. By choosing a long scanning interval on the day with the rapid change of weather, tracking error may occur due to the mismatch of the selected interval. Additionally, by choosing a short scanning interval on the day with a steady change of irradiation and temperature, the power loss from the unnecessary tracking is achieved.

Apart from conventional scanning, researches propose global MPP algorithms using the improvement of the existing conventional tracking method. Research by Eftichios et al [11] shows how the global MPPT methods work by distributing PV load lines on the characteristic curve and reference points are indicated along these lines. The result shows the complete tracking results with higher efficiency compared with the PV scanning and particle swarm optimization (PSO) , which is one of the optimization methods that can be a solution for the optimization

problem using the concept modeled after bird folk's behavior. Nonetheless, the work does not provide the time response result, and the implementation requires additional switching circuits, such as a flip-flop and a comparator.

Another interesting research by Hiren [27] shows the algorithm by setting the threshold to detect changes of power when shading occurs. Also, using the change of power to determine tracking direction. The algorithm confirms the effectiveness; however, the results only present in the short-term (less than 30 seconds). The practical long-term result for more than 30 seconds which is more surreal to the practical PV system operating time is not indicated. Researches by Jubaer [28] discussed the disadvantage of the P&O algorithm due to its oscillating response when operating in rapid irradiation change. This paper proposes mathematical equations to detect power deviation, which is used together with the tracking algorithm. The drawbacks are the complexity in calculation due to many parameters and programming.

Further research by Korey [29] presents the global MPPT based on the P&O algorithm, experimented with three series-connected PV panels. The result shows successful tracking; however, it still contains the oscillation and the power generated quantity was not realized. Also, work developed by Kobayashi et al. [30] and Irisawa et al. [31], two-stage MPPT is proposed. Consists of the first stage, the PV's optimum operating point is controlled to converge the MPP; afterward, the second stage operates to move closer to the MPP. The idea still faces the accuracy problem when operating under some non-uniform irradiation conditions. Also, the implementation requires an additional control circuit.

Research by Bekker [32] shows the optimal MPPT algorithm using the open-circuit voltage sweep along the P-V characteristic curve, but the loss from track still exists. The method by Nguyen and Gules [33, 34] proposes the adaptive reconfiguration scheme and control topology for the bidirectional DC-DC converter to decrease the shading effect. Both methods confirm the success under real-time operation; however, the method requires additional hardware and sensors in proportion to the size of the PV array, increasing in the cost.

In conclusion from the reviews, the major drawbacks from the first category's

topology are the requirement of many parameters which is hard to determine; also the requirement of hardware and complexity of programming.

2.2.2 Second category : Intelligence MPPT Algorithms

The second category is topologies based on the intelligence computing method. Since 2015, artificial intelligence methods have been used to solve the MPPT problem under the shading condition. The popular methods include the fuzzy logic based MPPT, ANN , and PSO algorithm. Examples of published work include as follow;

Research by Yuan [35] proposes the adaptive inertia weight particle swarm optimization (AWIPSO) based on the original PSO method. The method has the flexibility to adjust weight coefficient parameters, which can increase the speed of tracking. The algorithm is confirmed using the simulation; however, the experimental results are not included. Works by [14] and [36] states the difficulties of PSO including calculation complexity for related variables, also setting precision and requirement of cooperative agents and learning factors. Similarly, the work by Miyatake et al. [18] implements the PSO based method to track the power. The drawback is the requirement of a separate converter per one PV module, causing more extra cost.

In addition, another intelligence method called fuzzy logic is also integrated with the MPPT. Proposed by Alajmi et al. [37], the research presents the modified fuzzy-logic controller. The design is based on a diode model equation of the PV panel, with the modified fuzzy-logic from the hill-climbing method. However, the system requires thirty-two fuzzy control rules, adding more complexity to the system.

It is observed from two reviewed topologies of the proposed global MPPT performed by several articles, the common disadvantages for both tracking categories are the requirement of additional circuits, complexity and implementation cost. The disadvantages become the gap which motivates the research in global MPPT under shading condition.

2.3 Analysis

2.3.1 Partial Shading Condition for PV Systems

An ideal PV module can be modelled as a single diode equivalent circuit [38]. Figure 2.3 shows the single diode equivalent circuit, including a current source I_{ph} connected antiparallel with a diode, a series resistor R_s and a parallel resistor R_p .

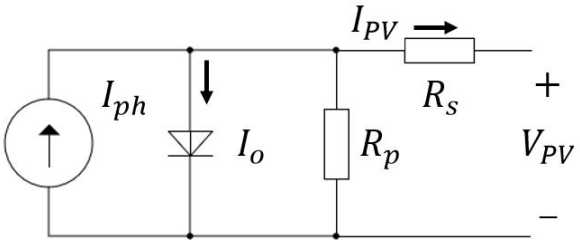

Figure 2.3: PV module equivalent circuit

Equation 2.1 represents the mathematical relationship between the PV module current I_{PV} and other related parameters [39].

$$I_{PV} = (I_{PV,STC} + K_I \Delta T)\frac{G}{G_n} \tag{2.1}$$

From equation 2.1, $I_{PV,STC}$ is the PV's current of the module in standard test conditions (STC) , K_I is the temperature coefficient of current , G is the solar irradiation measured in W/m^2 and G_n is the nominal solar irradiation (1000 W/m^2) .

The equation shows the directly proportional relationship between G and $I_{PV,STC}$ that the higher the irradiation, the more PV's current is measured. However, when irradiation decreases due to shading, the current reduces.

In addition, equation 2.2 represents the calculation of the PV module's open-

circuit voltage (V_{OC}) [27]:

$$V_{OC} = V_{OC,STC} + K_V(T - T_{STC}) + aV_T \ln(\frac{G}{G_{STC}}), \tag{2.2}$$

where $V_{OC,STC}$ is the PV module's open-circuit voltage at standard test condition, K_V is the temperature coefficient of voltage, T represents temperature and T_{STC} is the temperature at STC (25°C). Additionally, a is the diode ideality constant and V_T is voltage constant.

Equation 2.2 shows that the open-circuit voltage varies with both irradiation and temperature; by assuming the last term of the equation to be very small, the temperature level is the primary cause for the variation of PV's open-circuit voltage value. Likewise, both equations 2.1 and 2.2 explain that the operation of PV varies with irradiation and temperature [40].

2.3.2 P–V Characteristic Curve Analysis

From the review in section 2.2, conventional MPPT algorithms cannot confirm the global MPP tracking accuracy under shading conditions, contributes to the complexity in tracking the correct maximum point. In order to design an effective MPPT algorithm, more than 20 samples of P–V characteristic curves are analyzed. Figure 2.4 shows series-connected PV modules with different patterns of irradiation and temperature, specified as patterns A and B, where the temperature for each pattern is 25°C and 30°C, respectively.

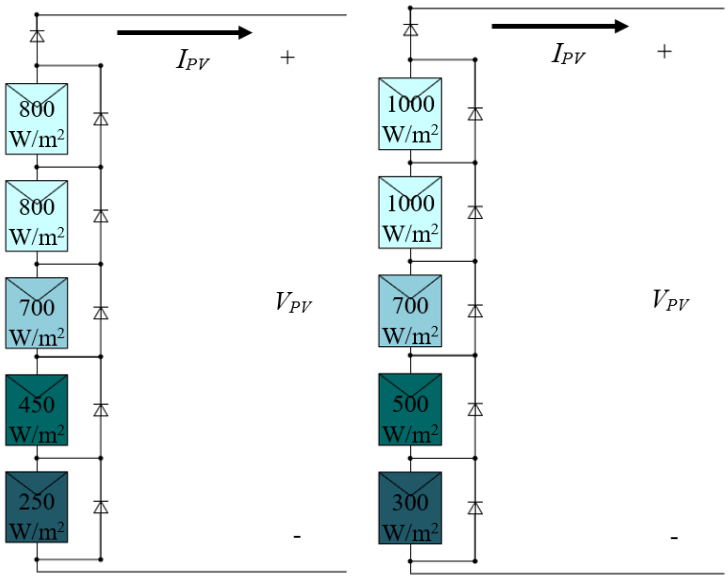

(a) Pattern A at 25°C (b) Pattern B at 30°C

Figure 2.4: Example of the case study patterns for P-V curve analysis

PV module's specifications from the manufacturer consist of Canadian Solar Cs5C-90M, Guelph, Canada; Trina Solar TSM-170D, Changzhou, China, and Jinko Solar JKM310M-72, Shanghai, China) using pattern A and B in figure 2.4. Studies can be distinguished into six cases. Figure 2.5 presents P–V curves in six cases with three different PV modules, varying the irradiation and temperature. The local and global MPPs exist in the highlighted searched regions.

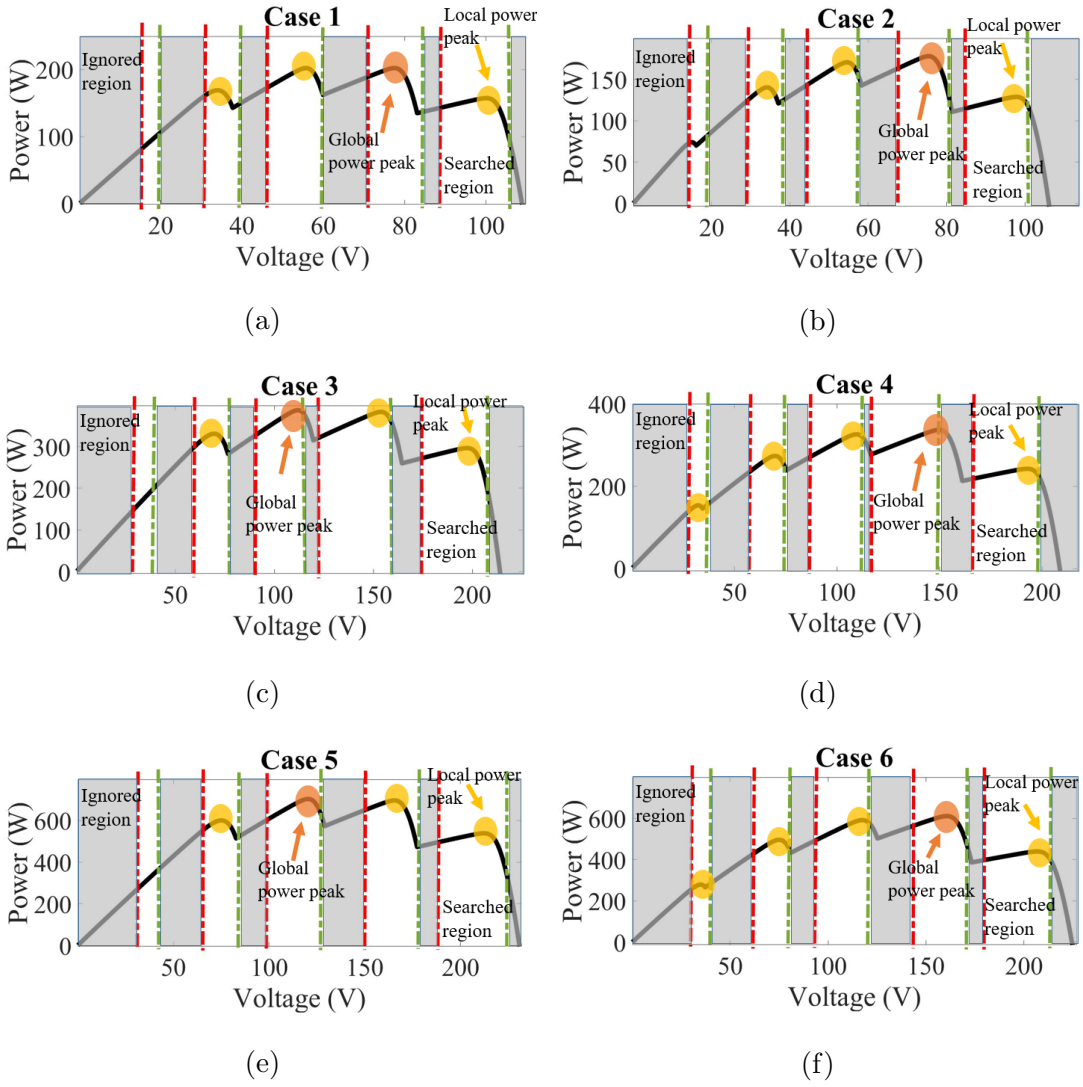

Figure 2.5: P–V characteristic curves for cases 1 to 6

The highlighted information obtained from the samples is that although the P–V curve has more than one maximum power point, each power peak, including local and global maximum points, exists at multiples of 70% to 85% of the PV module's open-circuit voltage (except for two rightmost sections of the curve, where the peak exists between 75% and 95%). Summarized information is shown in table 2.1.

Table 2.1: Summarized information of the P-V curve analysis cases 1 to 6

Case	PV module specification	Irradiation pattern	V_{OC} per module (V)
Case 1	Canadian Solar Cs5C-90M	A	22.20
Case 2		B	21.24
Case 3	Trina Solar TSM-170D	A	43.60
Case 4		B	41.72
Case 5	Jinko Solar JKM310M-72	A	47.10
Case 6		B	44.90

The value of V_{OC} per PV module at different temperatures is shown in table 2.1. The increase of temperature brings less measured V_{OC} , which verifies the explanation from equation 2.2. Therefore, the proposed algorithm should deal with the temperature changes since it causes effects to the PV's voltage. Continuously, although the location of global MPP varies in each pattern, the peaks still exist within the searched region (at approximate multiples of PV module's open-circuit voltage). Therefore, it is possible to estimate the searched region of the P-V curve. The information achieves from the analysis is combined and used to design the new global MPPT algorithm, shown in section 2.4.

2.4 System Description and Proposed Global MPPT Algorithm

2.4.1 System Description

Generally, for the PV system, a DC-DC converter is implemented together with the MPPT controller to control the input voltage and current from PV to reach its maximum power point. It is assumed that the PV system connects to the constant DC load voltage. In this section, the DC-DC boost converter is used to test the proposed method due to its robustness and simple switching control with only one duty cycle value (d). As for other converter topology (i.e., a buck-boost converter, single-ended primary-inductor converter (SEPIC)), the proposed algorithm can also be integrated; however, additional switching control

is required since the number of switches adds and the converter operates in both buck and boost mode. Figure 2.6 shows the basic block diagram of the PV system integrated with the boost converter [41, 42].

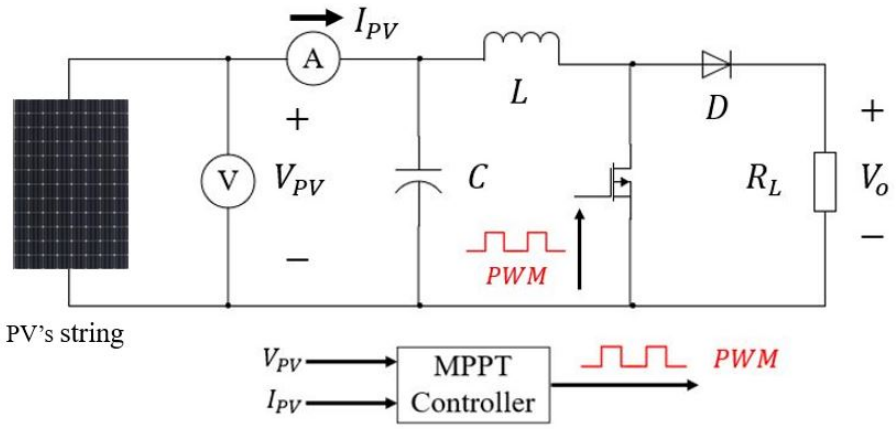

Figure 2.6: Basic PV system with the DC-DC boost converter

After measuring the PV's voltage and current, the MPPT controller determines the maximum power point according to the level of irradiation and temperature. By tracking, the controller outputs the duty cycle to control the PV system to operate at its maximum power. Equation 2.3 demonstrates the mathematical relations between PV voltage V_{PV}, load voltage V_O, and duty cycle d.

$$V_{PV} = (1 - d)V_O \tag{2.3}$$

From equation 2.3 d is used to generate the pulse width modulation (PWM) switching signal to control the MOSFET. The switching frequency of the tested PWM signal is set at 10 kHz. For the sampling period of the sensors and converter, the period must be set in the suitable ranges. If the setup is too small, it is unnecessary and may cause the slow system response for the converter to operate. On the other hand, if the sampling period is too large, the system does not have enough data from the sensors to track the accurate MPP and may cause the error. In the proposed system the sampling period should be set as approximately 0.1 ms, in order to achieve the high tracking efficiency.

2.4.2 Proposed Global MPPT Algorithm

Figure 2.7 shows the flowchart of the proposed global MPPT algorithm, describing how the proposed algorithm operates. The algorithm mainly divides into three parts; including (1) the main program (2) Irradiation Estimation and Shading Detection, and (3) global MPPT tracking using slope calculation.

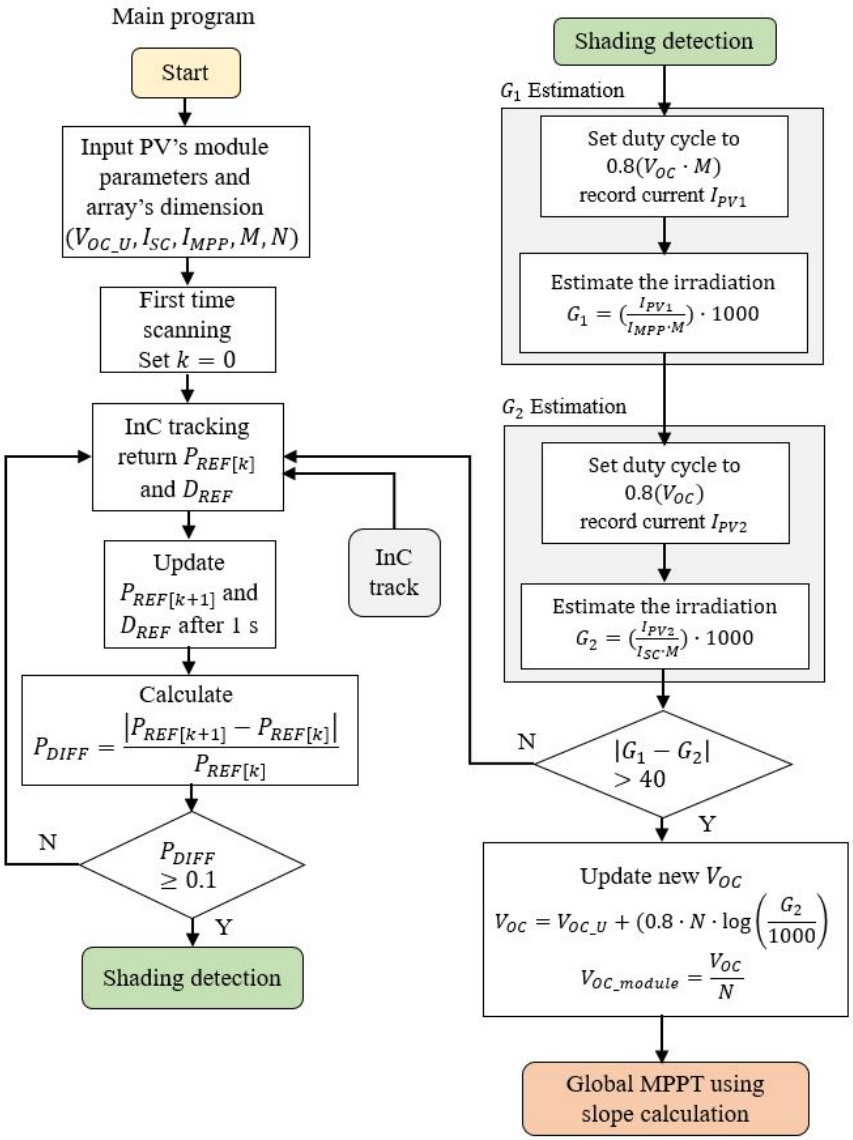

(a) Main program and Shading Detection Algorithm

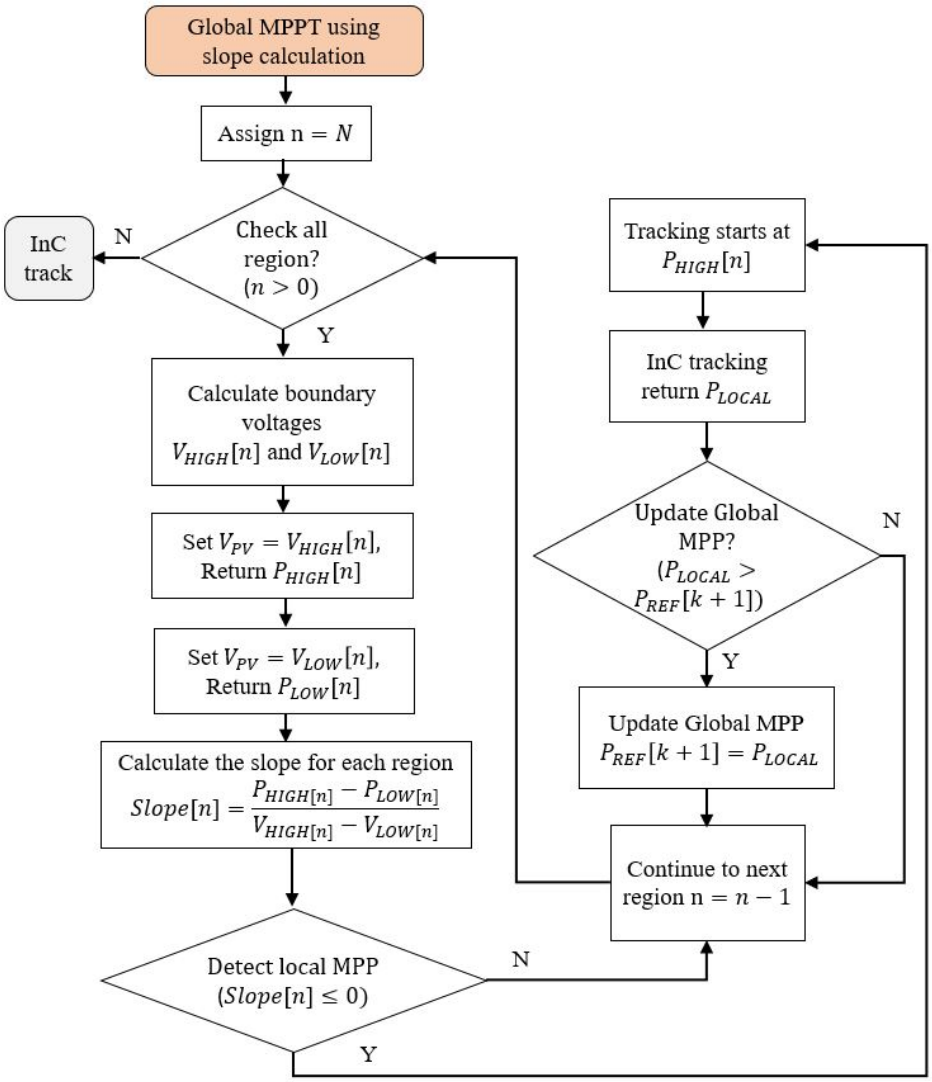

(b) Global MPPT using Slope Calculation Algorithm

Figure 2.7: Full flowchart of proposed global MPPT algorithm

2.4.2.1 Main Program

The first part of the algorithm is the main program; consists of two functions including the **parameters' initialization** and **power changes detection**.

Parameter's Intialization: In this part, the process is to input the fundamental parameters related to the PV module and the dimension of the PV system. Parameters include;

- PV module's open-circuit voltage (V_{OC})
- PV module's short-circuit current (I_{SC})
- PV module's current at the maximum power point (I_{MPP})
- Number of series-connected PV modules (N)
- Number of PV string in the array (M)

Power Changes Detection: When the program starts the first time operation, the scanning is performed to determine the initial maximum power point. After the point is found, the system maintains tracking at the point with the conventional Incremental and conductance method (InC). The tracked power is assigned as the reference point $P_{REF[k]}$ at the duty cycle D_{REF}. As shown in the flowchart, the value of the maximum power point is updated every one second and assigned as $P_{REF[k+1]}$, which is the next time sample. The reason for the update is to detect the changes in irradiation that possibly occurs from sudden shading or weather changes. The ratio of power difference, calculated as P_{DIFF}, is shown in equation 2.4.

$$P_{DIFF} = \frac{\left|P_{REF[k+1]} - P_{REF[k]}\right|}{P_{REF[k]}} \tag{2.4}$$

To identify if the value of P_{DIFF} is suitable for starting global MPPT tracking, as mentioned by Ahmed [43], the threshold needs to be chosen suitably. If the threshold is too large, the system then cannot initiate the global MPPT algorithm. But if the threshold is too small, the algorithm could perform a false trigger with unnecessary global MPPT, leading to the wastage of tracking time and power. In reference [44], if the setup threshold is set to 15% of power change, this condition does not guarantee the detection for all shading cases. Moreover, mentioned in

[45], the threshold is set up to 5%. There is no evidence of how effective this value is, but in practice, it is considered to be too small. Also, referring to [46], the studies use the standard formula's review to set up a threshold. According to the reviews, the threshold value of 0.1 (10%) is in popular use when assuming the average change of weather condition is assigned. In this case, as the weather in Tokyo, Japan does not change rapidly, the threshold of 0.1 is used.

The algorithm calculates whether or not P_{DIFF} exceeds the threshold. If the value exceeds, the program enters the next part of the algorithm, which is the **Irradiation Estimation and Shading Detection** presenting in section 2.4.2.2. On the other hand, whereas P_{DIFF} does not exceed the threshold, the program resumes to the standard InC tracking and maintain until further power change occurs.

2.4.2.2 Irradiation Estimation and Shading detection

The next part of the proposed algorithm is the shading detection and irradiation estimation. The primary purposes are to detect the shading on the PV array, also estimate the irradiation without using the sensor.

Irradiation estimation : According to other studies on solar irradiation estimation, there are several novel techniques of algorithm proposed. Research by [48] proposes the closed-form expression for solar irradiation with algebraic expression, with function of temperature, PV's current, and voltage. Although this method can estimate irradiation, the additional temperature sensor still needs to be installed, which increases the cost. This is in the same manner for reference [49], which proposed the cloud motion estimation for short-term solar irradiation prediction. The method uses the motion vector of passing cloud with the previous irradiation monitoring data recorded before the estimation.

For the proposed algorithm, concept from equation 2.1 is used to implement the irradiation estimation method. It is also confirmed the direct proportional relationship between PV's current and irradiation level. Figure 2.8 shows how irradiation estimation perform using the example I-V curves.

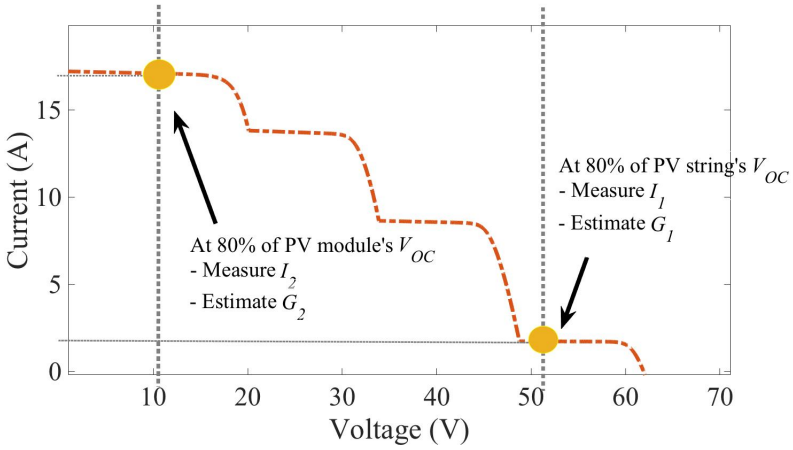

Figure 2.8: Irradiation estimation method of the example I-V curves

From figure 2.8, two irradiation levels (G_1) and (G_2) are estimated. G_1 locates at 80% of the PV module open-circuit voltage, whereas G_2 aligns at 80% of the PV's string open-circuit voltage. The algorithm measures the PV's current I_1 and I_2 using the current sensor.

Equation 2.5 and 2.6 present how the irradiation presented in the I-V curve is estimated.

$$G_1 = \frac{I_{PV1}}{I_{MPP} \cdot M} \cdot 1000 \tag{2.5}$$

$$G_2 = \frac{I_{PV2}}{I_{SC} \cdot M} \cdot 1000 \tag{2.6}$$

From the calculation, G_1 and G_2 can be simplified as the ratio between the current's at STC and shading condition. Equations also used the initialized parameters from section 2.4.2.1 (I_{SC} is the PV's module short-circuit current, I_{MPP} is the PV's module short-circuit current and M is the number of PV string).

Using the ratio between PV measured current with total string's I_{MPP} and I_{SC}, respectively, and multiplying with 1000, which is the irradiation at STC, the irradiation G_1 and G_2 can be obtained. After calculating the irradiation, the

values are used to determine whether shading happens or not. In this case, it is necessary for the system to setup the appropriate threshold.

Shading Detection : The estimated irradiations are used to detect whether significant shading occurs in the PV array or not. According to reference [43], the experiment is performed by testing samples of monocrystalline and polycrystalline PV panels and determining the threshold of difference between the irradiations. The determined threshold of 40 indicates the possibility of shading and multiple MPP exist. Equation 2.7 shows how shading condition is detected.

$$|G_1 - G_2| > 40 \tag{2.7}$$

If the difference is greater than 40, the algorithm steps to the next part which is the proposed global MPPT algorithm using the slope calculation. However, as stated in section 2.3.1 on the effects of irradiation towards the open-circuit voltage (V_{OC}); since V_{OC} is used as the indicator to track the global MPP, it is important to update the value according to the irradiation changes. Equation 2.8 shows the expression for updating V_{OC}.

$$V_{OC} = V_{OC\_U} + (0.8 \cdot N \cdot \log(\frac{G_2}{1000})) \tag{2.8}$$

Then, the PV's open-circuit voltage per one module (V_{OC_module}) can also be estimated by dividing V_{OC} with the input number of PV modules N. As shown in equation 2.9.

$$V_{OC\_module} = \frac{V_{OC}}{N} \tag{2.9}$$

The new value of V_{OC} obtained from equation 2.8 and 2.9 contributes to more precise and accurate tracking for the proposed algorithm. Additionally, the updated values are tested in short-term testing as part of the simulation result so that the efficiency can be confirmed.

To sum up the second part of the algorithm, the equation shows the methods to estimate the irradiation and detect shading condition without using either the temperature or irradiation sensors. Also, the irradiation data record is not required. This makes the method simpler to implement.

2.4.2.3 Global MPPT Using Slope Calculation

The last section of the proposed algorithm is called Global MPPT using slope calculation, which is published in the authors' published paper [54]. The concept of this algorithm is based on the inclined and declined slopes on each section of the P–V characteristic curve. The curve of the PV array is divided into sections based on the value of V_{OC_module} from the irradiation estimation and shading detection part.

For easier understanding, a step-by-step procedure of the algorithm is described using the example in section 2.4.2.4.

2.4.2.4 Example

The example is set by using 2 PV strings connected in parallel, each of which has 5 PV panels connected in series, as shown in figure 2.9. Each patterns are defined for different irradiation and temperature (25 °C and 30 °C, respectively).

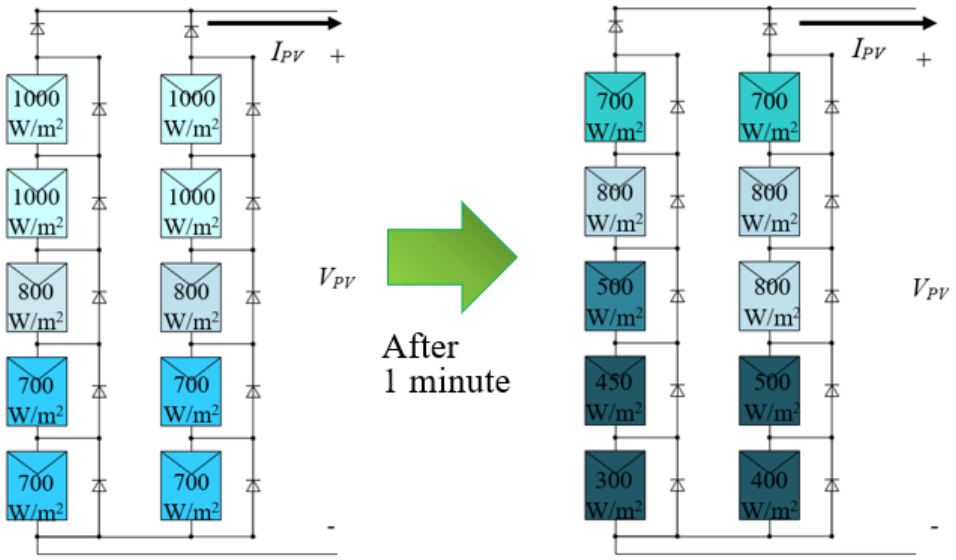

Figure 2.9: Example case for testing the Global MPPT algorithm

Table 2.2 presents the parameters for a single PV module used in this example.

Table 2.2: Parameters for a single PV module

Parameters	Value
Maximum power	425 W
Current at maximum power	5.83 A
Voltage at maximum power	72.9 V
Short-circuit current	6.18 A
Open-circuit voltage	85.6 V
Voltage Temperature coefficient	–0.36 (%/°C)
Current Temperature coefficient	0.10 (%/°C)

Main program

To explain how the program operates, firstly, the initialization is performed by inputting the PV array sizing. Including the number of strings and modules connected in series, also the PV current and voltage at STC indicated in table 2.2.

Then, first time scanning is performed for pattern C since it is the initialization of the process. The initial global MPP is tracked and remained at the point using the conventional InC method. Figure 2.10 presents P–V curve of this example. Points in the figure indicate the position where the tracking performs.

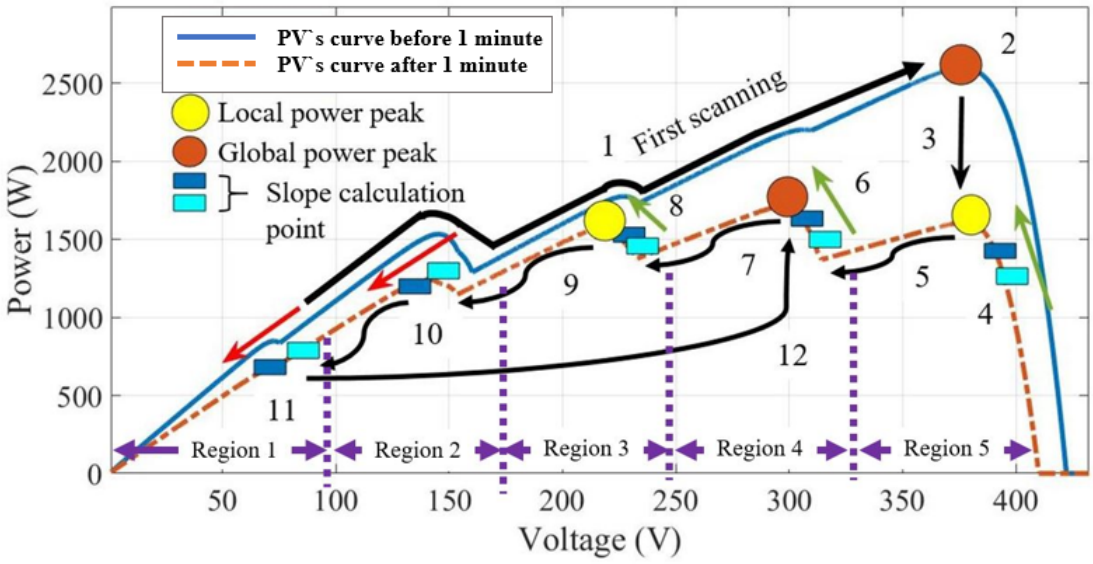

Figure 2.10: Example of P–V characteristic curves for testing the Global MPPT algorithm.

After 1 minute, the irradiation and temperature changes (rising from 25 °C to 30 °C) according to figure 2.9. At the same duty cycle, the tracking point moved from point 2 to point 3. The decrease of tracked power is recognized here, so the change of power detection algorithm operates. The system acknowledges the decrease, since the value of P_{DIFF} calculated is 0.40 ($P_{DIFF} = \frac{|1480-2472|}{2472} = 0.40$), in this case, which is greater than 0.1; then, the system can detect the change of power.

Irradiation Estimation and Shading Detection

Following is the irradiation estimation and shading detection part. The detection can be determined from the I-V characteristic curve, as shown in figure 2.11.

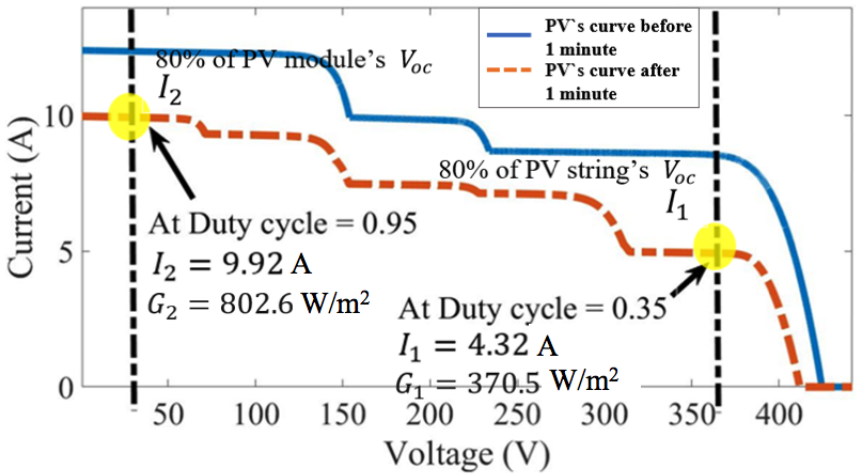

Figure 2.11: Example of I–V characteristic curves for testing the Global MPPT algorithm

This part shows the estimation of the irradiation G_1 and G_2 from the curve. Start with the measurement of current I_1 and I_2, the current I_1 is measured as 4.32 A, also I_2 presents as 9.92 A. Then using equation 2.5 and 2.6, the irradiation G_1 is equal to 370.5 W/m^2, along with G_2 as 802.6 W/m^2.

The difference between G_1 and G_2 is calculated and compared with the threshold set in equation 2.7, which equals 432.10 W. Consequently the difference is greater than 40, the system considers the I-V characteristic curve as shading detection. According to equation 2.8, the value of PV's open-circuit voltage V_{OC} is updated.

$$V_{OC} = 428 + (0.8 \cdot 5 \cdot \log \frac{802.6}{1000}) = 427.12 \text{ V}$$

$$V_{OC\_module} = \frac{427.12}{5} = 85.42 \text{ V}$$

From the calculation result, V_{OC} reduces due to the increase of the temperature. The updated value of V_{OC} uses in the global MPPT's part.

Global MPPT using Slope Calculation

After the system acknowledged that the shading occurs with more than one power peak located in the P-V characteristic curve, global MPPT uses a slope calculation, which is the final part of the algorithm performs.

According to figure 2.10, the system starts to track from point 4, which is the rightmost region of the P-V curve and has the highest percentage of global power peak to be located. Since the number of PV panels connected in series is 5 ($N = 5$), the system calculates the reference point for calculating the slope, shown as dark blue and light blue points in figure 2.10. The slope calculation points are assigned based on the test mentioned in the introduction. According to this information, the slope calculation chooses from the multiples of each open-circuit voltage in the region deducted by the scaling ratio. Equations 2.10 and 2.11 show the calculation for each slope calculation point on the P–V curve.

$$V_{HIGH}[n] = \begin{cases} (V_{OC\_module} \cdot n) - [(1 - 0.46) \cdot V_{OC\_module}] & , n > N - 2 \\ (V_{OC\_module} \cdot n) - [(1 - 0.51) \cdot V_{OC\_module}] & , otherwise \end{cases} \tag{2.10}$$

$$V_{LOW}[n] = \begin{cases} (V_{OC\_module} \cdot n) - [(1 - 0.51) \cdot V_{OC\_module}] & , n > N - 2 \\ (V_{OC\_module} \cdot n) - [(1 - 0.56) \cdot V_{OC\_module}] & , otherwise \end{cases} \tag{2.11}$$

where N is the number of the PV module connected in series, and n is the variable assigned in the flowchart in figure 2.7. Using equations 2.10 and 2.11, all slope calculation points can be calculated. For example, the rightmost blue point is assigned as $V_{HIGH}[5]$, which is calculated from equation 2.10 as:

$$\begin{aligned} V_{HIGH}[5] &= (V_{OC\_module} \cdot 5) - [(1 - 0.46) \cdot V_{OC\_module}] \\ &= (85.42 \cdot 5) - [(1 - 0.46) \cdot 85.42] \\ &= 381.54 \text{ V} \end{aligned}$$

The PV's voltage is controlled by the duty cycle to move to the point; after that, the reference power ($P_{HIGH}[5]$) is measured as 8.21 W. Following the next reference point $V_{LOW}[5]$ determined from equation 2.11 :

$$\begin{aligned} V_{LOW}[5] &= (V_{OC\_module} \cdot 5) - [(1 - 0.51) \cdot V_{OC\_module}] \\ &= (85.42 \cdot 5) - [(1 - 0.51) \cdot 85.42] \\ &= 385.60 \text{ V} \end{aligned}$$

From the calculation, the negative value of the slope is shown ($381.54 - 385.60 = -4.06$), so the graph has a trend of decline, and the power peak can exist. Because of this, the system starts the conventional tracking at the region using InC and finds point 5 as the local power peak. The value is assigned as P_{LOCAL} and saved for comparison with tracked powers in other regions. The steps are repeated in other regions of the P-V characteristic curves from regions 4 to 1. For this part, $V_{HIGH}[n]$ and $V_{LOW}[n]$ are tracked in each region.

Table 2.3 presents the summarized result of the slope calculation in each region of the P-V curve. The system finds the power peak in regions 4 and 2 but finds the decline slope in regions 3 and 1 according to figure 2.10.

Table 2.3: Summarized result for global MPPT using slope calculation for the example

Region (N)	**Reference data**				*Slope* **(W/V)**	**Decision**	**Power tracked** (W)
	P_{HIGH} (W)	V_{HIGH} (V)	P_{LOW} (W)	V_{LOW} (V)			
1	527.69	43.56	568.20	47.83	9.48	Not detected	-
2	1220.00	128.98	1230.00	138.00	1.11	Not detected	-
3	1570.00	215.12	1560.00	219.18	–1.96	Detected	1570.00
4	1700.00	296.30	1680.00	300.36	–5.37	Detected	1710.00
5	8.21	381.54	3.45	385.60	–1.17	Detected	1640.20

From the results shown in table 2.3, the proposed algorithm locates the global power peak in region 4 (1710.00 W). The result confirmed by figure 2.10 shows where the maximum power point is located. Overall, this example demonstrates the operations of the proposed algorithm step by step and verifies the result of global MPPT.

2.5 System Implementation and Results

2.5.1 Simulation Results

2.5.1.1 Basic Case Study

Basic case study is shown in figure 2.12(a), assuming the passing cloud which dynamically changes the irradiation across the small-scale PV system with the rated power of 1 kW. The test is simulated using MATLAB/Simulink based on the P-V curve of passing cloud shown in figure 2.12(b).

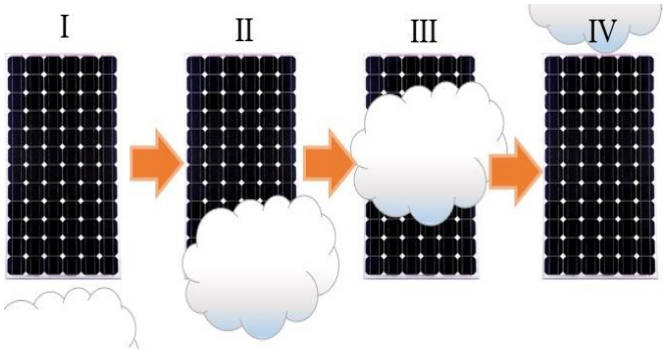

(a) Basic case study testing condition

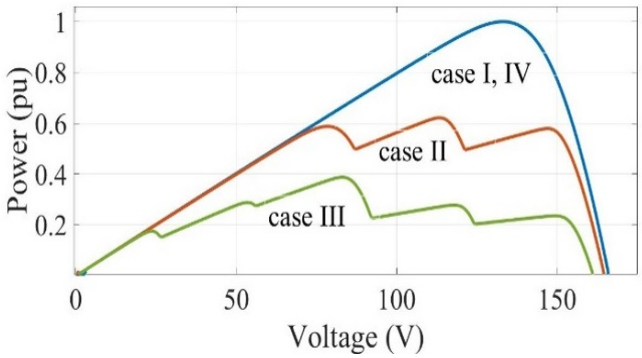

(b) P-V characteristic curves under irradiation changes by a passed cloud

Figure 2.12: Basic case study testing condition and P–V characteristic curves

The PV's array circuit implements with the DC-DC boost converter circuit shown in the system's description in figure 2.6. The converter is connected to the 5 PV panels connected in series, with a 220 V DC bus. Tested PV panel's specification under standard test condition also shown in table 2.4.

Table 2.4: Parameters for a single PV module for basic case study

Parameters	Value
Maximum power	205.80 W
Current at maximum power	7.71 A
Voltage at maximum power	26.60 V
Short-circuit current	8.36 A
Open-circuit voltage	33.20 V
Voltage temperature coefficient	-0.36 (%/°C)
Current temperature coefficient	0.10 (%/°C)

Figures 2.13(a) and 2.13(b) show the complete results of the proposed method, including the tracked power and located voltage. The tracking is divided into three regions, whereas figures 2.13(c) to 2.13(h) magnify the graphical results in each region for better understanding.

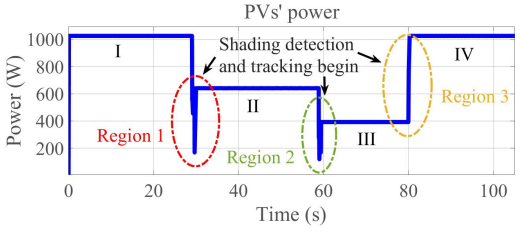

(a) PVs' power tracking result

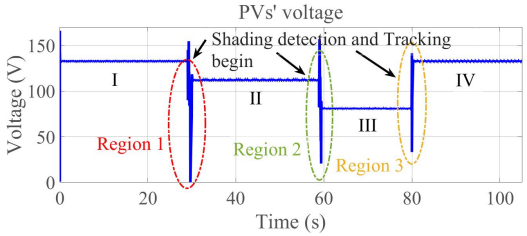

(b) PVs' voltage tracking result

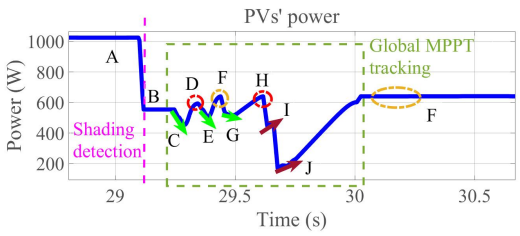

(c) PVs' power region I

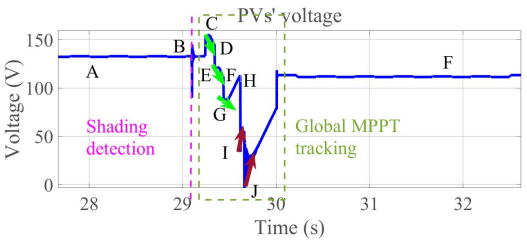

(d) PVs' voltage region I

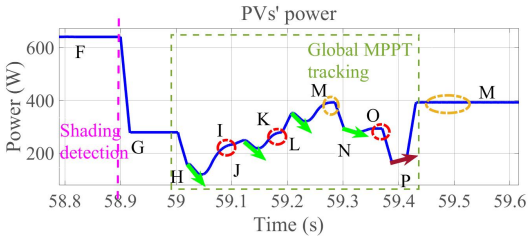

(e) PVs' power in region II

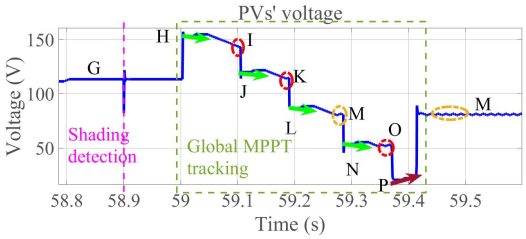

(f) PVs' voltage in region II

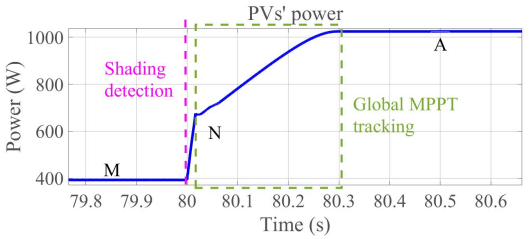

(g) PVs' power in region III

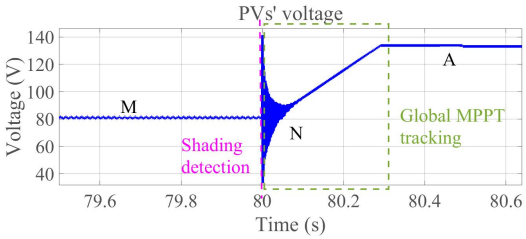

(h) PVs' voltage in region III

Figure 2.13: Results from proposed algorithm of the basic case study

Region I

Figure 2.13(c) shows the magnified global MPP tracking in the transition from the case I to II. Result shows the PVs' power drops from 1023.5 W (point A) to 554.4 W (point B). The algorithm tracks the power changes and proceeds to the irradiation estimation and shading detection part, highlighted in the figure. After the program acknowledges that shading occurs, the global MPPT starts tracking from point B onwards.

Begin tracking from the first slope calculation point of the P-V curve (point C), the tracked slope shows the negative result (represented by the green arrow); the system records the peak value at point D. Afterwards, the algorithm continues the same calculation in other regions by shifting to the next searching region as explained in equation 2.10 and 2.11, as the voltage's transition, shows in figure 2.13(d). All tracked powers are marked at points D, F, and H. After locating all the local peaks, the algorithm returns the maximum value which is point F at approximately 630 W (as shown in 2.13(c)). The tracking time takes approximately 0.77 seconds (0.90 seconds if the detection time is included).

Region II

For the next transition when the cloud covers the panel, similar procedure repeats. Starts from the voltage pair at point H, the voltage shows the inclining trend (presented by the green arrow). The algorithm acknowledges the existence of the peak. Then, the system tracks the peak (at point I). The step repeats by shifting to the next searching region, at points J, L, N and P. The local peaks include points I, K, M and O as indicated in figure 2.13(e) and 2.13(f) . At point P, indicated as the red arrow shows the declining trend of the slope. The algorithm acknowledges the non-existence of the local peak in the region and moves to the next region. After locating all the local peaks, the program returns the maximum power at approximately 400 W. The tracking and detection time consumes approximately 0.51 seconds.

Region III

After the cloud passes the panel, the system starts to operate at its standard test condition. From the tracked power at point M, the tracking power resumes the maximum power at point A onto 1023.5 W. Since the system resumes the unshaded condition, there's only one power peak that exists in the P-V curve, making it's faster for the algorithm to locate the maximum power. The graphical results is explained in figure 2.13(g) and 2.13(h). In total, the system uses approximately 0.27 seconds for tracking in this region.

To sum up, this basic case study confirms the accuracy and efficiency of the proposed algorithm. The program can locate the global MPP at all transitions of the irradiations. To conclude the dynamic testing, the result presents the accurate tracking with an excellent transient response, with a fast-rising and settling time of approximately 0.51 seconds on average. Furthermore, the results also develop the stability after achieving the accurate MPP.

2.5.1.2 Dynamic Case Study

In this section, the test involves more dynamic changes of irradiation to demonstrate the change in real weather conditions. Study divides to **short-term**

and **long-term test**. Figure 2.14 shows the circuit diagram of how the proposed global MPPT is tested.

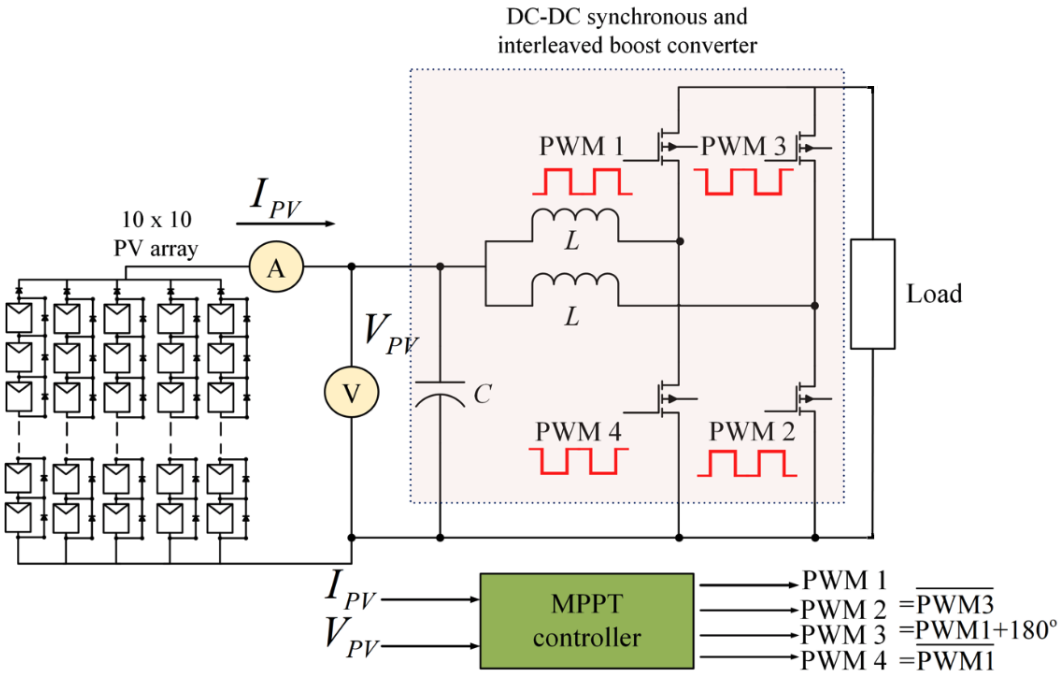

Figure 2.14: System diagram for the dynamic case study

The circuit consists of the medium-scale PV system with the rated power of 40 kW. Components include the PV arrays (ten strings with ten panels connected in series), where each panel has the specification as described in table 2.2, with voltage and current sensors and a DC-DC converter circuit, which is the synchronous and interleaved boost converter.

Short-term Test : For a short-term test, the proposed algorithm uses ten different P-V characteristic curves case studies to represent irradiation changes. Figure 2.15(a) shows P-V characteristic curves from patterns 1 to 10, which are applied to the simulation circuit. Each pattern is set to change to the next pattern at ten-second intervals. Figure 2.15(b) presents the graphical results of power tracking using the proposed algorithm compared to conventional scanning.

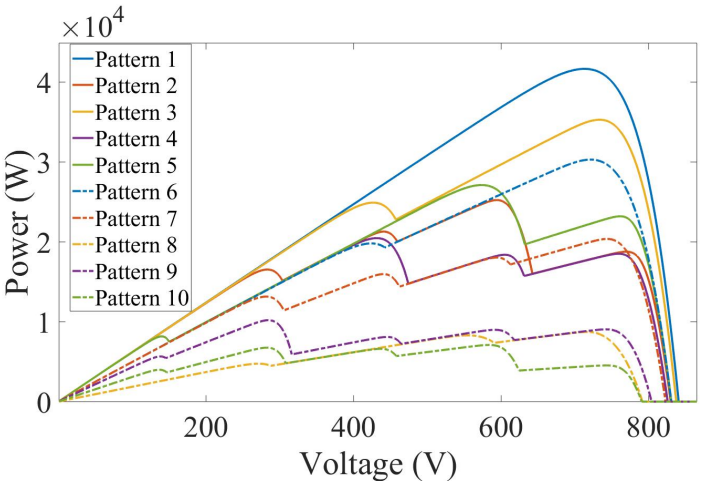

(a) P-V characteristic curves for short-term testing

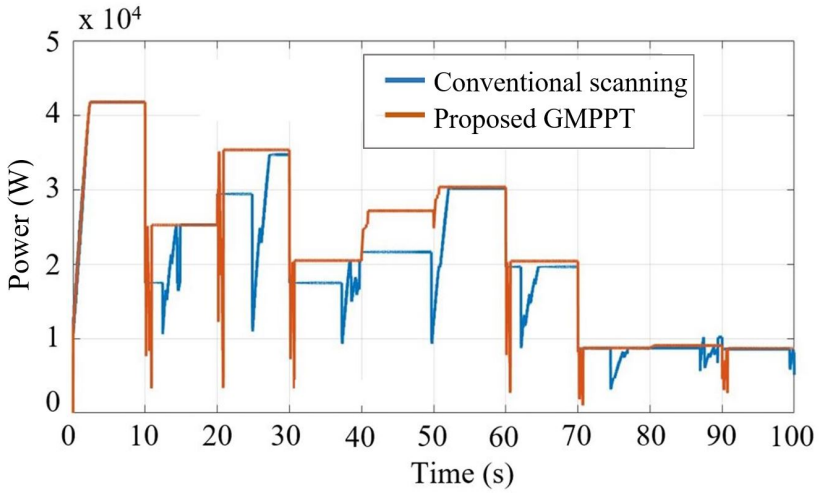

(b) Result of the tracked power over operating time

Figure 2.15: Short-term testing simulation results

The proposed algorithm is compared with the conventional scanning method which exists in commercial inverters. Table 2.5 summarizes the effectiveness comparison of conventional scanning and the proposed global MPPT.

Table 2.5: Performance comparison of conventional scanning and proposed global MPPT (GMPPT) algorithm using short-term testing

Shading pattern	**Tracking method**	**Tracked power**(W)	**Tracking time**(s)	**Maximum power from P-V curve** (W)	**Efficiency** (%)
1	Conventional scanning	41.67	2.35	41.75	99.81
	Proposed GMPPT	41.72	2.33		99.93
2	Conventional scanning	25.24	2.49	25.26	99.92
	Proposed GMPPT	25.25	0.91		99.96
3	Conventional scanning	34.71	2.57	35.36	98.16
	Proposed GMPPT	35.33	0.87		99.92
4	Conventional scanning	17.42	2.06	20.48	85.06
	Proposed GMPPT	20.47	0.71		99.95
5	Conventional scanning	21.61	2.79	27.14	79.62
	Proposed GMPPT	27.12	0.91		99.93
6	Conventional scanning	30.10	2.41	30.37	99.11
	Proposed GMPPT	30.34	0.77		99.90
7	Conventional scanning	19.63	3.39	20.39	96.27
	Proposed GMPPT	20.38	0.56		99.95
8	Conventional scanning	8.87	2.65	8.90	99.66
	Proposed GMPPT	8.73	0.74		98.09
9	Conventional scanning	10.17	2.10	10.19	99.80
	Proposed GMPPT	9.05	0.71		88.81
10	Conventional scanning	8.59	2.60	8.71	98.62
	Proposed GMPPT	8.69	0.78		99.77

The focus parameters in the results include tracking time and the efficiency to locate the Global MPP. It notices that the tracking time used for the proposed global MPPT method is less than the conventional scanning method. The algorithm reduces tracking time and consumes less power during the tracking operation. The loss of power gradually reduces each time tracking is performed.

Long-term Test : To perform the testing as demonstrated in the daytime operation similar to what the PV system operates in one day, the long-term test simulates different weather conditions in 10 hours (36 000 seconds). The test divides into a *steady* and *rapid change of weather conditions*. Moreover, the information is collected from the real measured data at Shibaura Institute of Technology, Tokyo, Japan in June 2018. Figure 2.16(a) and 2.16(b) shows the graphical results of tracking power using the scanning and proposed algorithm. The scanning is set to be a default every 15 minutes.

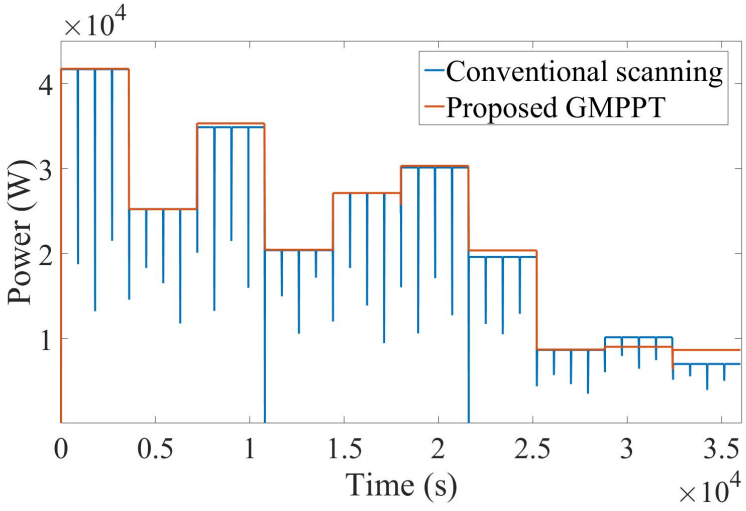

(a) Results of tracked power for long-term testing at steady change weather conditions

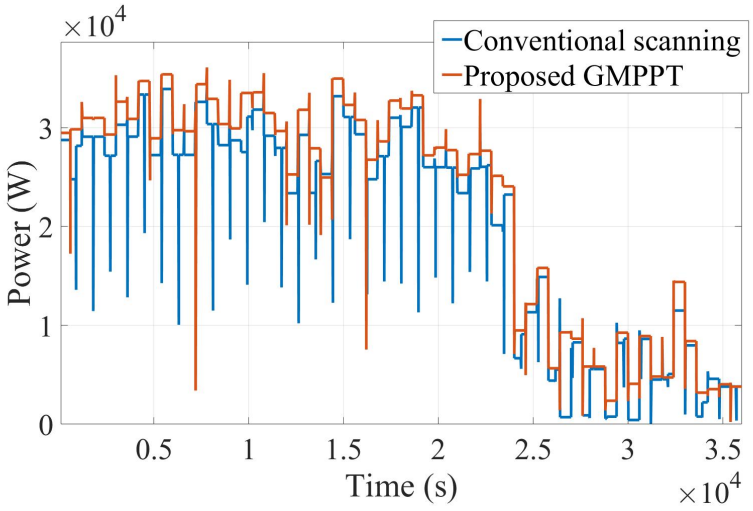

(b) Results of tracked power for long-term testing at rapid change weather conditions

Figure 2.16: Results of tracked power for long-term testing at different weather conditions

Table 2.6 presents the numerical results for long-term testing. The results show the total power achieved per day, per annum, and estimated revenue achieved using an energy selling rate in Tokyo, Japan in 2018 (20 JPY per kWh).

Table 2.6: Performance comparison and revenue of scanning and proposed global MPPT (GMPPT) algorithm using long-term testing

Weather condition	**Tracking method**	**Energy extracted per day** (kWh)	**Annual energy** (kWh)	**Revenue in JPY**	**Additional income in JPY**
Steady change	Conventional scanning	224.83	82 062	1 641 259	-
	Proposed GMPPT	227.18	82 921	1 658 418	17 159
Rapid change	Conventional scanning	206.51	75 376	1 507 520	-
	Proposed GMPPT	224.16	81 818	1 636 360	128 840

It is interesting to observe the rapid change condition, the proposed method can enhance the total energy of 8.55% compared to the conventional algorithm. Result confirms the advantage of the proposed algorithm, not only the performance to operate in both steady and rapid change weather conditions; the tracking speed enhancement also reduces power loss. To summarize, the speed enhancement is shown in the short-term testing, where each track has less power loss than conventional scanning. Consequently, the enhancement increases the energy generated from the PV system when operated in the long-term. Furthermore, the system also show the robust responses according to simulation results. Both small-scale and medium-scale systems show the stability after reaching the tracked MPP. The small power fluctuation may cause during the tracking operation; however, the system can recover back to the stability MPP within 5 seconds. Especially in the short-term test, eventhough the rapid change of irradiation occurs, the system is capable to response fast for tracking the accurate power.

2.5.2 Experimental Results

For confirming the efficiency of the proposed algorithm, the practical experimental is performed. Mainly, the experiment consists of the synchronous and interleaved DC-DC boost converter, Texas instrument F28335 digital signal processor (DSP), the PV simulator circuit and the electrical load. Figure 2.17 shows the photo of the experiment setup.

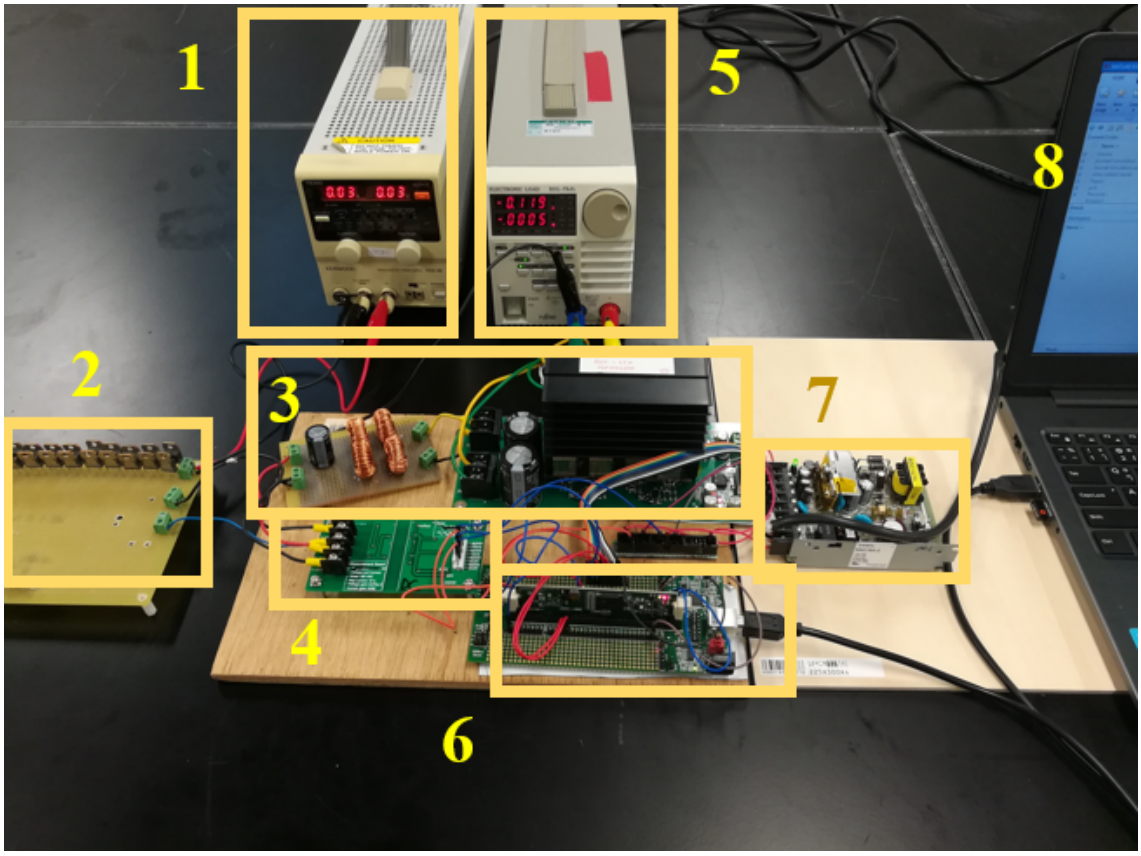

Figure 2.17: Photograph of the experimental system

From photo 2.17, the list of the components includes

1. DC power supply
2. PV simulator circuit
3. DC-DC synchronous and interleaved boost converter
4. Voltage and current sensor
5. Electronic load
6. DSP F28335 control card
7. 12V DC power supply

8. Laptop for data acquisition

Figure 2.18 presents the system's diagram.

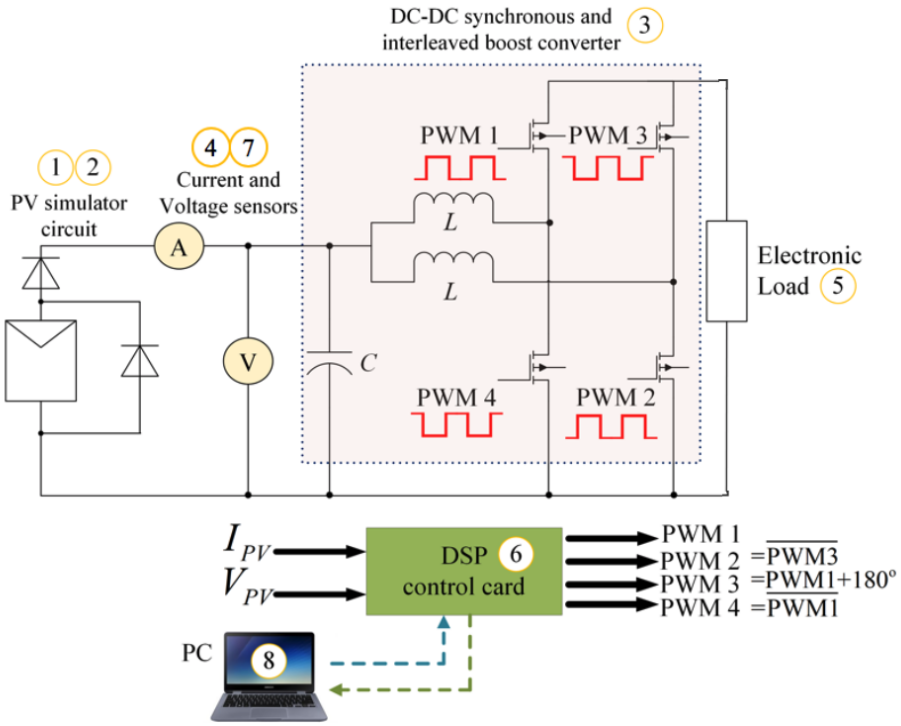

Figure 2.18: Diagram of the experimental system of the proposed global MPPT algorithm

From figure 2.18, the global MPPT algorithm is programmed using a Texas instrument F28335 DSP control card. The input voltage and current are inputted via the sensor unit to scale down the parameters before inputting to the control card. The switching control of this converter is performed by setting up the phase shift, according to figure 2.18. The inverted switching waveform consists of PWM4 (inverted from PWM1) and PWM2 (inverted from PWM3); the phase shift is set to be fixed at 180° for PWM3 (shifted from PWM1 which is the primary signal).

The setup parameters for the experiment include the sampling frequency as 10 kHz for the scanning and proposed method, and the incremental step is 0.2

seconds, which is the minimum step in which the tested DC-DC converter can operate efficiently. The experimental results are achieved from the voltage and current sensors connected to the converter's circuit, then evaluated in the control card and imported to the PC.

Figure 2.19(a) and 2.19(b) shows the graphical results of the tracking algorithm.

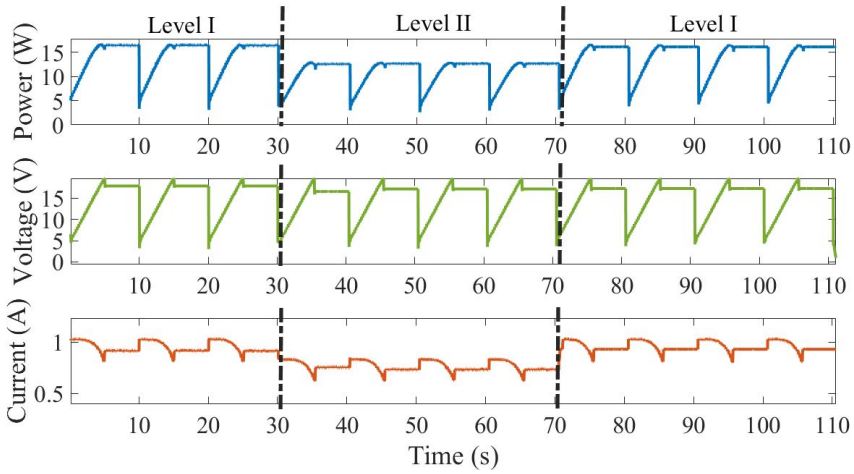

(a) Result of conventional scanning

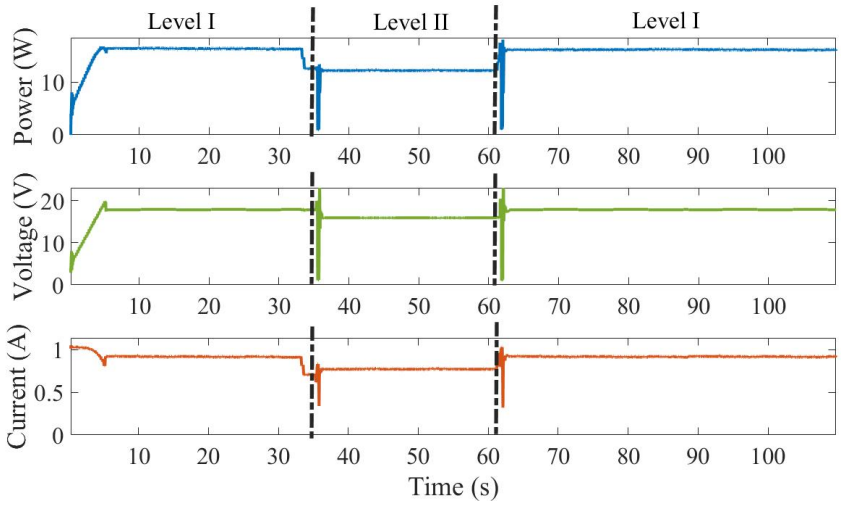

(b) Result of proposed global MPPT algorithm

Figure 2.19: Experimental results of the proposed global MPPT algorithm

The test consists of two different short-circuit current values set using the DC power supply to represent the different irradiation. The current is set as 1.03 A for level I of irradiation and 0.89 A for level II. The programs have a task to track the power changed from level I to II before restoring to level I again. From the result shown in figure 2.19(a), the conventional scanning takes approximately 4.96 seconds to track the power from level I to level II, which gives the value of 16.3 W and 12.6 W, respectively. As for the proposed method in figure 2.19(b), it takes approximately 0.42 seconds. The result confirms the simulation outcome that scanning consumes more time to scan throughout all values of power, causing less power loss during each tracking time. The experiment verifies the performance of the proposed algorithm in which the program can locate the correct MPP each time the irradiation changes. The results also show the robustness after the tracking completes.

2.5.3 Grid-connected PV system test

In this section, the proposed algorithm is tested with the grid-connected PV array for determining the robustness of the system. Figure 2.20 shows the diagram of the proposed algorithm implemented in the grid-connected PV system.

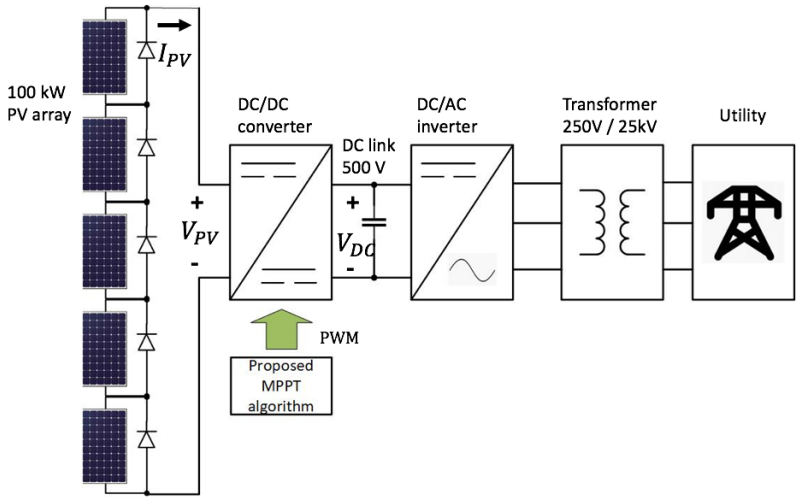

Figure 2.20: Diagram of the grid-connected system of the proposed global MPPT algorithm

The system is implemented based on the average model of a 100-kW Grid-Connected PV Array, presented by Mathworks [55]. Whole system consists of 100 kW PV array (with 5 series and 64 parallel PV module configuration) connects to the DC-DC converter with the installed proposed algorithm. The inverter is connected via the 500 V DC link before connecting to the utility. The simulation is performed using the referenced system. By applying the decrease irradiation at 2 seconds of the simulation time, the tracking results are shown. Figure 2.21 presents the simulation results including the tracked power, current, voltage and the DC link voltage.

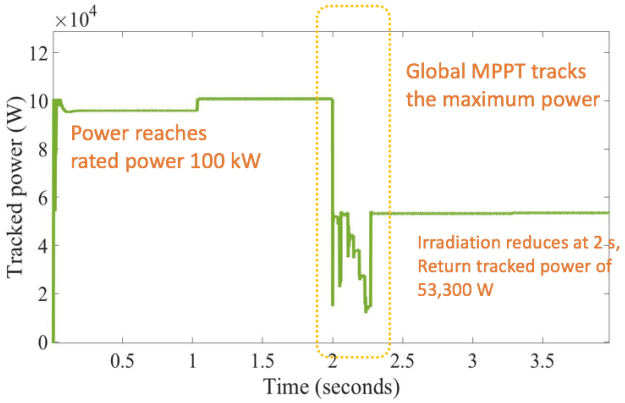

(a) Grid-connected PV system tracked power

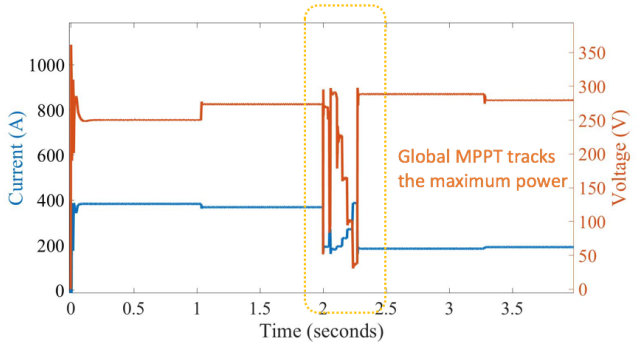

(b) Grid-connected PV system tracked current and voltage

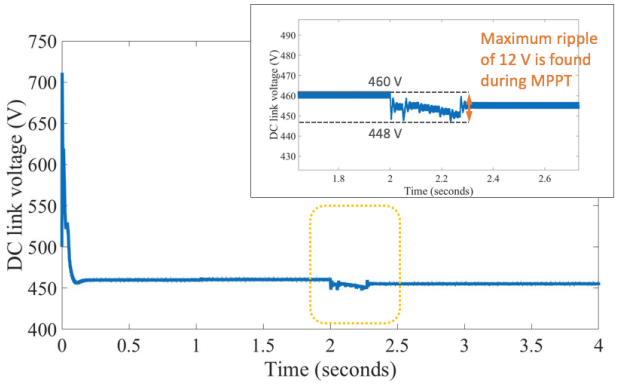

(c) DC link voltage

Figure 2.21: Simulation results of the grid-connected PV system with the proposed global MPPT algorithm

From figures 2.21(a) and 2.21(b) , the result shows the successful Global MPP tracking of the grid-connected PV system. Firstly at the irradiation of 1000 W/m^2, the tracked power reaches the maximum power of 100 kW. The system maintains the highest power. Continuously, after the irradiation reduces at 2 seconds, the proposed algorithm starts tracking the power by the slope calculation. Tracked power of 53,300 W is achieved within approximately 0.3 seconds of tracking time. Also, during the tracking process, the DC link voltage in figure 2.21(c) shows a maximum ripple of 12 V in short-period, after tracking completes the control system of the inverter controls the DC link voltage to become stable.

2.6 Conclusions

This chapter proposes the new global MPPT algorithm, including the irradiation estimation and tracking method using the slope calculation technique. The implementation confirms that the proposed tracking algorithm can operate with high efficiency and accuracy. Both graphical and numerical results prove the effectiveness of tracking time within 3.40 seconds and the accuracy of 98.62%. Moreover, the system was also simulated in the long-term with real weather data. Result also shows 8.55% total energy enhancement when compared with

the conventional method. To sum up, the increase in tracking speed shows in the short-term test that each track has a lower power loss than in conventional scanning. Consequently, when operating in the long-term, it increases the energy generated from the PV system. The proposed method can also increase the revenue benefits in the operating day. The factor affects the robustness of the algorithm mainly includes the precision of the current and voltage sensors, suitable sampling time and stablility of the DC link voltage if connected to the inverter. The high robustness can achieve by the well-implemented control system of the converter and grid-connected inverter.

Chapter 3

Simplified Hotspot Model and Proposed Hotspot Detection Algorithms for Photovoltaic Systems

According to chapter 2, it is confirmed by the analysis and evaluation that shading condition causes a significant decrease in the power generation level. Consequently, to expand the usage of the PV system, improving reliability is essential. For the PV system, similarly to other power systems, failures can occur during the period of operation. One of the failure problems that occurs towards the operation of PV system is the **hotspot**, which causes the power dissipation and the physical damage.

A hotspot is defined as the fault formed on the panel's surface due to the high temperature, which happens from the consequence of shading on the PV panel's surface when a PV cell in a panel generates less current. The fault occurs when the cell is entirely or partially shaded, cracked, or electrically mismatched. Hotspot not only causes the generated power reduction, but the severity of the stored heat could also lead to a dangerous fire hazard.

Unlike a typical electric circuit, since hotspot is the blind defection and difficult to access the internal circuits from the PV module, making the detection difficult; therefore, special equipment is necessary. Conventionally, the detection uses the infrared camera to capture a thermal image of objects under inspections. Figure 3.1 shows the example of hotspot appearance on the PV module captured by the infrared camera [56].

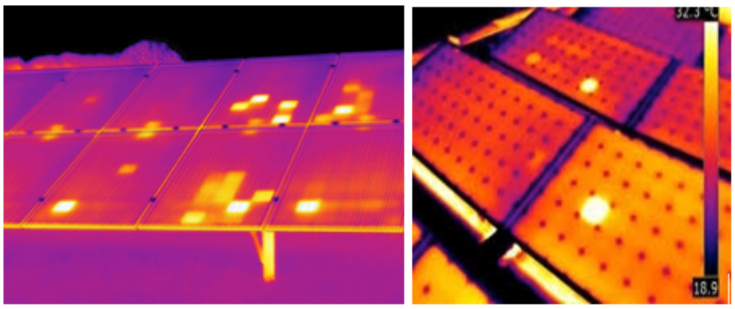

Figure 3.1: Example of hotspot on PV module captured by the infrared camera [56]

From figure 3.1, the camera captures the hotspot as the brighten areas formed on the PV module. Although the thermography detection method's performance is effective, the cost of the equipment—especially the infrared camera—is generally quite high, and a workforce for the routine checkup is also needed. Moreover, human error could occur involuntarily. Although hotspot happens on a part of the area on the PV cell, the power dissipation caused by the temperature can be found. The defected rate can also increase; this has been described in researches by Pillai et al [7] and Main et al [57] in which both describe the hotspot increases its degradation level over the operating time. In addition, it is confirmed by case studies and surveys that hotspot causes the reduction of the performance ratio, making the generated power of the PV system decreases. Therefore, it is important for researchers to develop methods for detecting hotspots accurately and effectively.

The main context of this chapter is to propose the hotspot detection method for the small-scale PV system, in the form of the algorithm. The method is designed based on the simplified PV module structure. Accordingly, the algorithm

is designed based on the observation of hotspot characteristic towards the PV system, using the characteristic curves. The algorithm identifies the hotspot by calculating the rate of change of PV's current on the characteristic curve after locating the searched region, based on the installed array's dimension. After detection, the algorithm presents the module's status using the indicator signal.

The usefulness of this research is the proposed algorithm, which can detect the hotspot within a short period, contributing the advantage for the PV maintenance. The mathematical equations accompanied by the flowchart describe the algorithm with the case studies for better understanding. The results of the hotspot detection algorithm are presented in the form of graphics with the indicator signal. This signal shows the presence of the hotspot when the algorithm detects the fault. Specifically, the contribution of this research is the algorithm, which can detect the hotspot with fast response and contribute the advantage for PV maintenance. The detection can perform when PV system is under operation. Also, the algorithm does not require the infrared camera and the irradiation sensor; making the low-cost implementation.

Structure of this chapter is arranged as follows. Section 3.1 states the problem of the hotspot, including the cause of occurrence and consequence of the PV system. The reviews of previous researches in hotspot modeling and detection methods are presented in section 3.2. In section 3.3, the analysis of the hotspot (consists of hotspot modeling and performance analysis) is described, and section 3.4 shows the proposed hotspot detection algorithm. The system's implementation and results are discussed in section 3.5 to validate the algorithm under various PV sizing and conditions.

3.1 Problems Statement

The main cause of the hotspot is formed by the localized heat on the surface of the PV module [59, 60]. The hotspot cell absorbs the current generated from the PV cell. Instead of supplying the power, the hotspot forces the cell to absorb the power and increases the PV cell temperature. Afterward, the PV's output

current from cells is reduced from the circulation of the current within the cell, making the PV's hotspot cell voltage become reversed bias. In consequence of the reduction of current, the generated power of the panel reduces accordingly. The efficiency degradation of the module has been confirmed by many of the research works [61, 62, 63]. If the temperature reaches and exceeds the limited threshold, the hotspot can be formed and bring permanent damage to the module.

Additionally, the survey data set from the installed PV system around the world proves how effective the hotspot to the PV's performance. The highlighted study is presented in [8] about the assessment of the hotspot in the PV sites over the UK in 2017, in which the majority have been installed for 10 years. Figure 3.2 presents the geographical map for the PV sites located across the UK and the hotspot probability of occurrence among all tested PV modules. The collected data shows that after 10 years of installation, 42% of total examined PV modules contain the hotspot in which varies from cell to string scale. Furthermore, it is reported from the study that over the operation of 10 years the mean performance ratio of the PV systems is dramatically reduced due to the existence of hotspot in the modules. Significantly, the highest percentage of difference compared to normal condition PV module is calculated at -15.47%.

Another confirmation is confirmed by Pillai et al [7], which describes the damage from the hotspot towards the solar farm in the US, and shows that hotspots can cause a reduction of energy yields up to 6%. It was also reported by Bharadwaj et al [59] that 25% of the short term failure distribution of PV module installed in the US is due to the hotspot. Moreover, in Japan, hotspot causes major defection in the PV module and reduction of power. Approximately 15% of reported failures were due to the panel's malfunction [64].

Additionally, research by Mani et al [57] describes the degradation of the panel will increase over the operating time. The hotspot will continue to heat up and thus result in more physical damage to the modules. The work also states the degradation rate of the hotspot PV module appears to degrade at a higher rate than the normal condition modules, which could lead to module mismatch issues in a module-string. The rate for 12-year modules exists between 0.6-2.5% per year.

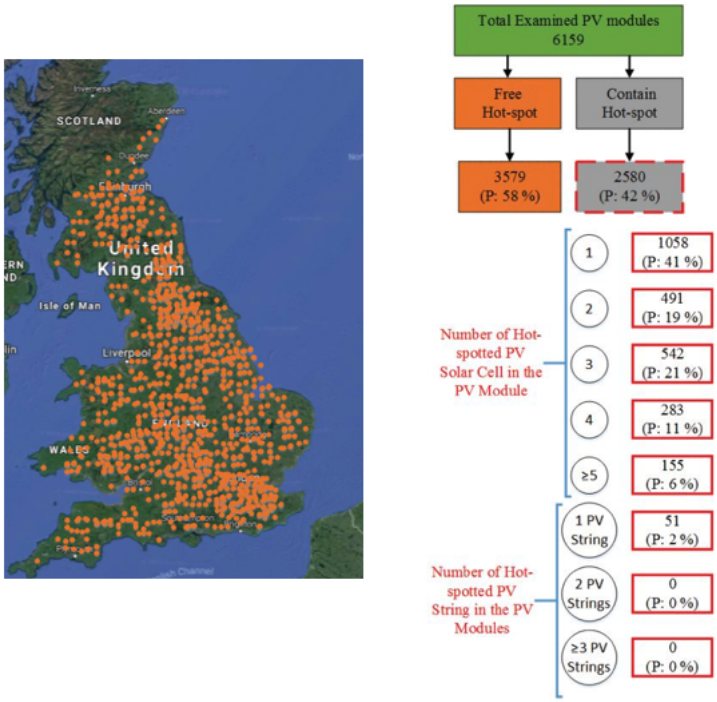

Figure 3.2: Geographical map for the PV sites location across UK and hotspot probability of occurrence [8]

According to IEC 61215 (design qualification and type approval of PV module), the standard states the hotspot endurance testing method to determine the ability of the module to withstand hotspot heating effects. Figure 3.3 shows the example of the hotspot effect in PV cell by measuring the I-V curves.

The amount of power dissipated in cell Y is shown in a shaded area, approximately equal to the product of the module current and the reverse voltage developed across Y. For any irradiation level, maximum power is dissipated, which the reverse voltage across Y is equal to the voltage generated by the remaining (s–1) cells in the module. The standard states the step-by-step testing procedure in which manufactured PV module needs to pass. By exposing the module in different shading ratios and enduring the test for 5 hours, the monitoring is performed by an I-V curve tracer. If the tested module contains no evidence of major visual defects, the degradation of maximum output power does not exceed 5% and no change in insulation resistance, the module passes the test and qualified.

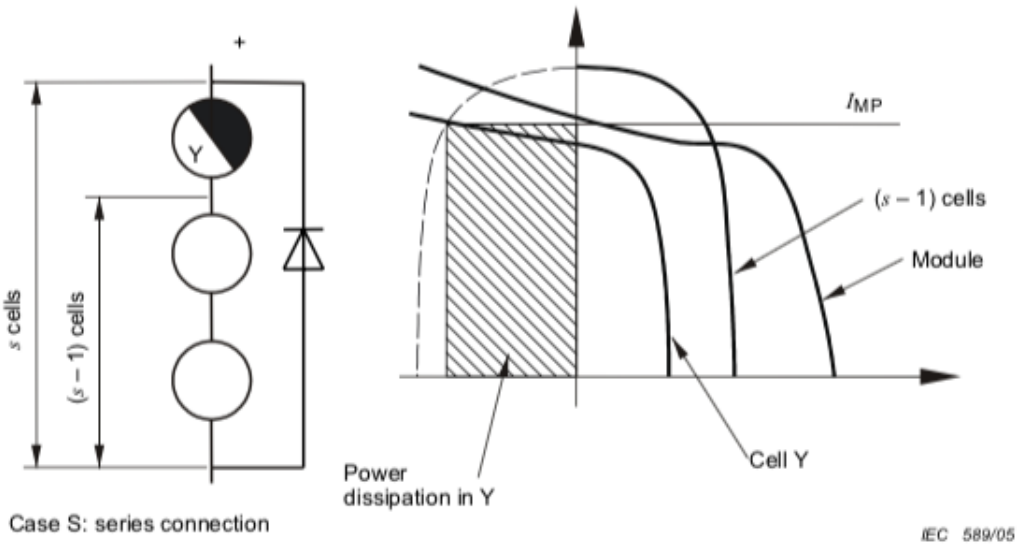

Figure 3.3: Hotspot effect in PV cell by IEC 61215 [5]

3.2 Literature Reviews

This section presents the reviews of previously published works on hotspot modeling and detection methods, which has different implementation and varies by complexity respectively.

As mentioned in section 3.1, the IEC 61215 standard explains the hotspot characteristic using the I-V curve and evaluate the power dissipation inside the cell. The dissipation level can be estimated using the area under the I-V curve where the voltage is negative (highlighted in figure 3.3). The missing description of the maintenance and detection procedures, again, are not described. Moreover, research by Qian et al [74] states that IEC 61215 mentions only the hotspot monitoring of the shaded cell; however, the hotspot occurring in unshaded condition is not specified.

As mentioned in section 3.1, the hotspot can be found by using infrared thermography. The infrared sensors are used to obtain thermal images or thermograms of objects under inspection [58]. The image captured by the camera shows

the presence of the hotspot as a white spot on the PV panel's surface. Although the thermography detection method's performance is effective, the cost of the equipment—especially the infrared camera—is generally quite high, and a workforce for the routine checkup is also needed. In this case, researchers are trying to develop the topology to detect the hotspot in PV module regardless of the camera for reducing the cost. The following are the reviews of the major proposed hotspot model.

The first model shows the AC parameter characterization to represent the effects of the hotspot [66]. Figure 3.4 presents the advanced dynamic PV circuit model. Apart from the single-diode parameters (current source I_{ph}, forward-bias conduction diode D_f, shunt resistance R_{sh}, and series resistance R_s), this model also incorporates AC parameters with a series inductance L_s, variable parallel capacitance C_p, and reverse-bias conducting diode D_r with a breakdown voltage offset V_{bd}.

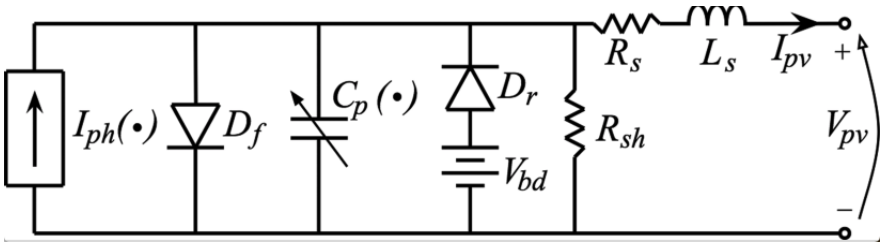

Figure 3.4: PV circuit model with reversed breakdown voltage [66]

From the model, R_s and L_s are associated with the physical length, area, and shape of the leads. Larger R_s leads to higher conduction losses, particularly for cells with higher rated current levels. The value of R_{sh} depends on the PV material, thickness, and manufacturing quality. The complexity of this model is that the circuit's parameters are not treated constantly due to the effects of PV's operating point and temperature. Also, it requires many mathematical equations to fit all the parameters, especially for AC parameters that require frequency domain characterization.

Research by Yang et al [68] later presents a simpler model of the hotspot as one of low resistance installed in a circuit equivalent to a single diode. This

resistance induces the PV's current to flow back to the PV cell, which generates the reverse bias phenomenon inside and causes a reduction of the output current. Another research by Alsafasfeh et al [69] presents the Simple Linear Iterative Clustering (SLIC) Super-Pixel technique as the technique for hotspot detection. The topology is to decompose a PV's thermal image into small homogeneous regions before applying the SLIC to determine the defected cells. The experimental results confirm its efficiency; however, several parameters are necessary to be assigned. Another method is presented by Dong et al [70] using the door connection method, which utilizes a new PV cell connection pattern that can detect the hotspot. Along with research by Kim et al [66], the work presents the novel complex-total-cross-tied array structure and a hotspot detection scheme. The method is implemented based on current monitoring and comparison with computational values. However, the precise value is strongly dependent on many environmental parameters.

Interesting detection method is presented by Rossi et al [67]. By measuring the PV's current in each module, the current is compared to the reference PV cell which operate in normal condition. The system consists of set of current sensors connected to each module, with the hysteresis comparators to detect the hotspot. The results confirm the efficiency of the method under different levels of irradiation; however, the reference PV cell needs to be completely undetected in order to achieve the accurate results.

As mentioned in reviewed works, several hotspot models and detection methods are presented and confirmed their accuracy and efficiency. Since hotspot is the blind fault and has a relationship with PV material property, making the detection not only depending on electrical characteristics, also the material parameters need to be considered. Overall, the main problems for the reviewed methods are the material properties, environmental parameters and the equipment's requirements (i.e. the irradiation and temperature sensors, complex control circuits). Hence, it is the contribution to implement the hotspot detection together with the global MPPT algorithm, which is never presented in other published papers.

3.3 Analysis

For a better understanding of PV operation, it is important to investigate the PV cell model under normal and hotspot conditions. In this section, the single-diode model (described in section 2.3.1) is used. The circuit consists of a current source I_{ph} connected anti parallel with a diode, including series resistor R_s and parallel resistor R_p.

According to the literature reviews in section 3.2, several of hotspot models are presented. The models can effectively present the hotspot condition but still require complex calculation and implementation. In this case, the author uses the cited model proposed by Yang et al [68] due to the simplicity and effectiveness. Also, the model is based on DC circuit in which is capable to the proposed global MPP algorithm. The proposed work shows the model as the small resistance installed in a PV's single-diode equivalent circuit. Figure 3.5 presents the simplified circuit model of a hotspot defected cell.

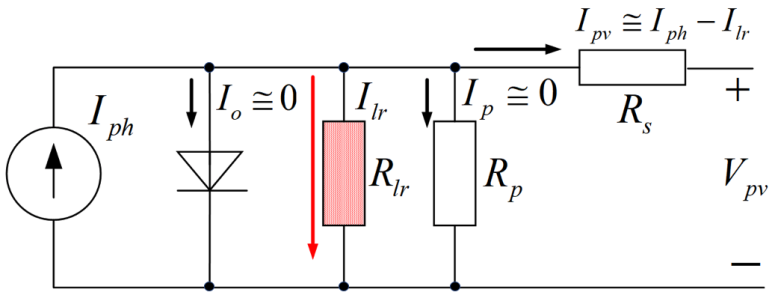

Figure 3.5: Simplified model of a hotspot defected cell

From the equivalent circuit, the small resistor R_{lr} presents the resistance of the defective part of the PV cell. When the PV system operates, R_{lr} induces the current I_{lr}, consequently reduces the output current I_{pv}. Furthermore, the increase of I_{lr} causes the high power dissipation. The defective PV cell heats up due to the rise of cell's temperature, if this heat is stored without any fault detection, damage can occur as the burnt on the PV panel's surface. Also, more absorbed temperature achieves.

In order to support the effectiveness of the model, it has been stated in research papers about the shunt resistance representation in hotspot condition. Roy et al. [71] describes that the shunt resistance create a mismatch and lead to hotspot formation that can thermally destroy the module. Resistance are formed due to several material degradation reasons. Moreover, Rossi et al. [67] confirms that the existence of shunt resistance leads to the exhibit of a large inverse current. Although we acknowledge the cause of hotspot occurrence, the observation and detection over time are difficult. Since the circuit inside the PV cell is not accessible; therefore, direct measurement of the cell's output current is not applicable [72]. Instead, the indirect measurement is performed by using the I-V and P-V characteristic curve.

Before analyzing the PV's characteristics, the simulation of the PV model in the cell's scale is implemented. The model is implemented based on the PV module structure described by PVEducation [73], which consists of many interconnected cells connected in series encapsulated into a single stable unit. In this chapter, the simplified PV model without bypass diode is used since the full hotspot defected is the main concern. The parallel resistor R_p in normal condition is equal to 19.5 Ohm, for the hotspot case it is assumed the value of R_{lr} equals to 0.1 Ohm which is 0.5% of the R_p in normal condition. Figure 3.6(a) shows the graphical picture for the PV module with different levels of hotspots from 0% to 100% with an increment of 10% by dividing the PV cell into ten groups, and figures 3.6(b) and 3.6(c) display the I-V and P-V curves for each hotspot levels.

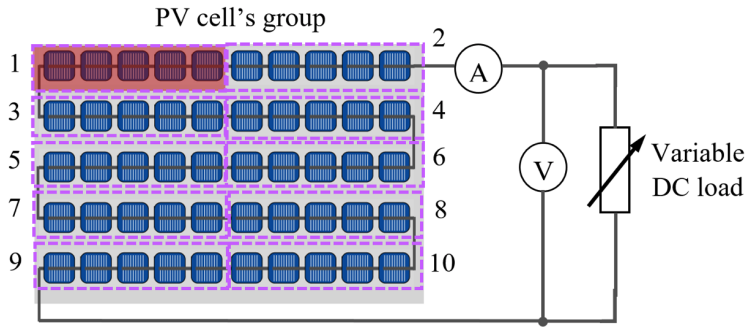

(a) Simulation circuit diagram for different levels of hotspots in a PV's panel

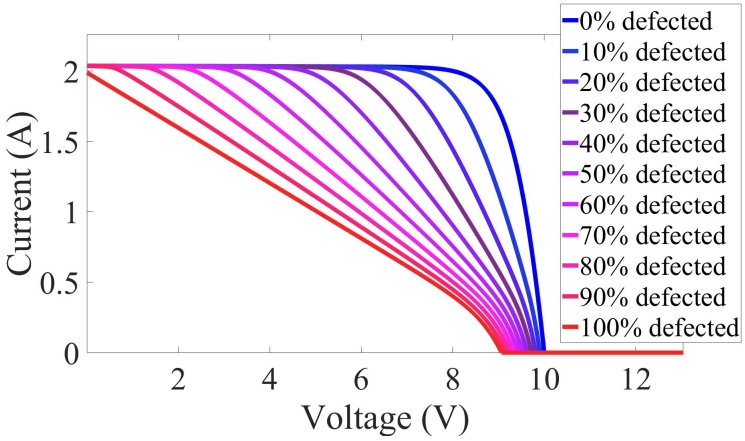

(b) I-V characteristic curves for different levels of hotspots

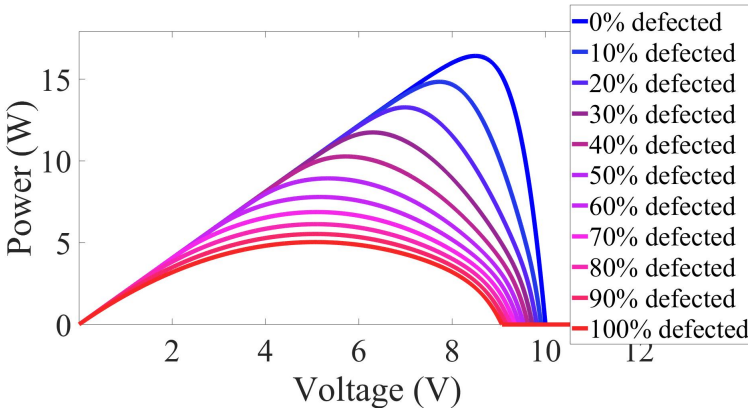

(c) P-V characteristic curves for different levels of hotspots

Figure 3.6: Diagram for the PV module and characteristic curves at different levels of hotspots.

Results observe from the I-V curves in figure 3.6(b) show that the rate of decrease for the PV's current varies when hotspot occurs. Especially in the high percentage of the hotspot, the current drops at a lower PV's voltage when compared to the non-defected cells.

The value of PV's current effects due to the low shunt resistance R_{lr}. Since R_{lr} varies from the impurities of the material, the percentage of R_{lr} value is assumed. The occurrence happens from the existence of R_{lr}, which reduces the current to

cause them to flow out of the cells. Hence, a linear decrease in the I-V curves' region can be identified. Furthermore, the decrease of the current consequently reduces the amount of power generated from the panel, as shown in the P-V curve in figure 3.6(c). The result from the I-V and P-V curves describes the operation of PV cells when the hotspot happens.

The analysis concludes as the number of series-connected panel increases, the more the reverse bias region is divided in the I-V curve. Although the position of the reverse bias region varies from the different specification, their trends can be observed. The hotspot occurrence can be found by detecting this reverse bias region, using the linear decrease of I_{pv}. Assuming the certain irradiation and temperature conditions (from the curve in figure 3.6(b)), when the full hotspot happens, the linear decrease of the PV's current can be detected. By designing the tracking starting from approximately 50% of the whole curve's voltage range, the range for detecting the hotspot can be limited. The achieved information can help to design the hotspot-detecting algorithm.

3.4 Proposed Hotspot Detection Algorithm

In this section, the proposed hotspot detection algorithm is explained. The algorithm contributes the advantage in terms of the ability to integrate with the proposed global MPPT algorithm in chapter 2 (section 2.4.2). The algorithm makes the online detection possible while PV system is under operation, contributing the faster detection.

The flowchart in figure 3.7 and 3.8 show the flowchart of the global MPPT algorithm integrated with the simplified hotspot detection method. The algorithm consists of three main parts including; (1) the main program (2) the irradiation estimation, shading detection and global MPPT, and (3) the proposed hotspot detection. From figure 3.7, the algorithm begins with the main program and the initialization by inputting PV module parameters and array's dimension. Onwards, the program proceeds to the shading detection and global MPP tracking which follows the same procedures stated in section 2.4.2.

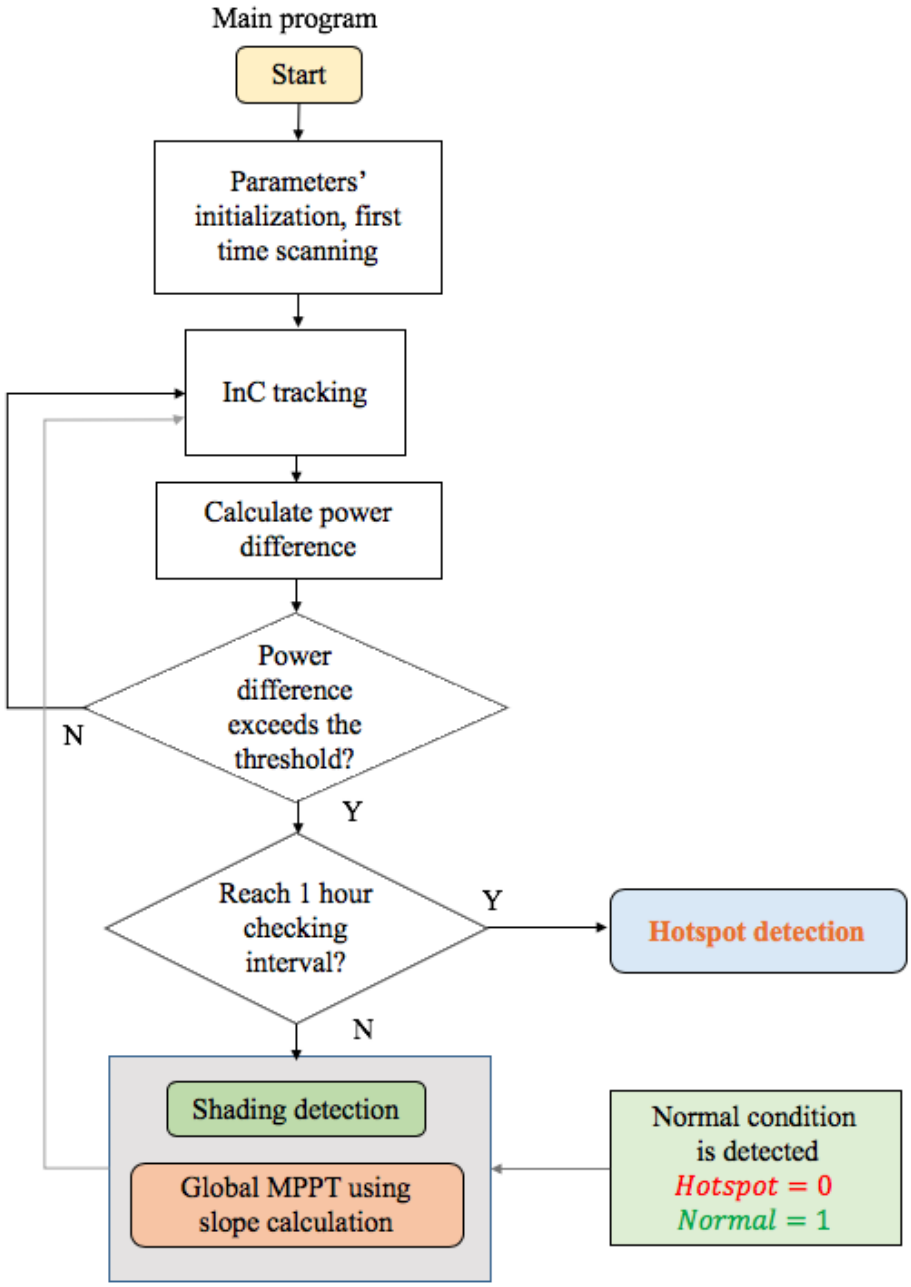

Figure 3.7: Main program and proposed global MPPT algorithms

Figure 3.8 presents the proposed hotspot detection algorithm integrated into the global MPPT. The program contains the first and second reference points measurement and slope calculation.

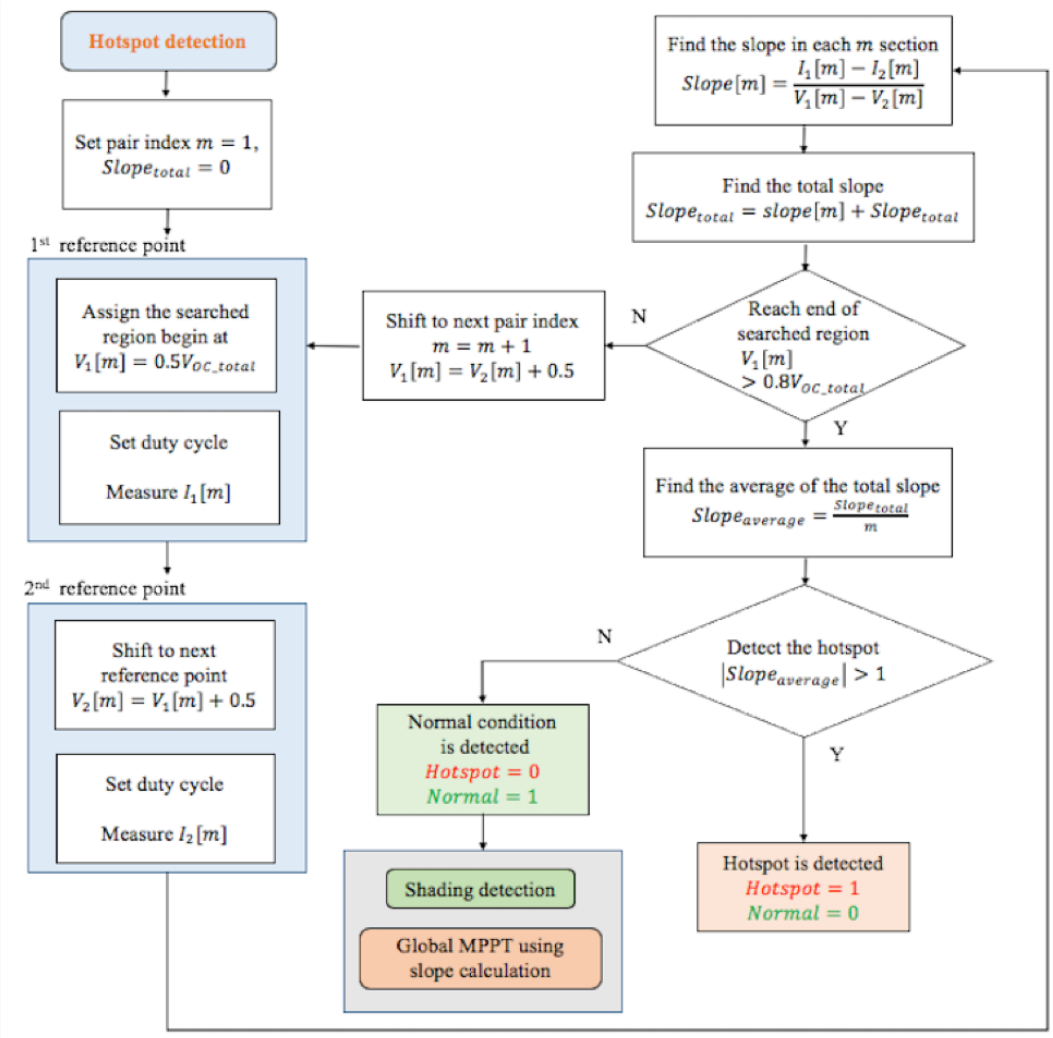

Figure 3.8: Proposed simplified hotspot detection algorithm

For the hotspot detection, the algorithm calls for the detection every 1 hr after the power difference is detected. From the flowchart, the indicators of PV's status ($Normal$ and $Hotspot$) are assigned. The algorithm starts from 50% of V_{OC}, the voltage assigns as the first reference voltage $V_1[1]$ and the current is recorded as $I_1[1]$. Step repeats after shifting the voltage by 0.5 V to the next point $V_2[1]$ and recording the current $I_2[1]$. Consequently, the algorithm calculates the rate of change called $Slope[m]$ between two current points with respect to the voltage,

the calculation shows in equation 3.1.

$$Slope[m] = \frac{(I_1[m] - I_2[m])}{(V_1[m] - V_2[m])} \tag{3.1}$$

Figure 3.9 shows how the example I-V curve used for calculating $Slope[m]$.

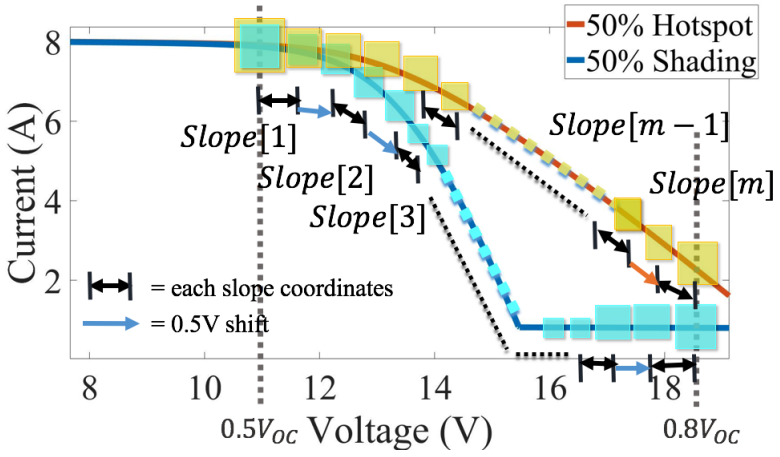

Figure 3.9: Slope calculation method for hotspot and normal condition PV array

Presented in figure 3.9, the gray dash-line indicates the slope calculation region. From the analysis of PV curve in section 3.3, the region starts from 50% to 80% of the total V_{OC}. The calculation starts from the first two current values (presented by the yellow rectangles) each 0.5 V apart, the first slope ($Slope[1]$) is achieved. Then the calculation repeats by shifting to the next 0.5 V until the algorithm reaches 80% of total V_{OC}, the average slope $|Slope_{average}|$ is calculated.

In order to differentiate the occurrence of hotspot from shading, the algorithm uses the threshold to compare the calculated $|Slope_{average}|$. For the hotspot, the characteristic curve shows the gradual decrease of PV's current according to low shunt resistance in the model. On the other hand for the normal condition PV cell, due to the high shunt resistance value, the current shows low slope value even though shading occurs. The threshold of 1 is achieved from the simulation test with more than 15 samples of different hotspots and shading locations. If $|Slope_{average}|$ is greater than the threshold, the program estimates the hotspot

condition occurs and the *Hotspot* indicator triggers the status from 0 to 1 after detection completes. On the other hand, if the slope is less than the threshold, the *Normal* status remains before proceeding to the global MPPT for tracking the maximum power.

The idea of slope calculation makes the proposed algorithm can detect the hotspot that occurs in the PV array, also differentiate the normal condition and integrated the proposed algorithm to the MPPT. Moreover, the program can track the global MPP after shading happens.

3.5 System Implementations and Results

The hotspot detection simulation is performed to test the performance of the proposed algorithm. The system is tested with the medium scale PV array. Figure 3.10 presents the system's diagram which categorizes according to the number of the panel containing faults.

The implementation consists of small-scale PV system includes 5 × 5 PV arrays with the rated power of 83.28 W per module (I_{sc} of 8.62 A and V_{oc} of 12.64 V). A DC-DC converter is implemented together with the MPPT controller to control the input voltage and current from PV to reach its maximum power point. As described in the flowchart in figure 3.7, the duty cycle from the algorithm indicates the operation of the converter. Only centralized current and voltage sensors are used. The switching frequency of the PWM signal generated from the MPPT unit is 10 kHz with the sampling period of the sensors as 0.1 ms.

Cases are divided based on the different number of faulted panels (2, 3 and 4 panels), as presented in figure 3.10. Highlighted colors indicate the fault locations for each case. The low shunt resistance is assumed as 0.1 Ohm for the hotspot condition and the irradiation of 500 W/m^2 for the normal condition.

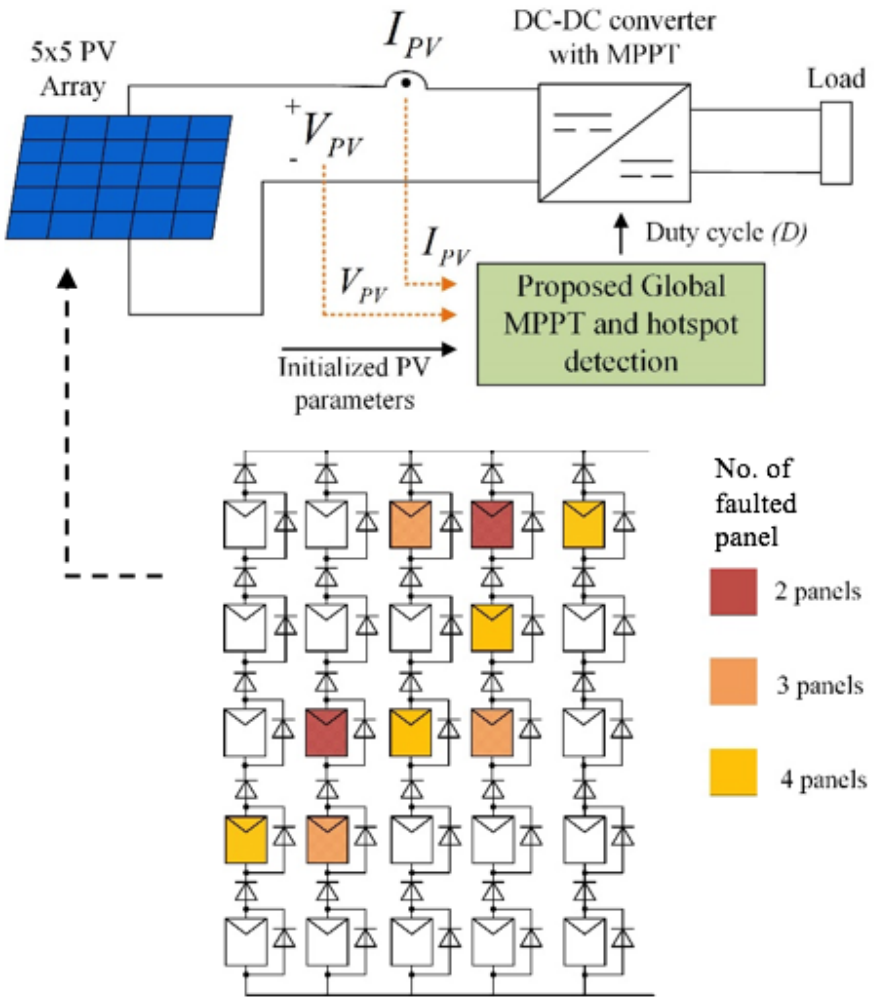

Figure 3.10: Second implementation's simulation circuit diagram for hotspot detection

Figures 3.11, 3.12 and 3.13 show the graphical results of the proposed algorithm for each number of faulted panels. Parameters include the PV's current and voltage, tracked power and status indicators.

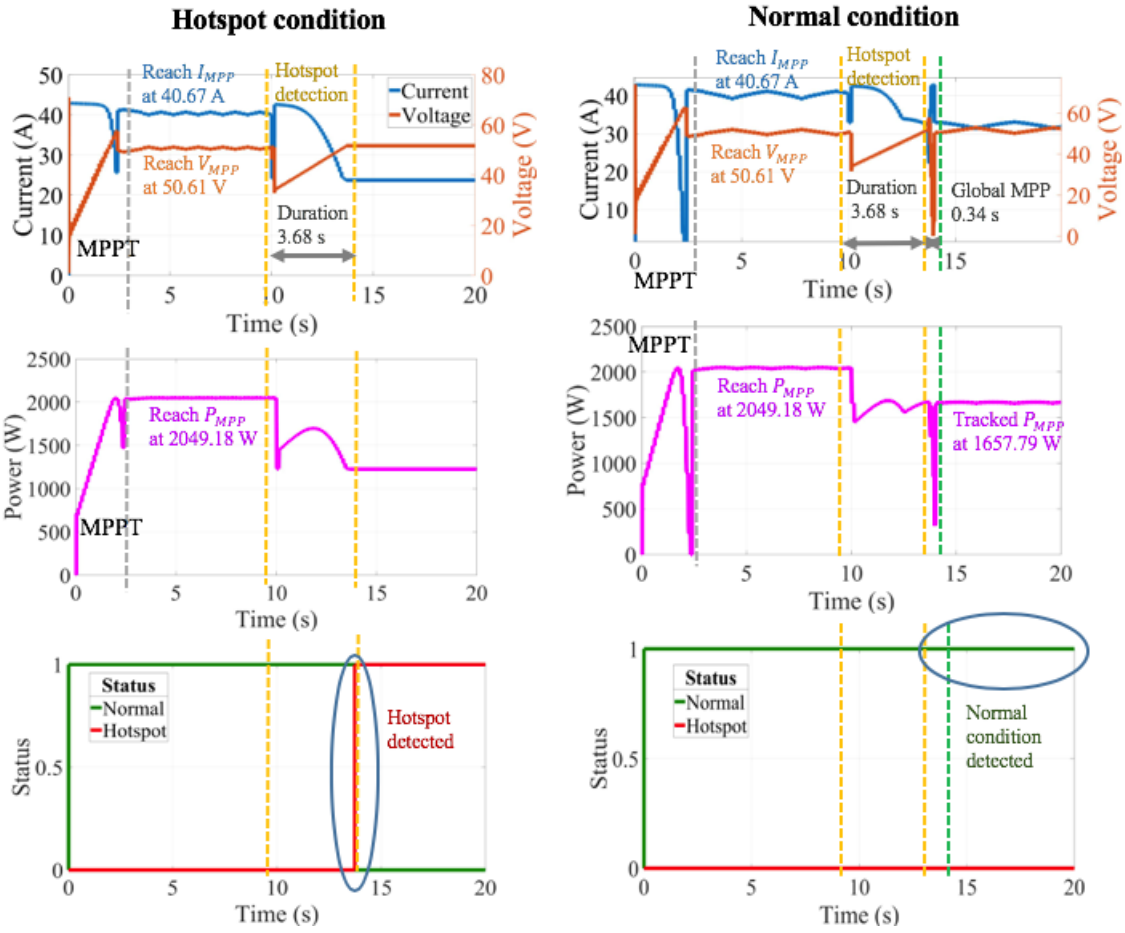

Figure 3.11: Hotspot and normal condition detection for 2 panels case

Figure 3.11 presents the result for 2 panels case. The program starts with the first MPPT to determine the maximum power, successfully reaches 2049.18 W. This takes approximately 2.30 seconds. Afterward, the hotspot occurs at 10 seconds, the program starts to identify the hotspot by calculating $Slope[m]$ and compares to the determined threshold. If the hotspot is detected, the status indicator triggers from 0 to 1 for indication in which the duration takes 3.68 seconds. On the other hand, the program determines the status as the normal condition in which proceeds to the proposed global MPPT in section 2.4.2 which takes 0.34 seconds to track the new MPP at 1657.79 W. Therefore, the status remains at normal condition.

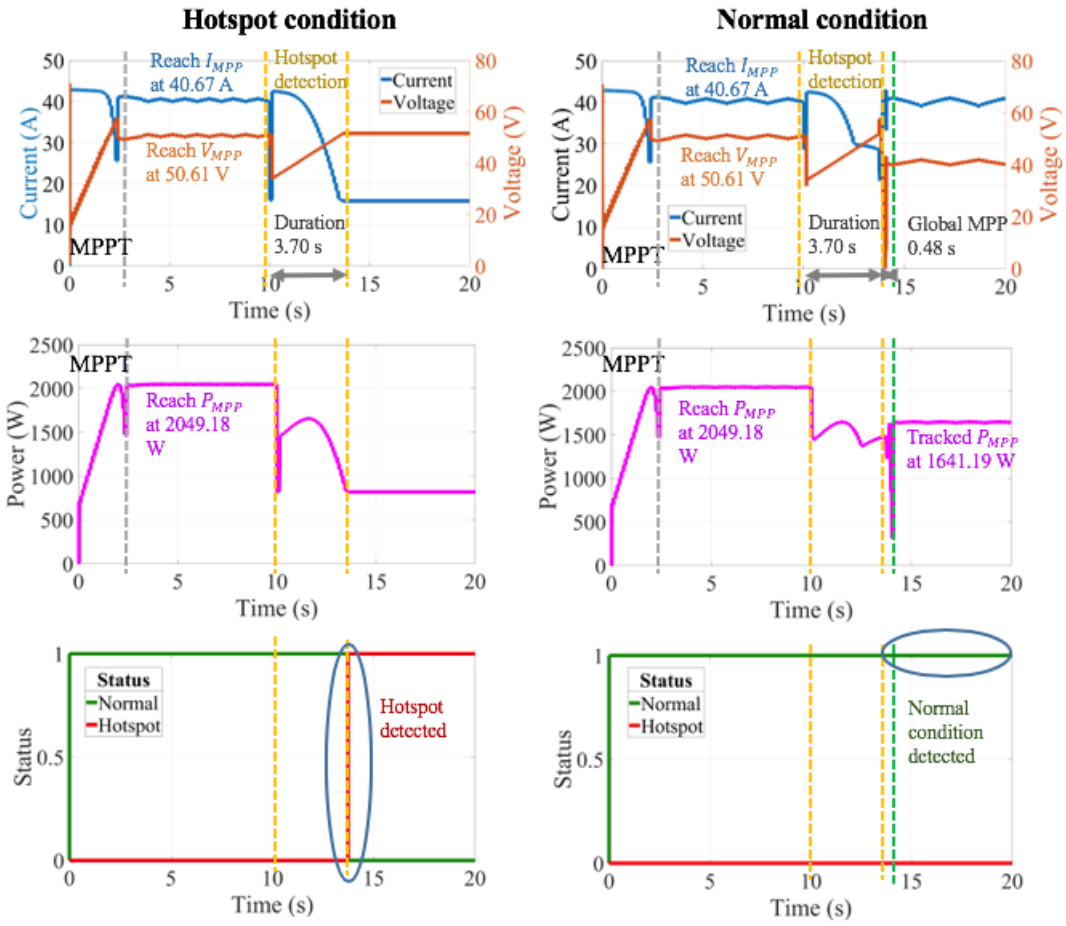

Figure 3.12: Hotspot and normal condition detection for 3 panels case

For 3 panels case in figure 3.12, the proposed detection method succeeds to detect the hotspot and normal condition. Starting off with the first MPP and continuing towards the detection, the duration takes 3.70 seconds then the status triggers. In contrast, when shading occurs, the programs proceed to global MPP and track the power at 1641.19 W.

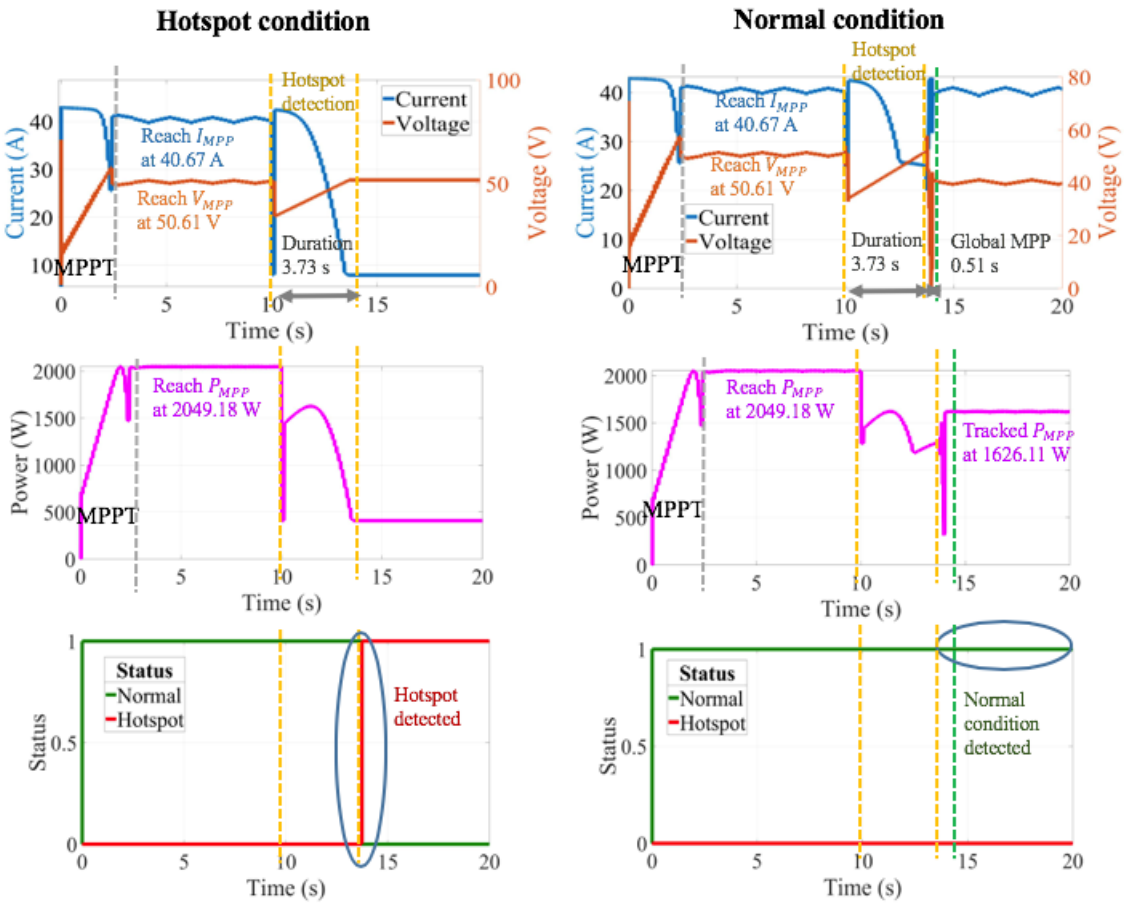

Figure 3.13: Hotspot and normal condition detection for 4 panels case

Accordingly, figure 3.13 illustrates the detection of 4 panels case. Similarly characteristics to the previous case, the algorithm detects the hotspot with a duration of 3.73 seconds before the status triggers. The detection confirms successful results. Alternatively, the algorithm is capable to detect the shading and track the new global MPP at 1626.11 W.

Table 3.1 indicates the numerical results of the second implementation including value of the averaged slope, detection time used and status indicator.

Table 3.1: Numerical results for the hotspot and normal condition detection at different hotspot locations

Case	$\lvert Slope_{average} \rvert$ (A/V)	Detection time (s)	Indicator
2 panels	1.08	3.68	*Hotspot*
	0.59	4.02	*Normal*
3 panels	1.52	3.70	*Hotspot*
	0.79	4.18	*Normal*
4 panels	1.93	3.73	*Hotspot*
	0.87	4.24	*Normal*

The numerical results in the table proves the capability of detecting the hotspot by using the proposed algorithm. For the normal condition by using the combination of the global MPPT method, the system provides more function and allows the power tracking to restore back to the PV's highest efficiency. The robustness of the system is shown by the response after the detection completes. Although the detection algorithm calls periodically, the system can recover back to the stable operation with the maximum tracked power. The settling time is within 5 seconds.

3.6 Conclusions

Hotspot causes not only the decrease of generated power from PV system but also the damage to the PV material if not detected effectively. This chapter presents the hotspot detection algorithm in the PV array using the simplified model. The model is implemented based on the low shunt resistor, which expresses the degradation of the material. Consequently, the proposed algorithm shows the accuracy and efficiency to detect the hotspot, confirmed by the simulation in different PV specifications and hotspot positions. In addition, the algorithm is capable to integrate with the irradiation estimation and global MPPT algorithm presented in chapter 2, contributing the integrated function to the

MPPT system. Correspondingly, the algorithm can detect the hotspot and differentiate the normal condition from the PV's current slope calculation in the specified region. The total detection time takes less than 6 seconds on average and the indicator shows the accurate status after detection completes.

Further works from this chapter include the improvements of the hotspot model, which suits the standard PV module with the cluster's arrangements. Moreover, the temperature estimation of the PV cell is investigated to clarify the damage level of the hotspot. The details are presented in chapter 4.

Chapter 4

Hotspot Model in Cluster's Structure with Hotspot Detection Algorithms and Temperature Estimation for Photovoltaic Systems

According to chapter 3, based on published researches, survey data, and the analysis, hotspot condition causes a considerable decrease in the generated power by the whole PV system. The simplified hotspot model is used to analyze and develop the hotspot detection algorithm. The results confirm the accuracy and efficiency to detect and indicate the fault in different PV sizing and locations. In this chapter, the improvement of the hotspot model and detection method are presented. The improved model presents higher efficiency, which shows more compatibility with the practical PV module's structure. Since the implementation of the practical PV module in the real installation is built using the cluster's structure; therefore, the proposed model should be more elaborate and capable to work in practice.

With the information from the IEC 61215 in section 3.1, the hotspot results

in the reversed bias problem in a defected cell. Power dissipation generated in the cell is proportional to the increased PV's reversed bias current. Two factors related to power dissipation include (1) the value of shunt resistor and (2) level of irradiation on the hotspot's cell. Apart from the hotspot model improvement, the model also presents a clear reversed bias characteristic of the hotspot in order to implement an effective configuration. Studies related to material defection (value of the shunt resistance) and different irradiation levels are presented.

The main context of this chapter is to improve the hotspot model described in chapter 3 in order to make the model capable to operate with the practical PV module's structure. The model is analyzed and compared to the IEC standard and other published works to make sure of the highest capability, also identifies the accelerated factors that generate the hotspot. The improved hotspot detection algorithm is developed and presented in the form of the flowchart. After detection, the algorithm displays the module's status using the indicator signal, giving the usefulness to display the detection results. Furthermore, not only the hotspot detection is presented in the algorithm, the second stage which is the temperature estimation is also shown, since temperature is used as the parameters to determine the damage level of the hotspot. If the hotspot's temperature can be estimated, it is possible for the algorithm not only to detect the hotspot but also to indicate how severe the hotspot occurs in the cell.

Continuing from chapter 3, the usefulness of this research is the improved proposed algorithm (implemented from practical three cluster's model) can accurately detect the hotspot and differentiate from normal and shading conditions. The algorithm uses mathematical expressions to derive the hotspot model under reversed bias condition. Graphical and numerical results display the presence of the hotspot. Importantly, the contribution of the work is practical capability. Since most researchers develop the detection method based on single and two clusters model, the proposed method shows more development and compatibility with the practical PV standard. Significantly, the proposed method uses the concept of the increased bias current under reversed bias condition to detect the hotspot. The algorithm estimates the rate of change of PV's current over the

operating time to detect the hotspot over the degradation. In terms of implementation, the design of the system's implementation is simple with only centralized current and voltage sensors. Apart from the detection, this chapter also introduces and discusses the hotspot's temperature estimation method which has the benefit to indicate how severe the hotspot occurs in the cell, contributing more advantages to the PV's maintenance stage.

The chapter is outlined as follows. Firstly, section 4.1 states the problems of hotspot toward PV system in the reversed bias condition and temperature estimation. The chapter continues with section 4.2, presenting the elaborate hotspot model in the cluster's structure using the voltage-controlled current source model and analysis of factors that accelerate the hotspot condition. The proposed detection algorithm is presented in section 4.3 with the system's implementation and results to evaluate the algorithm in section 4.4. The implementation consists of hotspot detection cases in different sizing, various irradiation, and material defection. The chapter ends with the discussion of temperature estimation in section 4.5 for further understanding of the linkage between electrical engineering and material science concepts used to develop the estimation method.

4.1 Problem Statement

As explained in chapter 3, the hotspot model is introduced for modeling the PV module operation. Since it is impossible to extract and access the hotspot directly from the PV cell, the hotspot is modeled using the electric circuit to represent the operation.

According to section 3.3, the simplified low shunt resistance model is used to represent the defective part of the PV cell under hotspot conditions. When the shunt resistance reduces due to material degradation, the circuit induces the current which causes the power dissipation. Also, the simplified model is analyzed and used to design the hotspot detection algorithm. To improve the existed model, more standards and practical specifications are considered. As stated in the chapter's introduction, the practical PV module is implemented

using the cluster's structure. Explained by work in [76], most commercial PV modules are formed by a group of PV cell serially connected and include three bypass diodes. Some of the PV modules are offered without bypass diodes. Figure 4.1 shows the PV module model in three cluster's structure.

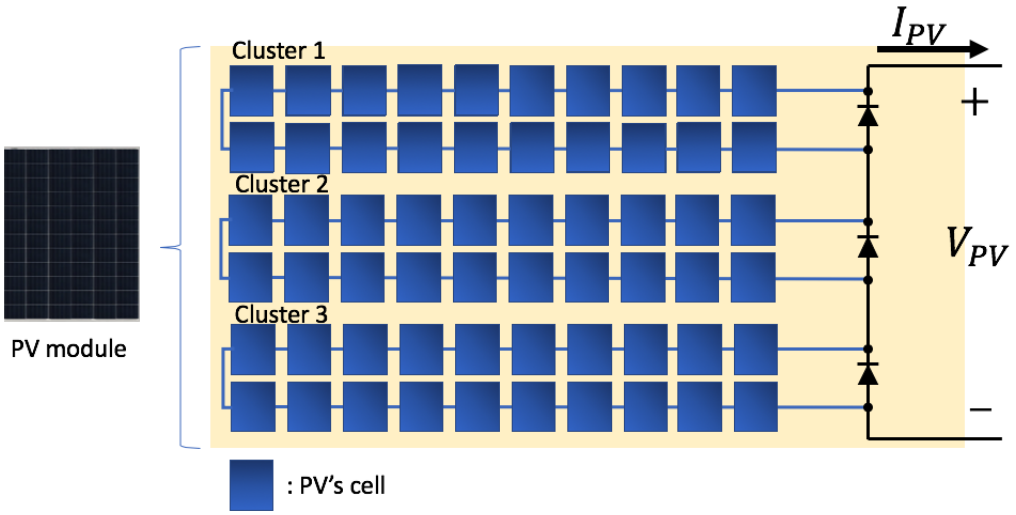

Figure 4.1: PV module model in three cluster's structure

From figure 4.1, the standard model consists of 60 PV cells is divided into three clusters. Each cluster consists of 20 PV cells connected in series and is separated by the bypass diode. This diode helps to mitigate the exceed current and prevent from the hotspot. Although most PV installations include the bypass diode to protect the effects of shading and hotspots, however; the diode is still insufficient for hotspot prevention. Work done by Bharadwaj et al [77] states the cause of hotspots in the presence of large mismatches such as partial shading, and also shows that the installation of the standard bypass diodes does not eliminate hot-spotting inside the array. The weakness of bypass diode is also mentioned by the work in [78] and [79], which describes that the diode helps to reduce the magnitude of the hotspot. However, a moderate hotspot that accelerates degradation can still occur.

As a result, the PV module operates as the reverse-bias diode which dissipates power and consequently heats up. Moreover, according to Rossi et al [67], the

time required for the heating to generate permanent damage in a PV cell under hotspots strongly depends on two factors—environmental parameters (from shading and temperature) and impurities in the materials. For this reason, it is essential to find a practical solution for detecting hotspots to prevent severe damage.

Furthermore in IEC 61215 standard, although the hotspot effect in shading condition is explained; the document does not describe the effect of the material's property degradation. Since the degradation in the cell can affect the hotspot model parameter and increase the induced current, the increase of the induced current can occur. Therefore, the effects of material matters should be considered. In addition, after the algorithm successfully detects the hotspot, further process in indicating how severe the detected hotspot is performed. This process is relatively challenging for researchers due to the requirement of material specification and several factors.

4.2 Analysis

This section introduces the hotspot model use the cluster's structure, with the analysis of hotspot condition under different material's defection and irradiation levels.

4.2.1 PV Cell Hotspot Model

The cited hotspot model used in this section is presented by Rossi et al [67]. The model is implemented based on the single-diode DC model with the additional voltage-controlled current source (VCCS) connected to the shunt resistance branch. The reversed bias current I_{BR} is generated.

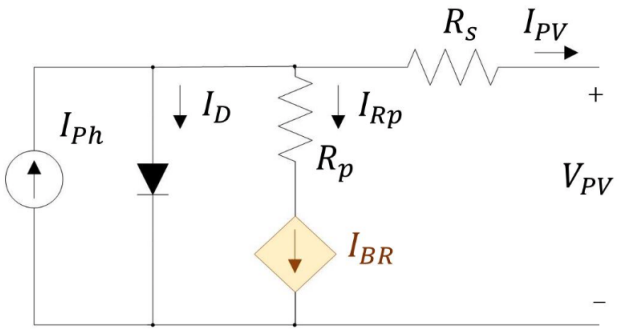

Figure 4.2: PV hotspot model with VCCS and shunt resistance [67]

When the cell is exposed to sunlight, the source generates the current is proportional to the irradiation level. Equation 4.1 shows the expression of the currents in the circuit according to Kirchoff's current law.

$$I_{PV} = I_{ph} - I_D - I_{Rp} \tag{4.1}$$

The reverse bias of the cell is represented by the polarity of the PV's output voltage V_{PV}. During normal condition ($V_{PV} > 0$), the current source I_{BR} does not generate additional current; therefore, the circuit operates in normal condition as the PV single-diode model. The current I_{BR} generated from the additional VCCS expressed shown in equation 4.2 [67].

$$I_{BR} = \begin{cases} 0 & , V_{PV} > 0 \\ \alpha(\frac{V_{PV}}{R_p})(1 - (\frac{V_{PV}}{V_{BD}}))^{-m} & , V_{PV} \leq 0 \end{cases} \tag{4.2}$$

From equation 4.2, α and m are the fitting parameter (α =1.93 and m = 1.10 for the crystalline Silicon) and V_{BD} is the cell's breakdown voltage. When V_{PV} turns negative, the current source generates I_{BR} in the exponential trends.

Figure 4.3 presents the current-voltage (I-V) characteristic curve of the hotspot cell, assuming the 500 Ohm shunt resistor R_p with the irradiation at 1000 W/m^2.

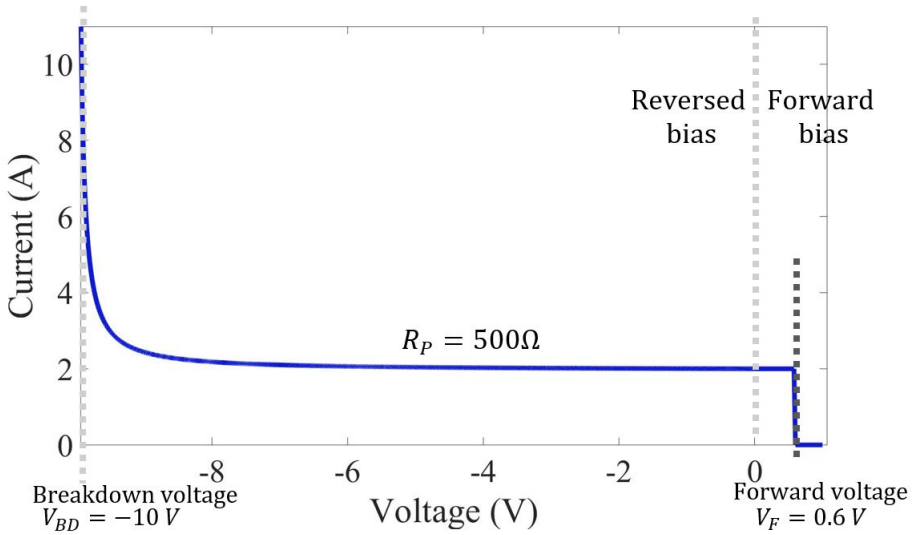

Figure 4.3: I-V characteristic curve of the hotspot cell in forward and reversed bias conditions

As shown in figure 4.3, the curve presents the PV's current in two operating regions including forward and reverse bias. When V_{PV} is positive, the cell will operate in forward bias in which the cell's diode turn-on when reaching the diode's forward voltage V_F of 0.6 V. PV's current increases to approximately 2 A (current level at 1000 W/m^2). In contrast, when V_{PV} turns negative, the reverse bias condition starts to occur. The graph shows the PV's current starts to incline exponentially, especially when reaching the breakdown voltage of 10 V. This sharp increment causes the overheat inside the cell's surface and leads to damage.

4.2.2 Effect from the Shunt Resistance

As described in section 4.1, since the material's degradation in the cell can affect the hotspot model parameter and increase the induced current; therefore, the analysis considers the effect of the shunt resistance towards the performance of the PV module. A detailed investigation is performed by considering the value of shunt resistance (R_p), as shown in the I-V curves in figure 4.4.

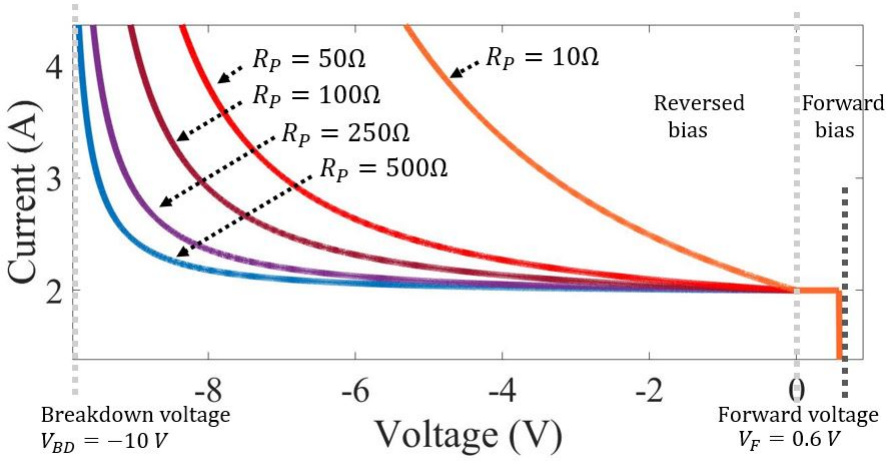

Figure 4.4: I-V characteristic curves of the hotspot cell at different shunt resistances

From figure 4.4, the curve shows the effect of shunt resistance values on the reversed bias current in the cell. The result presents the low resistance value generates a large current. Especially for the lowest resistance value of 10 Ohm, the current increases significantly at approximately -5 V, which is less than the value of the breakdown voltage. The low resistance value can be reflected as the degradation of the material which induces more current and more power dissipation.

4.2.3 Effect from the Level of Irradiation

Due to the dependence of weather, especially irradiation, it is necessary to evaluate the hotspot effect at different irradiation levels. By using 500 Ohm shunt resistance, figure 4.5 shows the effect of irradiation on the PV's current during hotspot condition.

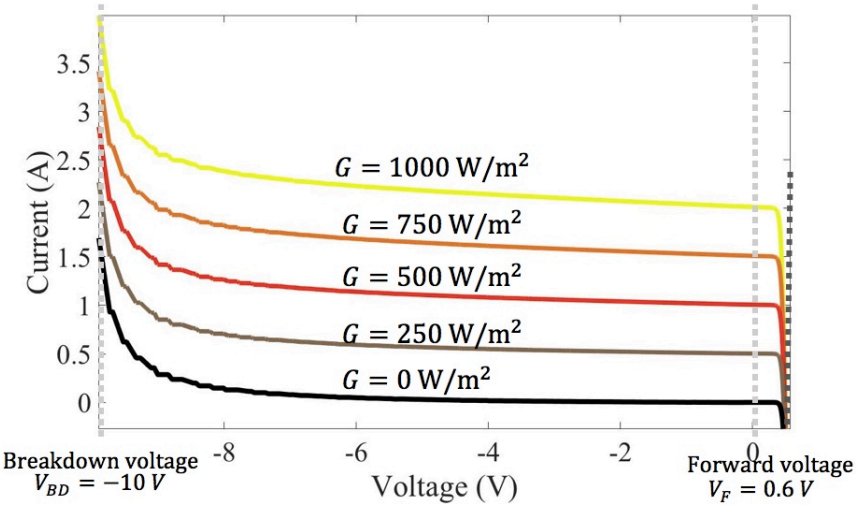

Figure 4.5: I-V characteristic curves of the hotspot cell at different irradiations

Figure 4.5 highlights the different levels of current which are in proportional to the irradiation. The graph shows that the more irradiation inputs to hotspot's cell, the more generated current causes a higher power dissipation level.

4.2.4 Effect of Hotspot to PV Module in Cluster's Structure

In this part, the effect of the hotspot in the PV cell is analyzed with the cluster's structure in the single PV module. Figure 4.6 shows the PV module in three cluster's structure with one hotspot's cell highlighted. The hotspot is implemented with the PV cell VCCS and shunt resistance model.

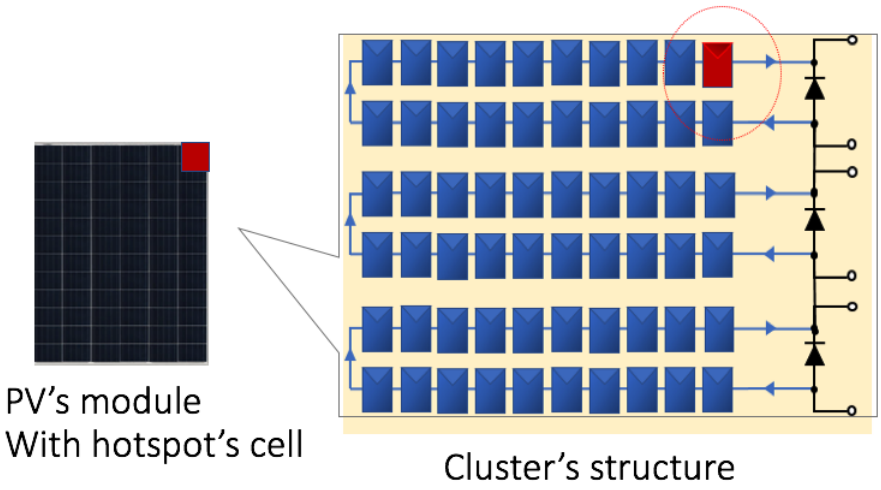

Figure 4.6: Hotspot's cell in PV module model in three cluster's structure

Table 4.1: Parameters for a single PV cell under STC

Parameters	Value
Maximum power	0.76 W
Current at maximum power	1.95 A
Voltage at maximum power	0.40 V
Short-circuit current	2.00 A
Open-circuit voltage	0.50 V
Shunt resistance	35.54 Ohm
Series resistance	0.02 Ohm

Table 4.1 presents the parameters' specification of the PV cell under STC. By using the configuration in figure 4.6, the parameters of the hotspot's cell, also the PV module under normal and hotspot conditions are displayed. The condition for the hotspot's cell consists of the irradiation of 300 W/m^2 and shunt resistance of 35.54 Ohm. Figure 4.7 presents the I-V curves of the hotspot's cell and the whole PV module.

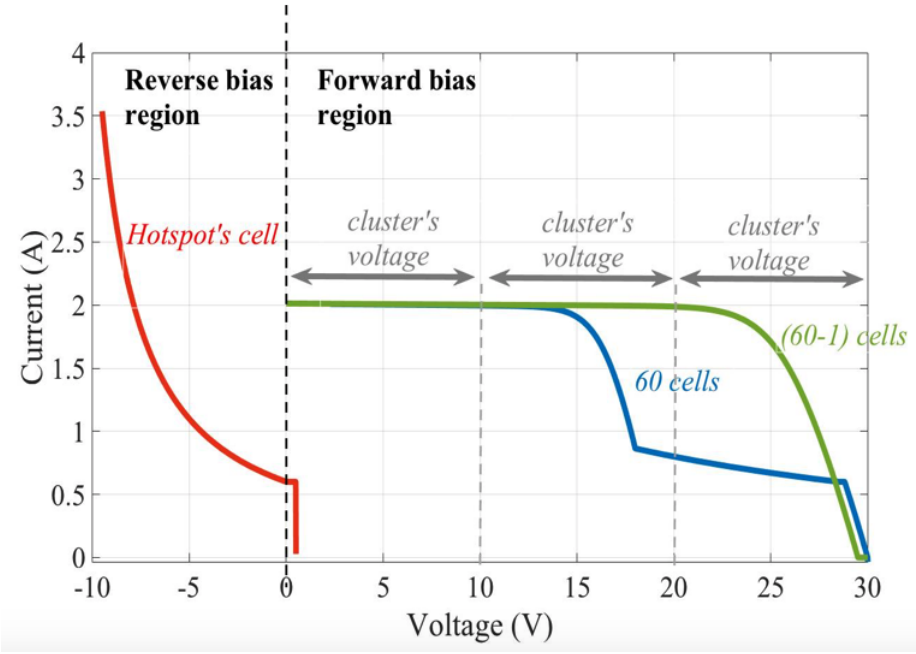

Figure 4.7: I-V characteristic curves of the hotspot's cell and whole PV module

From figure 4.7, the I-V curves show the PV's current characteristic under forward and reverse bias regions. The result shows the capability to match the information presented by the IEC 61215 standard explained in figure 3.3.

Under reversed bias region, the red graph displays the cell's current which increased exponentially from the current value at 300 W/m^2 before reaching the breakdown voltage at -10 V. Moreover, the blue graph displays the linear decrease on the whole module's current, existing at cluster's total voltage (at 20 V). In this case, although the maximum power of the module is not significantly different compared to the normal condition, the high power dissipation can cause the cell to overheat and bring damage. Figures 4.8(a) and 4.8(b) conclude the effect of shunt resistance and irradiation toward the module's current.

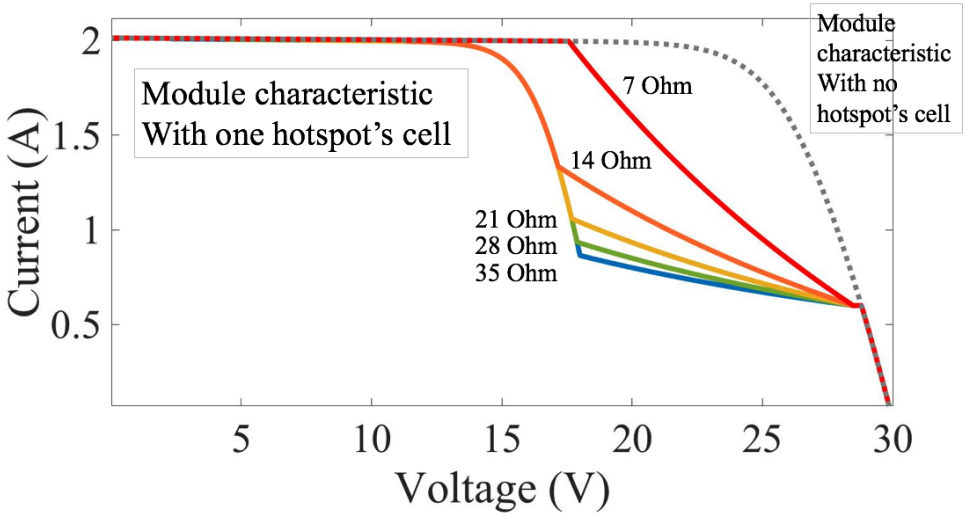

(a) Shunt resistance effect

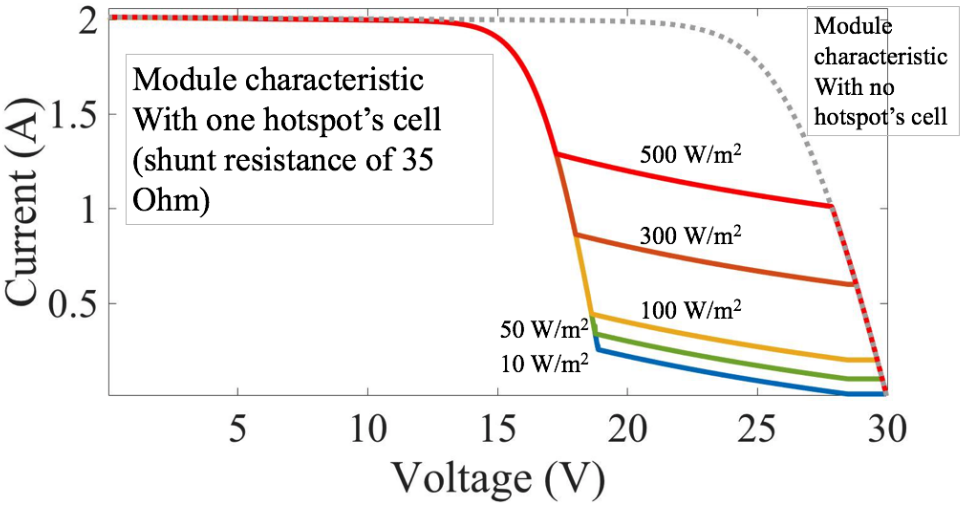

(b) Irradiation effect

Figure 4.8: PV module characteristic with the effect of shunt resistances and irradiations

Figure 4.8(a) presents the inverse proportional relationship between the shunt resistance and power dissipation level. Less shunt resistance shows a higher power dissipation, observing from the area under the PV's current. In addition to the

resistance, the irradiation also affects the amount of power dissipation. Confirming by figure 4.8(b), the information presents the directly proportional relationship of the irradiation and power dissipation. The dissipation contributes to high-temperature rises in the hotspot's cell. If the cell operates close to the breakdown voltage, the level of dissipation can increase exponentially, causing damage to the cell. The achieved information from the analysis is used to design the hotspot-detecting algorithm presenting in section 4.3.

4.3 Proposed Hotspot Detection Algorithm for PV Module in Cluster's Structure

This section presents the general system implementation with the improved hotspot detection algorithm for PV module in the cluster's structure. Implementation shows in figure 4.9. The system is implemented by PV array (two series-connected modules, one module contains the hotspot's cell), the boost converter with a duty cycle control and the constant load. The reversed bias voltage V_{REV} is assumed to decrease over the system's operating time. This decreased rate represents the degradation due to the hotspot. In this case, V_{REV} has a decrease rate of -0.21 V per second. According to the decrease of V_{REV} over time, the gradual increase of the PV's current in reverse bias region can be observed from the whole module's I-V curve. Therefore, if the system can determine the increase rate of change of PV's current, the hotspot can be detected.

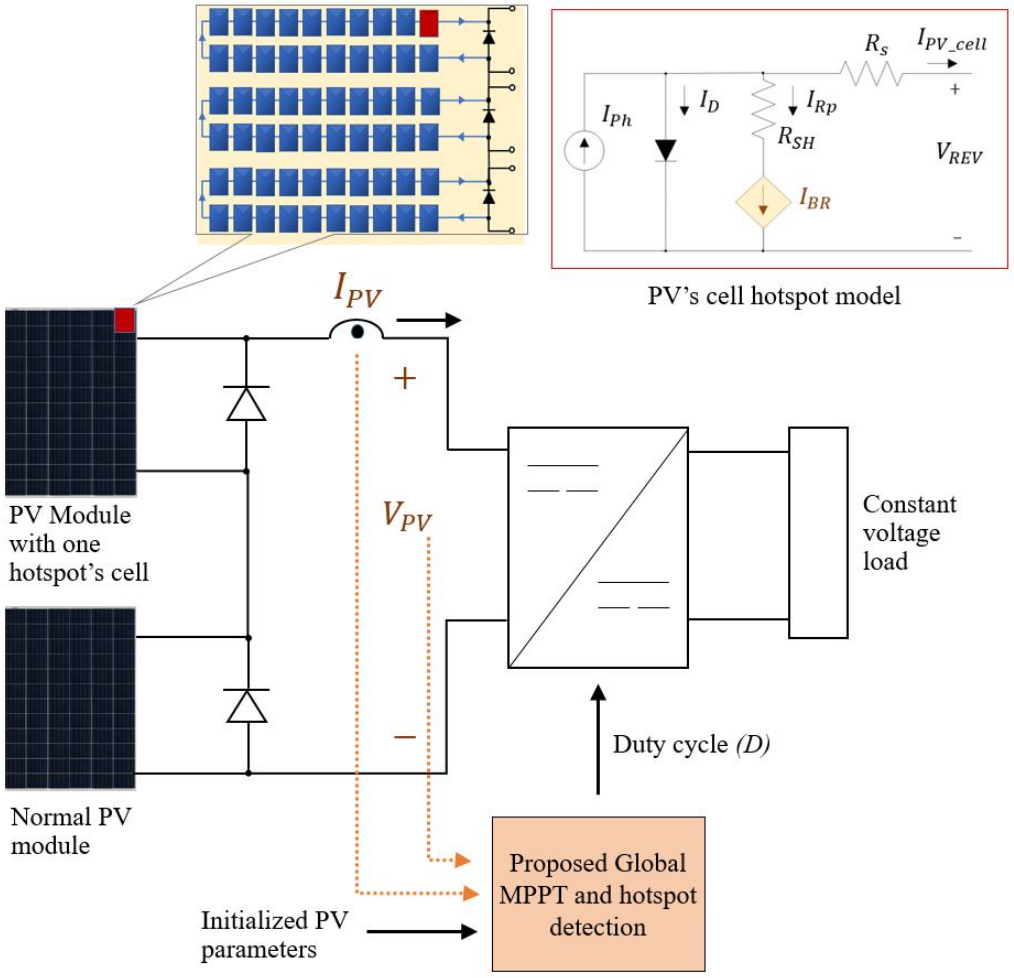

Figure 4.9: System's implementation of the hotspot detection for PV module in cluster's structure

For the converter unit, the sampling frequency and period are set in common to the simplified hotspot detection system presented in section 3.5 (sampling frequency is set as 10 kHz from the PWM signal, sampling time for the current and sensors is set as 0.1 ms.

Figure 4.10 shows the example of the I-V curve of hotspot conditions over the changes of reversed bias voltage.

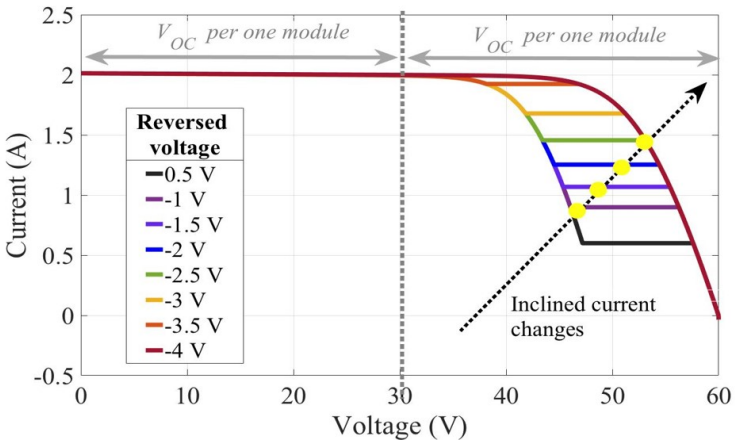

(a) I-V characteristic curves under hotspot condition with the decrease of reverse bias voltage over time

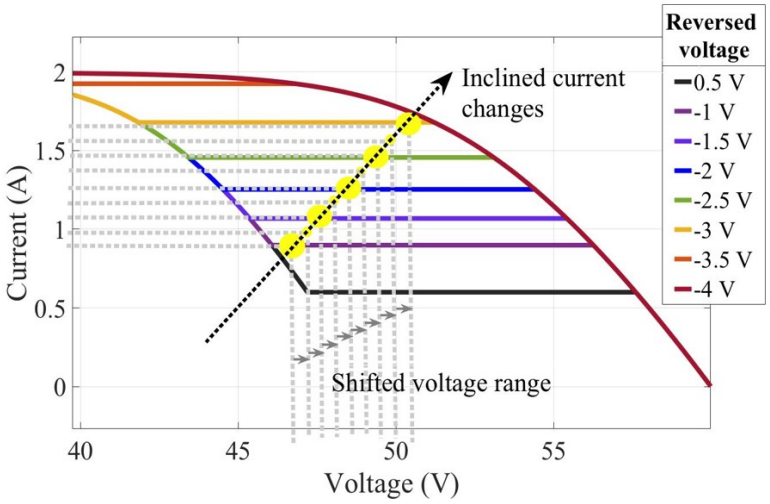

(b) Magnified inclined current changes detection area

Figure 4.10: PV module characteristic over operating time

As a result of the exponential increase of PV's current in the hotspot's cell, the decrease of reverse bias voltage tends to reach the breakdown. In addition, the slope calculation in the region can help to detect the dynamic change of hotspot. The information is used for designing the detection algorithm, in which the flowchart is shown in figure 4.11 (the algorithm is complemented together

with the shading detection and global MPP tracking in figure 3.7).

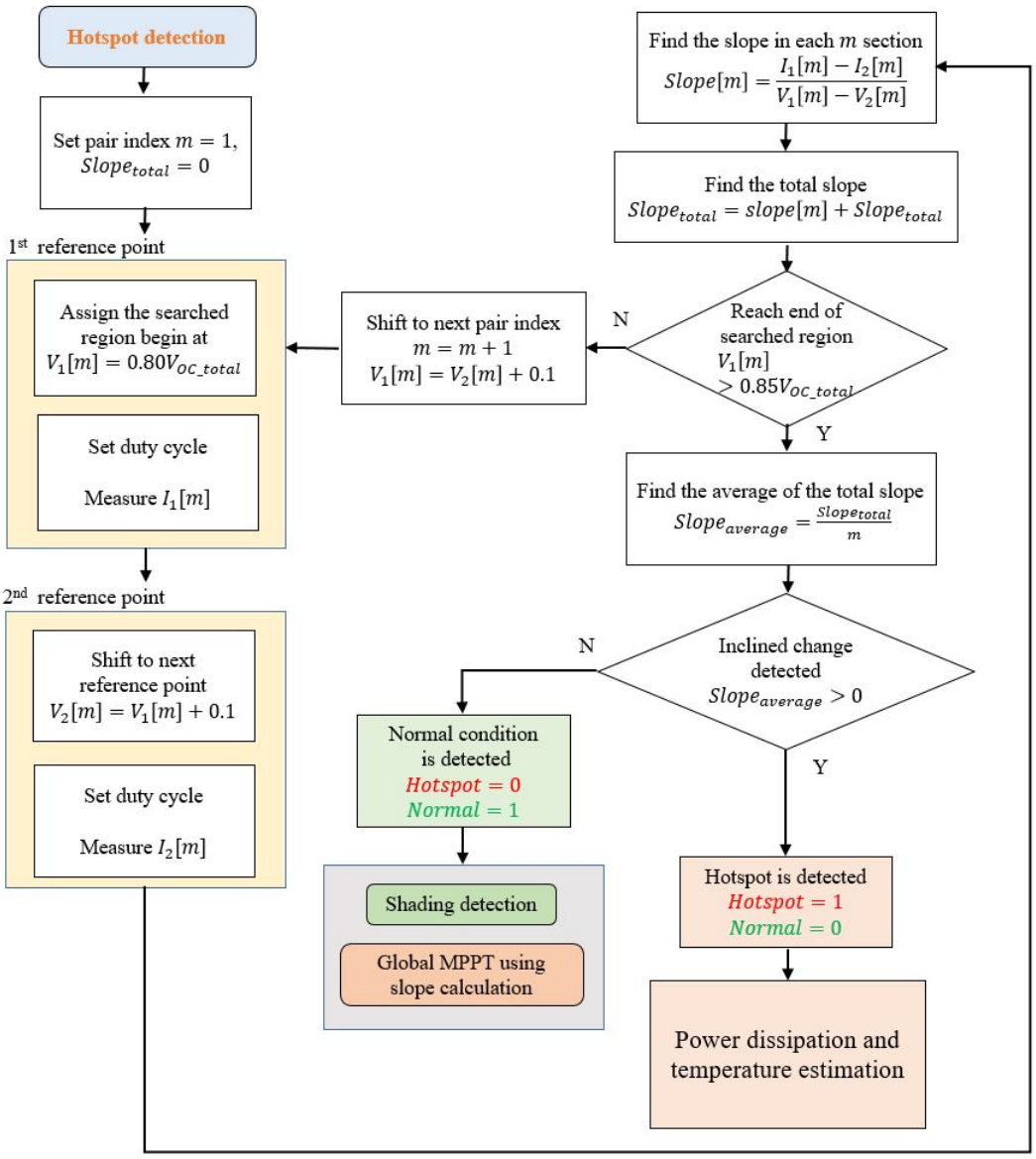

Figure 4.11: Proposed hotspot detection algorithm for PV module in cluster's structure

The concept of this algorithm is to improve the simplified detection model presented in section 3.8 to be compatible with the PV cluster structure. The al-

gorithm searches the detection every 1 hr after the power difference is detected. In the same manner as the simplified version, the indicators of PV's status ($Normal$ and $Hotspot$) are assigned.

For indicating the searched region, the hotspot occurrence probability is revised. According to the data survey of the PV sites across the UK [8], the most found hotspot type belongs to one hotspot's cell with 41% of the total hotspot's percentage, while the second rank belongs to two hotspot cells. From the I-V characteristic curves, the commonly searched region for all number of defected cluster locates at the ranges of the knee level of the curve (at 80% of V_{OC})

The algorithm starts detecting the inclined current from 80% of V_{OC}, the voltage assigns as the first reference voltage $V_1[1]$ and the current is recorded as $I_1[1]$. Step repeats after shifting the voltage by 0.1 V to the next point $V_2[1]$ at 85% of V_{OC}; afterward, the algorithm records the current $I_2[1]$. Consequently, the algorithm calculates the rate of change called $Slope[m]$ between two current points with respect to the voltage points, as shown in equation 3.1. After calculating all slope in the searched region, the average of the total slope ($|Slope_{average}|$) is determined. Importantly, to detect the hotspot, the algorithm calculates whether or not $|Slope_{average}|$ presents the reverse bias of the cell. If $|Slope_{average}|$ shows the positive value, the program estimates the status as the hotspot condition, making the $Hotspot$ indicator triggers from 0 to 1. Consequently, the algorithm proceeds to the second stage which is the power dissipation and temperature estimation On the other hand, for the normal condition if $|Slope_{average}|$ is less than or equal to zero, meaning the PV cell is not affected by the low shunt resistance, the $Normal$ status remains before proceeding to the global MPPT for tracking the maximum power.

To sum up, the proposed algorithm presents the hotspot detection method which can be used with the PV module in cluster's structure; improving more practical capability. By using the concept of detecting the increase of reverse bias current over the operating time, the program is capable to indicate the hotspot in the PV cell.

4.4 System Implementation and Results

This section presents the system's implementation to evaluate the proposed detection method. Using the module specification from table 4.1, the case divides by different values of the shunt resistances and irradiations. One-cell and two-cell hotspot are used to test the proposed detection algorithm, due to the high occurrence rate reviewed by the survey data explained in section 3.1. Figure 4.12 shows the system's implementation of the hotspot detection algorithm.

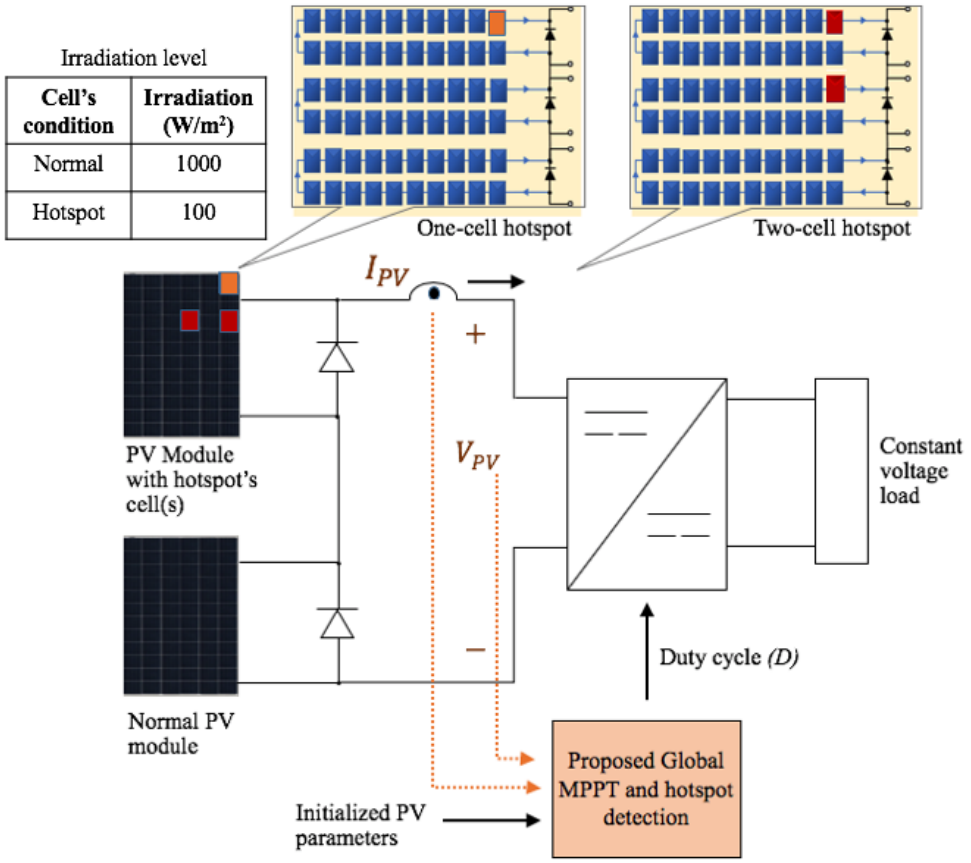

Figure 4.12: System's implementation of the hotspot detection in different cases

The hotspot model with VCCS and shunt resistance explained in figure 4.2 is used to build the hotspot PV cell. The implementation is divided with five possible values of shunt resistances with a -20% variation with respect to its nominal

value, based on [67]. The work considers five possible values of shunt resistance with the step of -20% reduced with respect to the nominal value at 35 Ohm, to present various defection levels. Furthermore, each resistance value is tested with different levels of irradiation.

4.4.1 One-cell Hotspot Detection

The first part of the implementation is to detect the one-cell hotspot in the PV array. Mentioned by the data survey in [8], the one-cell is the most-found hotspot type across the PV sites with the occurrence percentage of 42%, and yet the most challenging to detect. The test is divided by two irradiations at 10 W/m^2 and 100 W/m^2. The hotspot's cell is highlighted in red in figure 4.12.

(a) Irradiation at 10 W/m^2

The first case presents the detection at 10 W/m^2. Figure 4.13 presents the results of hotspot detection with different shunt resistances, including normal conditions.

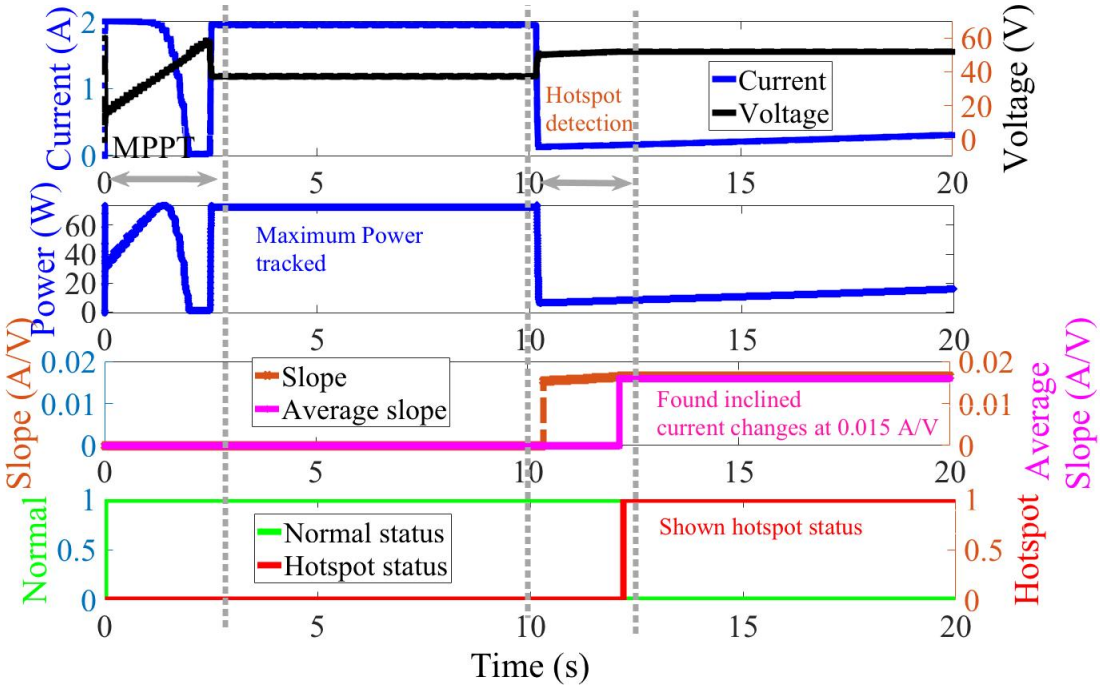

(a) 35 Ohm

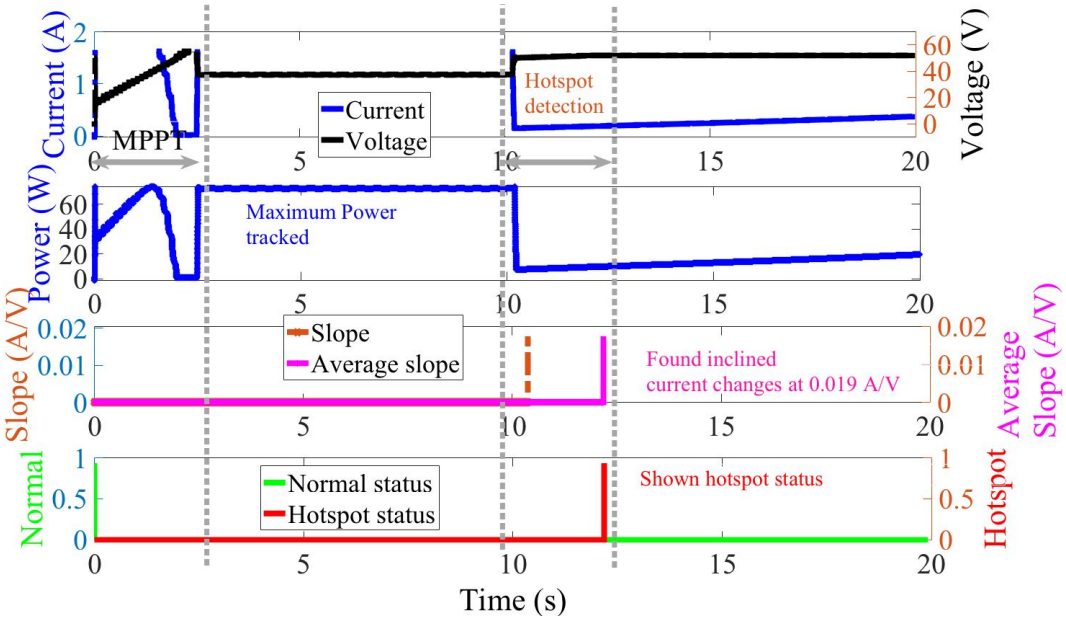

(b) 28 Ohm

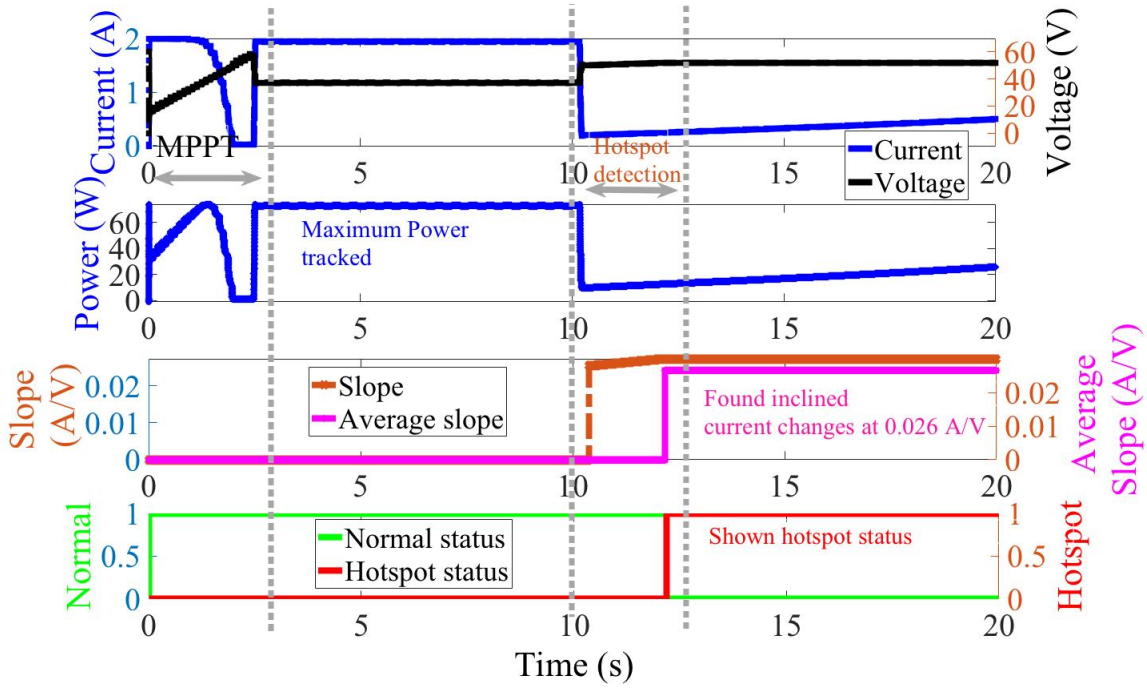

(c) 21 Ohm

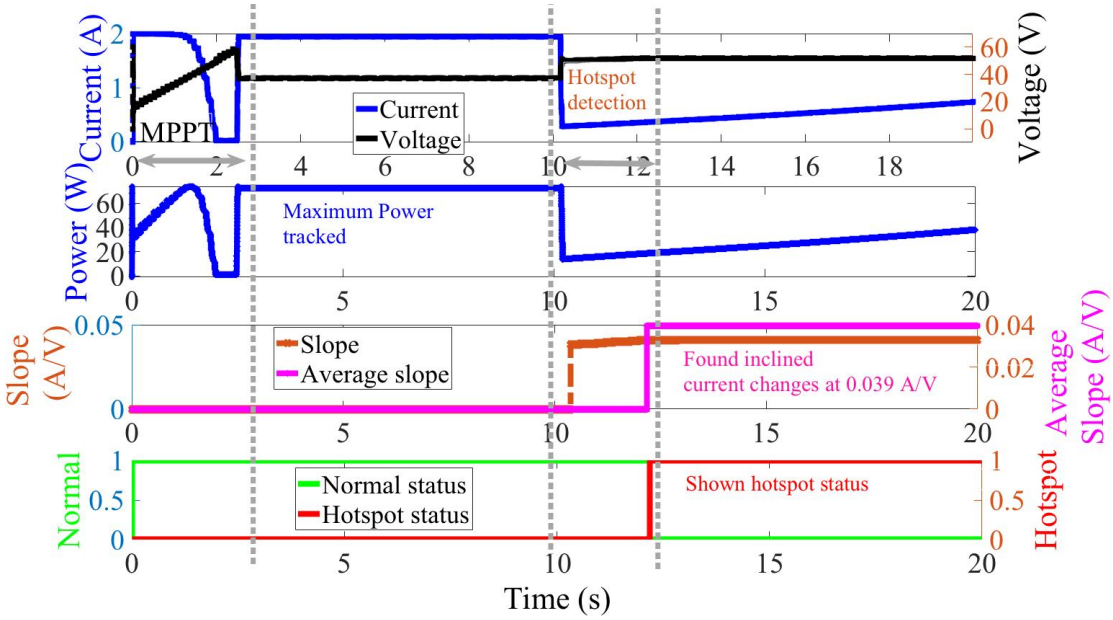

(d) 14 Ohm

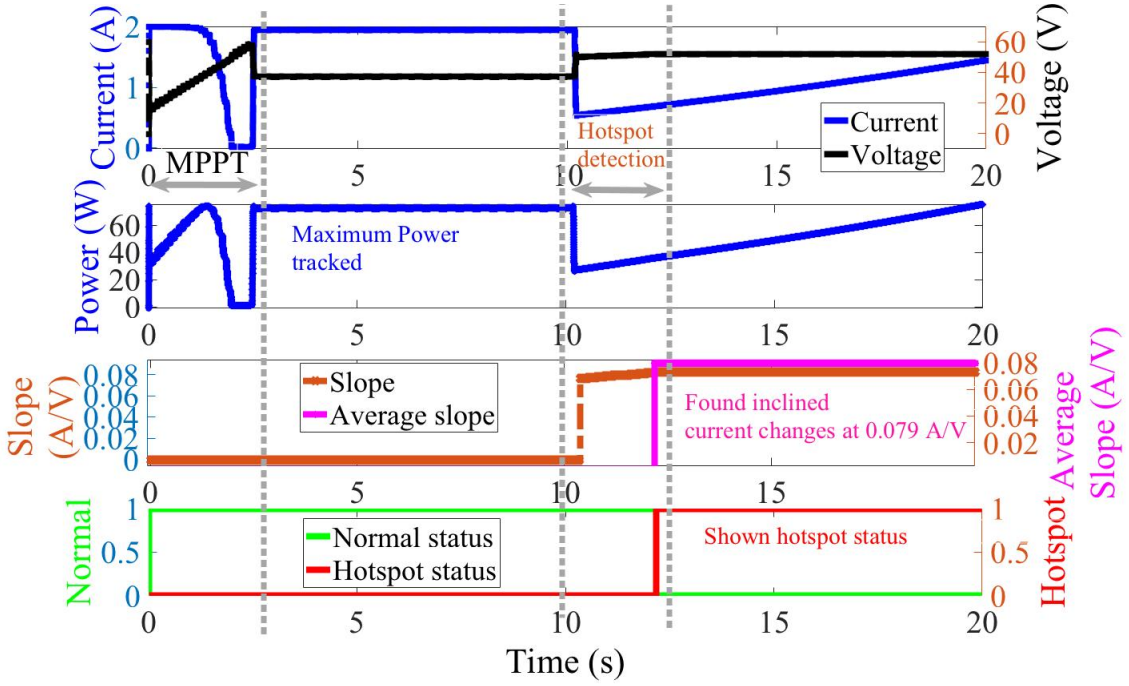

(e) 7 Ohm

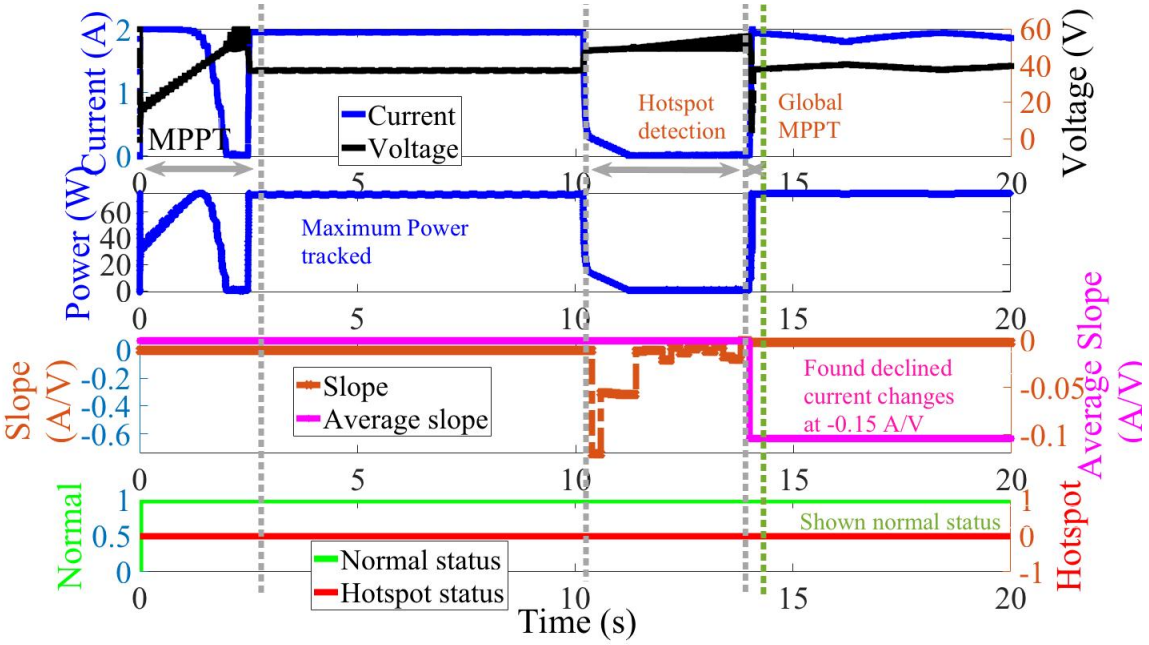

(f) Shading condition

Figure 4.13: Hotspot and normal condition detection for the irradiation at 10 W/m^2 at different shunt resistances

The results in figure 4.13 confirms the efficiency of the proposed hotspot detection algorithm. The program starts with the first MPPT to determine the maximum power of the total PV array, detecting at 72.74 W. The process takes approximately 2.5 seconds. Continuously, when the hotspot occurs at 10 seconds, the program starts to identify the hotspot by calculating $Slope[m]$ and detecting any incline of the current from the reverse bias current. According to figure 4.13, the hotspot at different shunt resistances is detected. It can be observed the increase of incline current changes when shunt resistances reduce after the program successfully detects the hotspot. Although the resistances vary the changes of PV cell current; the algorithm is capable to detect the incline change. The status indicator triggers from 0 to 1 for indication, after the algorithm finishes the detection. This process takes approximately 2.23 seconds.

On the other hand, the algorithm can determine the normal condition, including the low irradiation at 10 W/m^2. The program determines the status as the

normal condition in which proceeds to the proposed global MPPT in chapter 2. From figure 4.13(f), the program detects the normal condition with the decline slope at -0.15 A/V. Consequently, the program proceeds to the global MPPT algorithm after completing the detection. The algorithm takes approximately 0.23 seconds to track the new global MPP.

(b) Irradiation at 100 W/m²

Apart from the low irradiation, figure 4.14 shows the hotspot detection at 100 W/m^2 to evaluate the proposed algorithm in different irradiation condition.

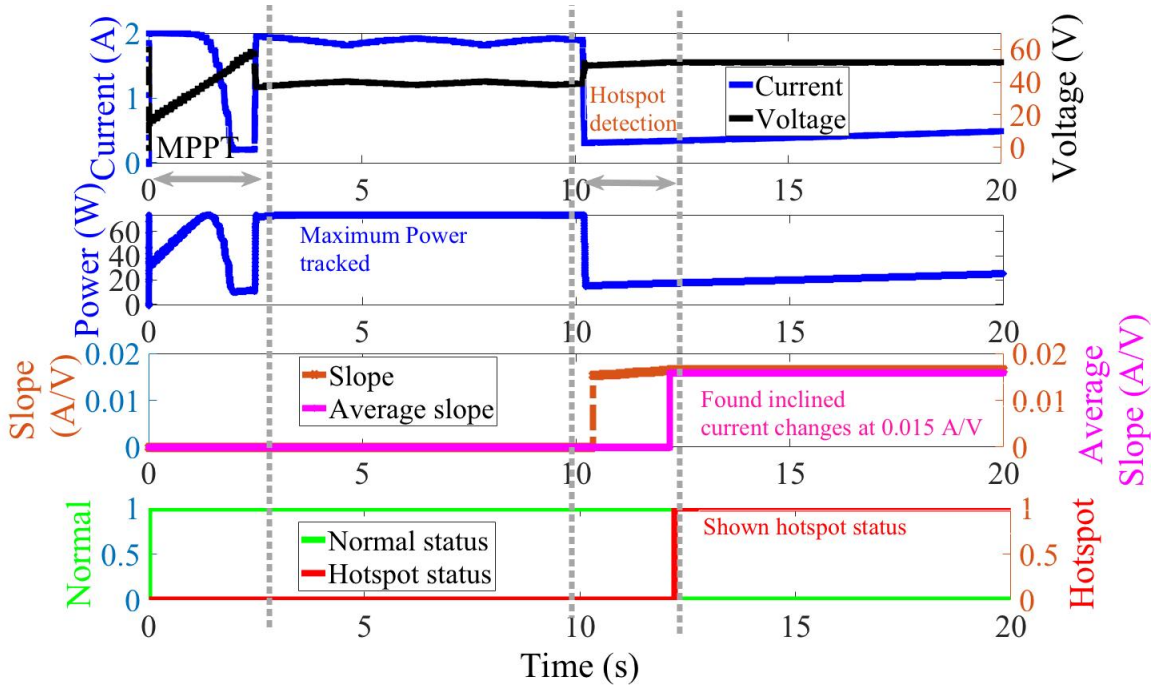

(a) 35 Ohm

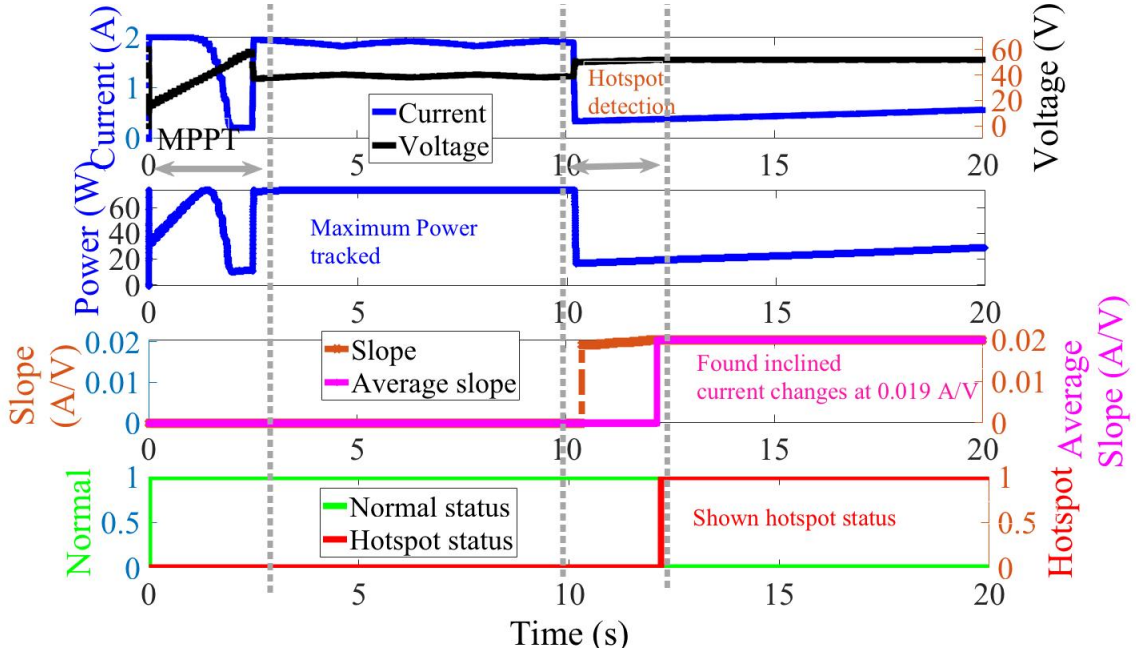

(b) 28 Ohm

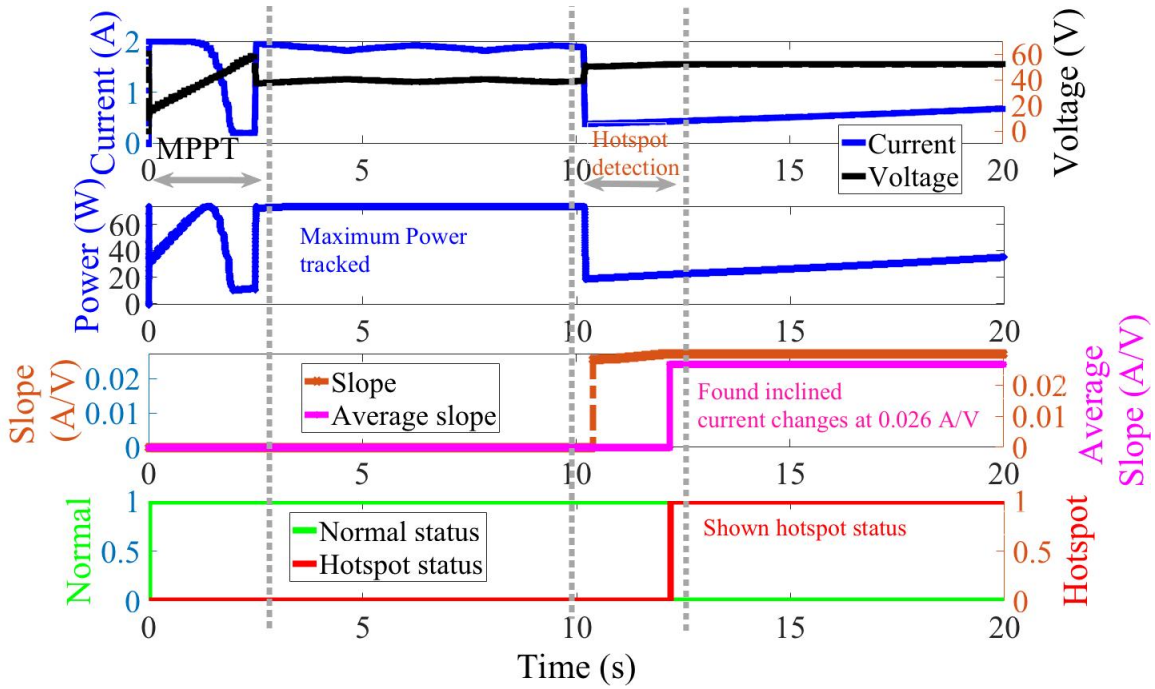

(c) 21 Ohm

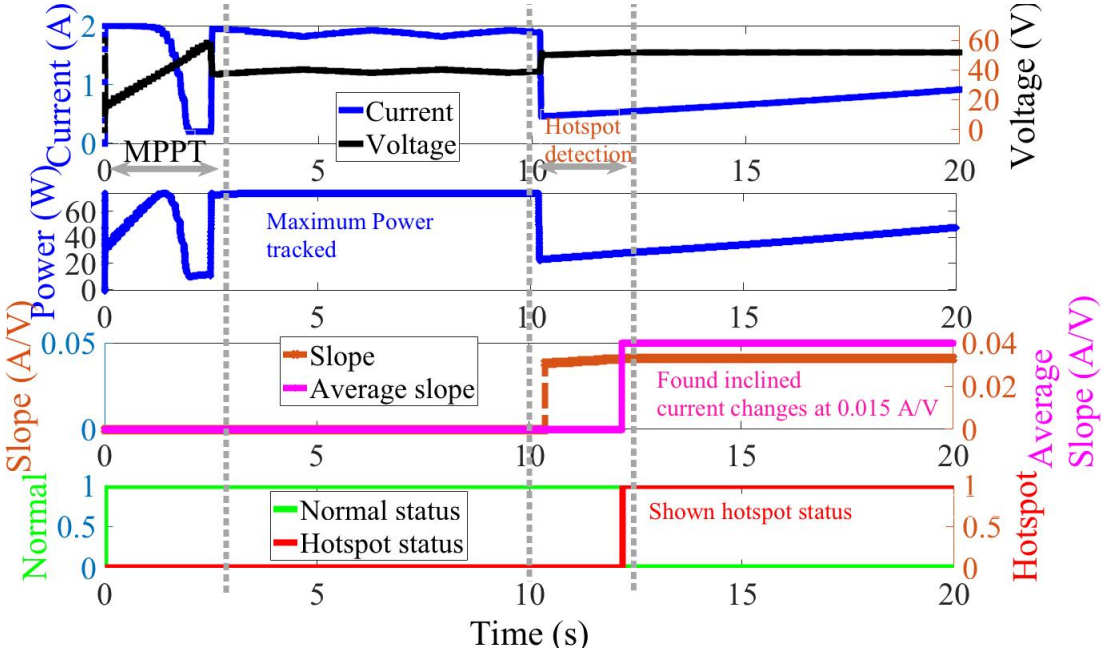

(d) 14 Ohm

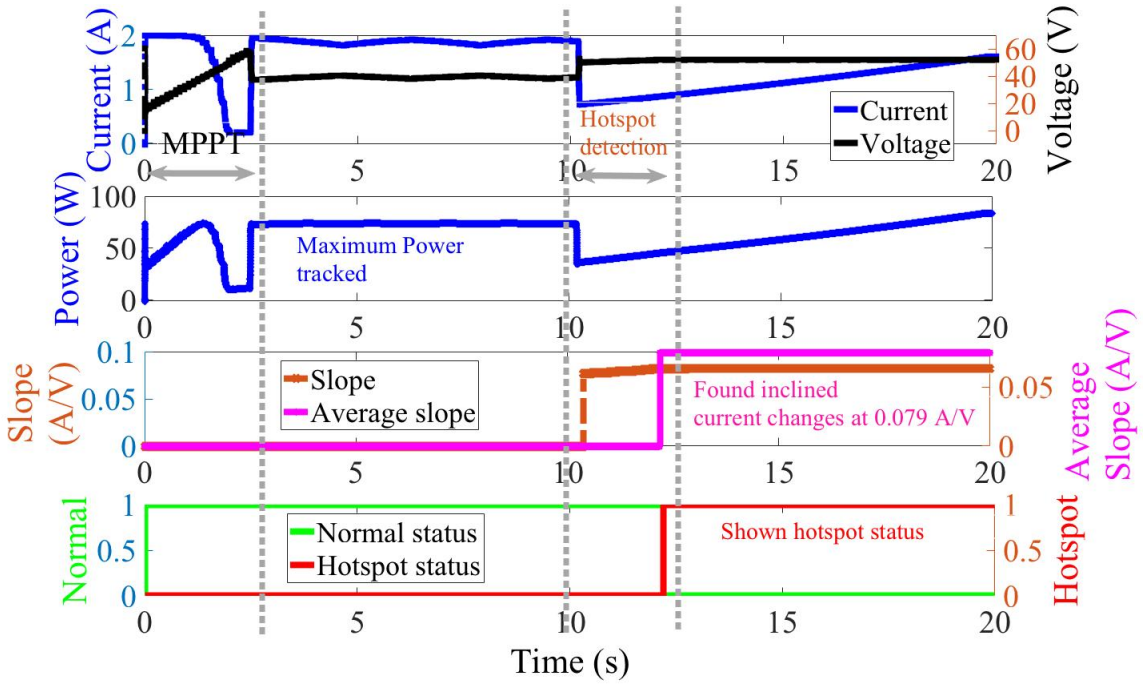

(e) 7 Ohm

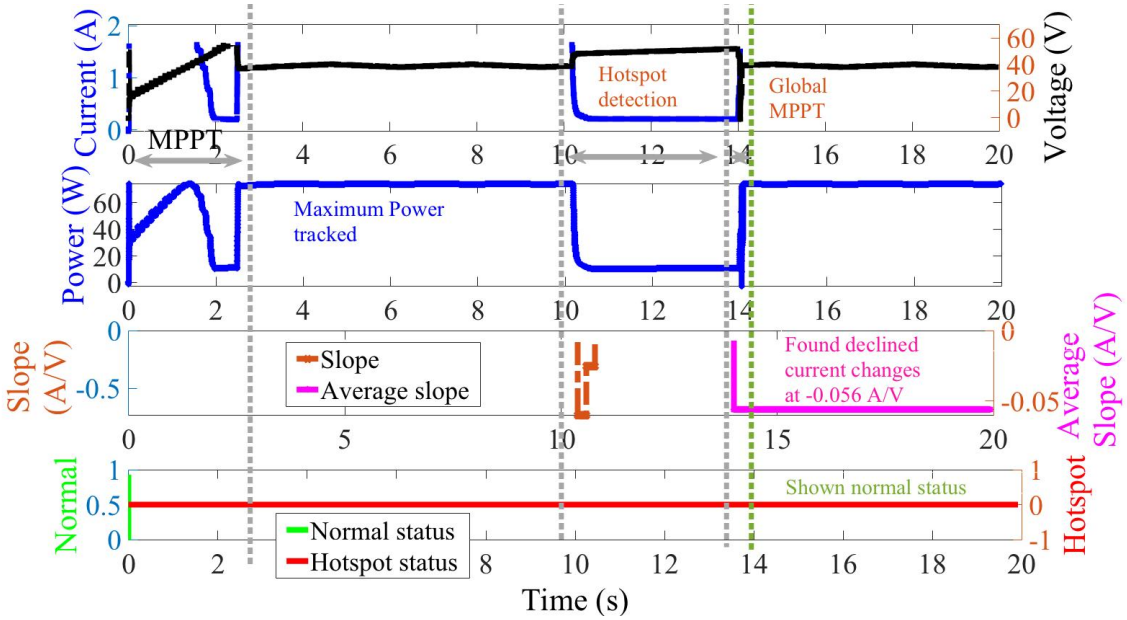

(f) Shading condition

Figure 4.14: Hotspot and normal condition detection for the irradiation at 100 W/m^2 at different shunt resistances

Graphical results in figure 4.14 also confirm the success of the proposed hotspot detection algorithm. The program starts with the first MPPT to determine the maximum power of the whole PV array. Afterward, when the hotspot occurs at 10 seconds, the program starts to identify the hotspot by calculating $Slope[m]$ and detect any incline of the reverse bias current. The results of the hotspot detection show successful detection, which indicate the increase of incline current changes when the shunt resistances decrease. The algorithm is capable to detect the incline change although the resistances vary the inclined current changes rate.

Moreover, the algorithm can also determine the normal condition including the shading irradiation at 100 W/m^2. The program determines the status as the normal condition and proceeds to the global MPPT to track the new MPP. Confirming by figure 4.14(f), the program detects the normal condition with the decline slope at -0.056 A/V, proceeding to the global MPPT after the detection

completes. The algorithm takes approximately 0.27 seconds to track the new MPP.

4.4.2 Two-cell Hotspot Detection

In this part, the test involves the number of hotspots cells in the PV module. The test uses the implementation according to figure 4.12 (whereas the hotspot's cell is highlighted in orange). The test consists of three categories, categorized by different shunt resistances and irradiation. Table 4.2 summarizes the information of three test categories, dividing into cases 1 to 8.

Table 4.2: Summarized information of the two-cell hotspot detection cases from 1 to 8

Case catagory	**Case number**	**First hotspot's cell**		**Second hotspot's cell**	
		Irradiation (W/m^2)	Shunt resistance (Ohm)	Irradiation (W/m^2)	Shunt resistance (Ohm)
Same irradiation with different shunt resistance	1	100	35	100	35
	2	100	35	100	21
	3	100	21	100	7
Different irradiation with same shunt resistance	4	100	28	300	28
	5	100	14	300	14
Different irradiation with different shunt resistance	6	200	21	500	14
	7	10	14	400	7

Category 1: Same irradiation with different shunt resistance

Figure 4.15 presents the graphical results of two-cell hotspot detection for the first category, dividing into cases 1 to 3. The hotspot is set to happen at 10 seconds based on the simulation time.

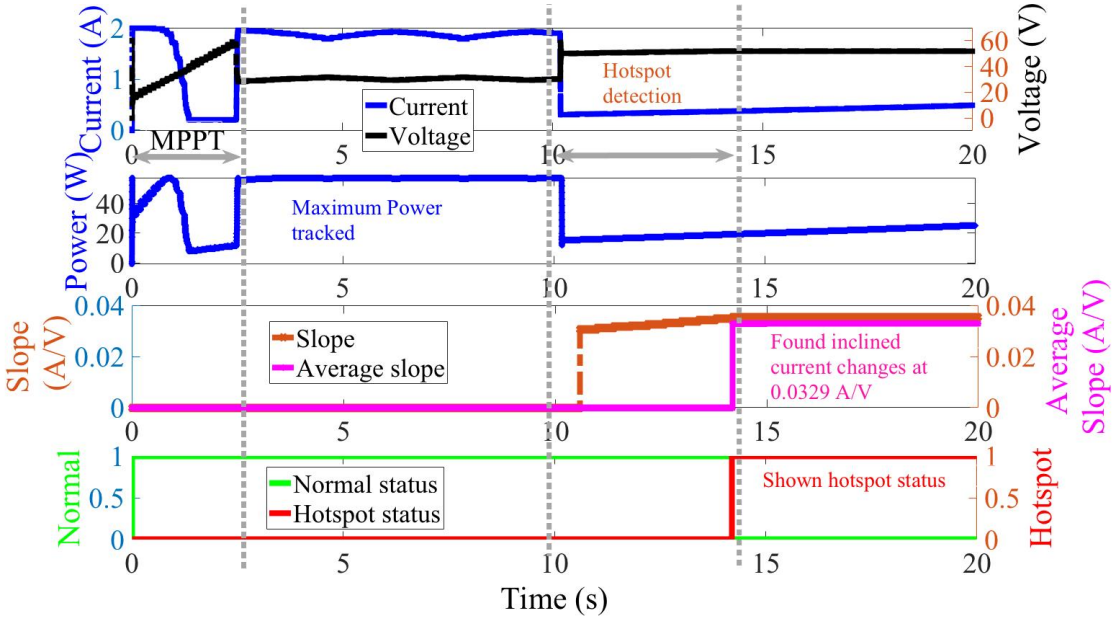

(a) Case 1

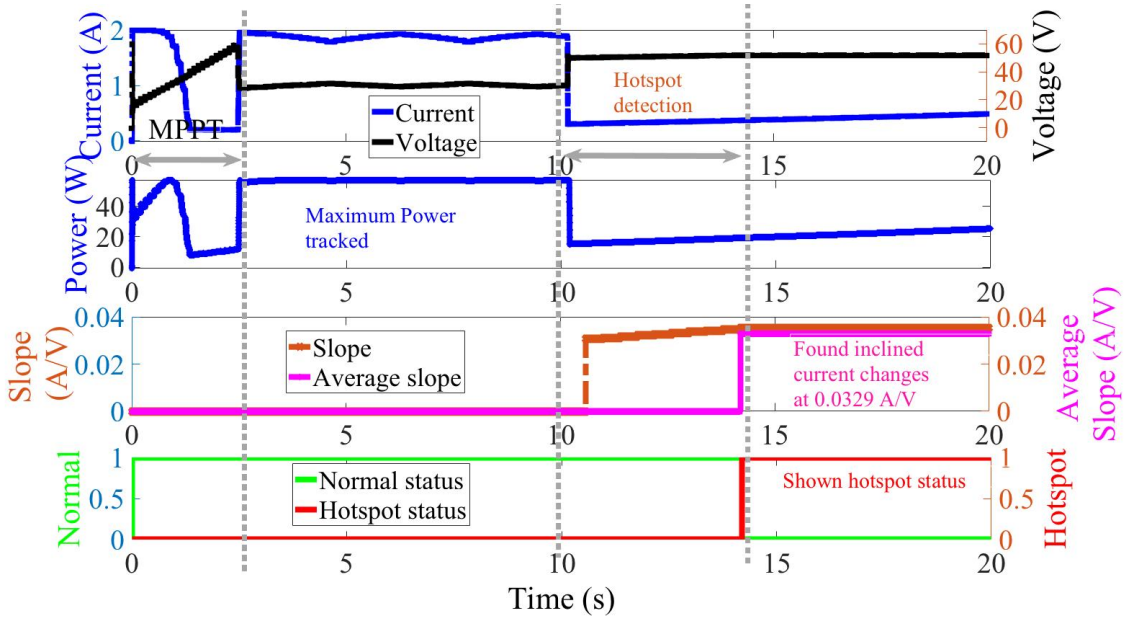

(b) Case 2

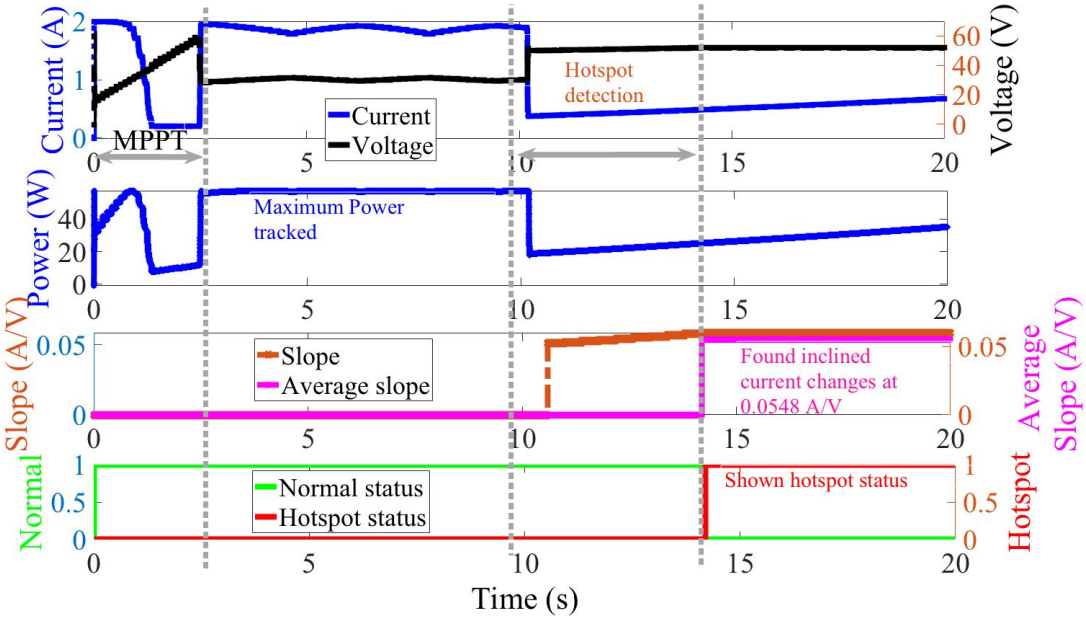

(c) Case 3

Figure 4.15: Graphical results of two-cell hotspot detection (category 1)

According to the results in figure 4.15, it is established the success of the proposed detection algorithm when the shunt resistance is varied. As shown in figures 4.15(a) and 4.15(b), the average slope of 0.0329 A/V is achieved. Both cases present the same slope value due to the same highest shunt resistance value at 35 Ohm. By tracking the slope starts from 80% of the total open-circuit voltage, the slope of the highest shunt resistance is estimated. The algorithm tracks the hotspot and shows the indicator within 5 seconds. Similarly, for figure 4.15(c), the average slope is tracked with a value of 0.0548 A/V. The value is determined from the highest shunt resistance of 21 Ohm, giving the higher slope value compared to cases 1 and 2.

Category 2: Different irradiation with same shunt resistance

Figure 4.16 shows the graphical results of two-cell hotspot detection for the second category, from cases 4 and 5.

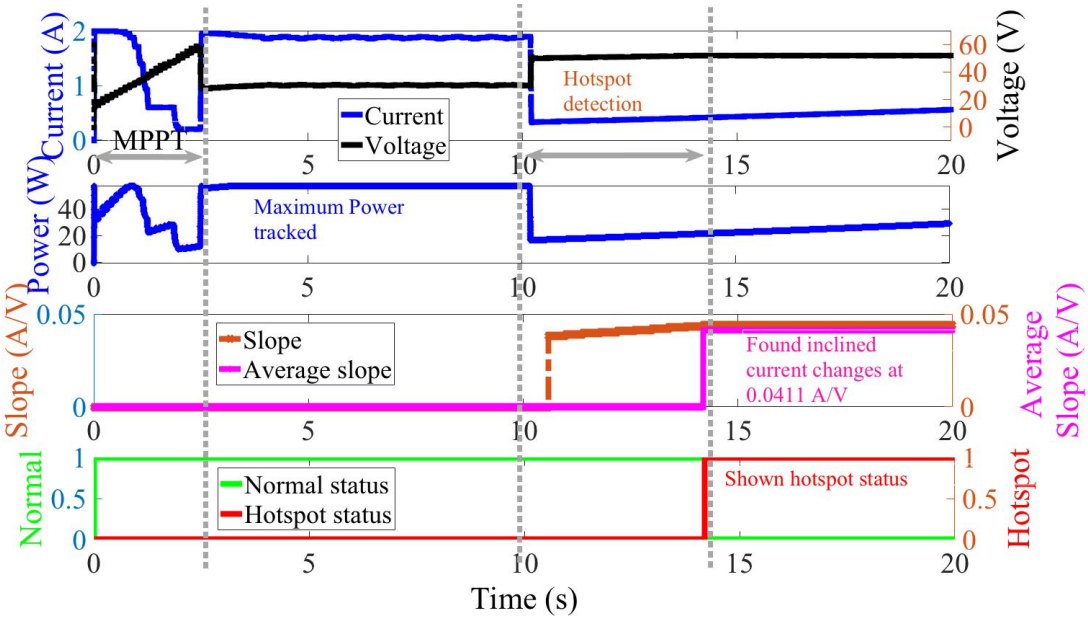

(a) Case 4

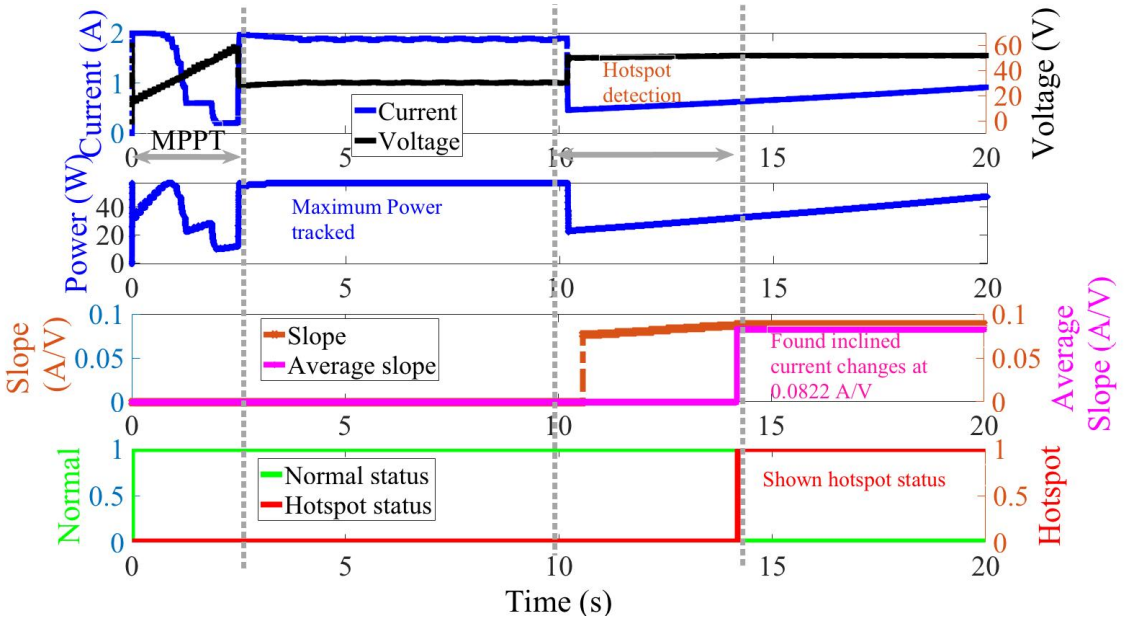

(b) Case 5

Figure 4.16: Graphical results of two-cell hotspot detection (category 2)

From the graphical results, the proposed algorithm succeeds to determine the hotspot at different irradiation levels. Confirming in figure 4.16(a), at the MPPT period between 0 to 3 seconds, the graph shows the effects of non-uniform irradiation by representing with the step change of the PV's current. Although the shading only applies to the two cells (from a total of 60 in three clusters), the non-uniform current still can be observed. Apparently, the total maximum power after MPPT is 56.5 W due to shading conditions. After the hotspot occurs at 10 seconds, the algorithm starts the detection process, results in the average slope of 0.0411 A/V. The value is occurred by the lowest irradiation level of 100 W/m^2, with the highest shunt resistance of 28 Ohm. Furthermore, figure 4.16(b) presents the success detection with the average slope of 0.0822 A/V (higher than case 4), results from the highest shunt resistance of 14 Ohm. The detection in both cases also takes less than 5 seconds. In comparison, although the same irradiation levels are established in cases 4 and 5, the average slopes are varied due to the difference of shunt resistances.

Category 3: Different irradiation with different shunt resistance

Figure 4.17 shows the results of the third category, consists of cases 6 and 7.

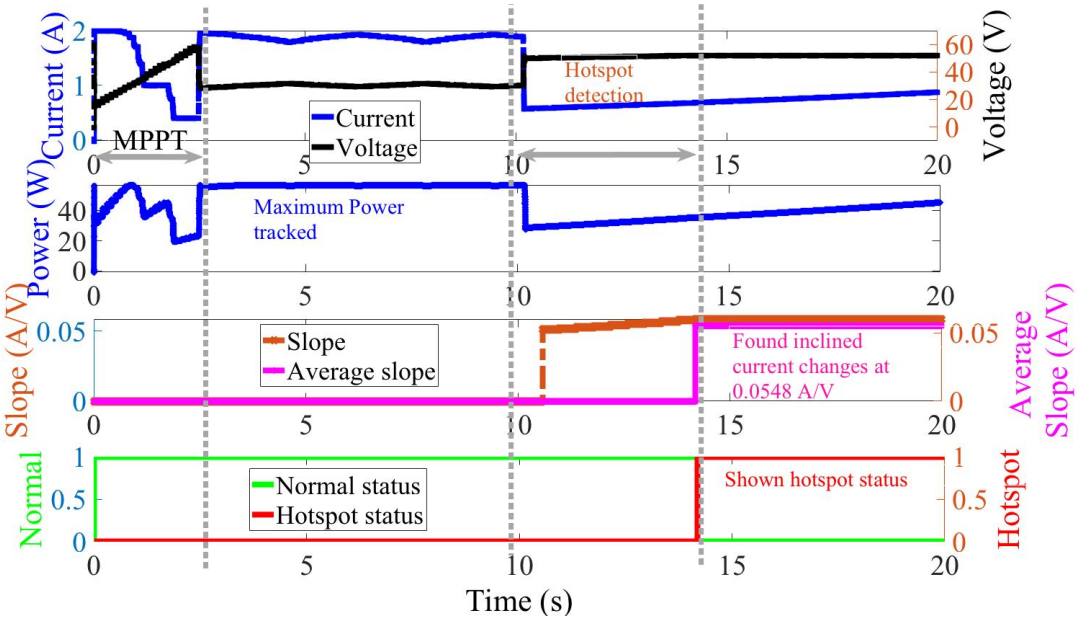

(a) Case 6

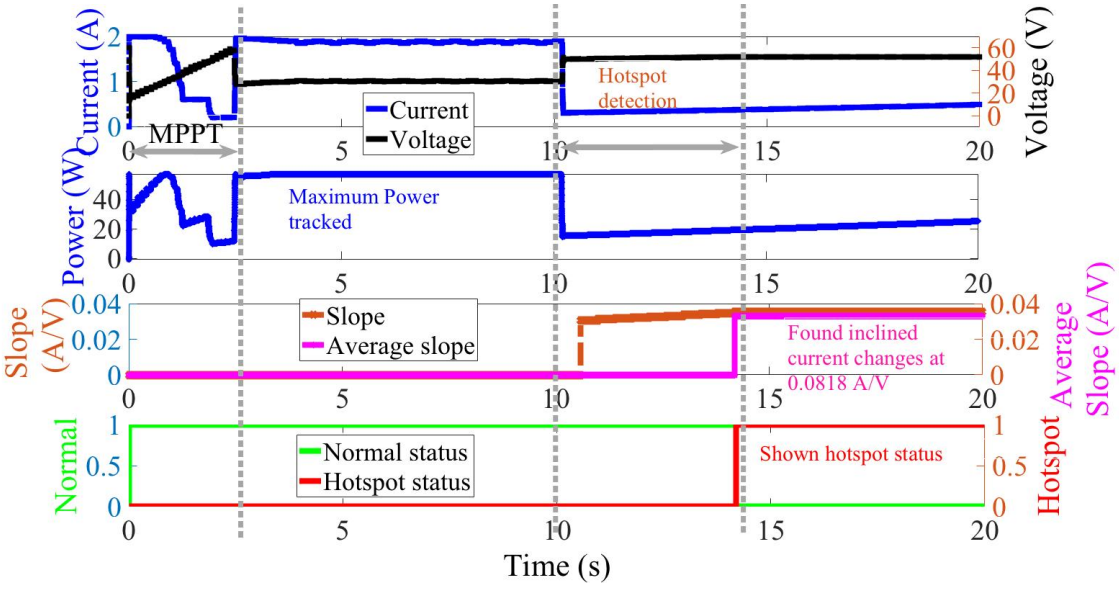

(b) Case 7

Figure 4.17: Graphical results of two-cell hotspot detection (category 3)

According to results in figure 4.17, the proposed algorithm can detect the hotspot in the last two cases which the irradiation and shunt resistance are non-uniform. Between the MPPT, the graph shows the effects of non-uniform irradiation by representing the step change of the PV's current. The MPPT completes the power track, reaching the maximum power of 57.2 W. Observed in figure 4.17(a), the algorithm detects the hotspot at the average slope of 0.0548 A/V, which generated from the highest shunt resistance of 21 Ohm at the first hotspot's cell. Furthermore, figure 4.17(b) shows the success detection with an average slope of 0.0318 A/V, results from the highest shunt resistance of 14 Ohm.

To conclude the two-cell hotspot detection results, even though the shunt resistance and irradiation do not significantly reduce the maximum power of the total PV array, it is important to detect the hotspot, especially at the low shunt resistance. The results from cases 1 to 7 confirm the efficiency of the proposed hotspot detection algorithm. The focused parameters in the results include the accuracy of the detection, average slope and detection time. Furthermore, the results of hotspot detection develops the robust responses. Results show the de-

tection time for two PV's series-connected panels takes within 5 seconds, imply fast detection. The sudden current and voltage changes can be occured during the detection; however, the duration is considered to be short within 2 seconds after the detection completes. Moreover, for the normal condition, the system can recover back to the stability point by using the proposed global MPPT algorithm, with the maximum time required of 4 seconds. The algorithm can operate under various conditions of irradiation and shunt resistance. Importantly, the system implementation is simple and requires neither the extra current and voltage sensors, temperature and irradiation sensors, nor the infrared camera.

4.4.3 Detection with Different Breakdown Voltage Rate

To confirm the slope detection concept to detect the hotspot, figure 4.18 summarizes the average slope results over the decrease of shunt resistances in different degradation rates. The results consist of five different time ranges for the PV cell to reach its breakdown voltage; including 50, 100, 150, 200 and 250 seconds.

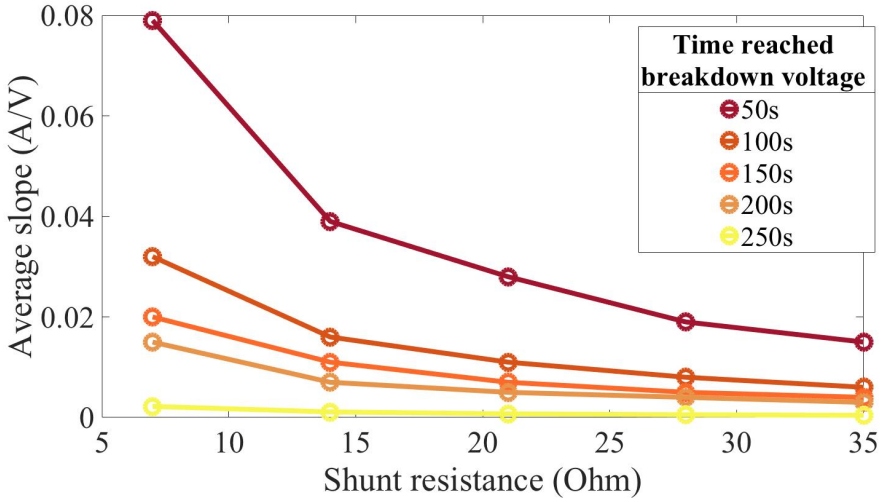

Figure 4.18: Record of the average slopes at different shunt resistances and rate of reverse bias voltage changes

Table 4.3 summarizes the numerical results of the average slope according to figure 4.18.

Table 4.3: Numerical results of the average slopes at different shunt resistances and rate of reverse bias voltage changes

Time reached	$\lvert Slope_{average} \rvert$				
breakdown voltage (s)	35 Ohm	28 Ohm	21 Ohm	14 Ohm	7 Ohm
50	0.015	0.019	0.028	0.039	0.079
100	0.006	0.008	0.011	0.016	0.032
150	0.004	0.005	0.007	0.011	0.020
200	0.003	0.004	0.005	0007	0.015
250	4.312e-4	5.3906e-4	7.1876e-4	0.0011e-4	0.0022e-4

Results from figure 4.18 show that the average slope increases in inversely proportional to the time reached the breakdown voltage, with the decrease of the shunt resistance. The maximum average slope reaches 0.08 A/V at 7 Ohm for 50 seconds of time to reach breakdown voltage. In summary, due to the low shunt resistance as long as the defective cell works in reverse bias operation, the cell experiences more power dissipation and leads to higher temperature rises.

Further discussions of the power dissipation and temperature estimation to indicate the level of damage of the PV cell is presented in the next section.

4.5 Temperature Estimation

As explained in section 4.2 about the effect of shunt resistance and irradiation which distributes to power dissipation in the PV cell. In this section, the power dissipation and temperature estimation are discussed.

Described by IEC 61215 in figure 3.3, the reversed bias I-V curve can represent the quantity of power dissipation by calculating the area under the curve in the reversed bias region. Since the power dissipation and the temperature have a directly proportional relationship, it is possible to use the information to estimate

the temperature. However, the difficulty is to connect these two parameters together, because the power dissipation is representing using the electrical term meanwhile thermal is one of the material properties. The objective is to find the linkage parameter to connect the dissipation and temperature.

Research by Armstrong et al [80] explains the material composition of the PV panel. The information states the six main material layers in the panel; the glass covering, an anti-reflective coating (ARC), PV cells, ethylene-vinyl acetate (EVA), metal back sheet and Tedlar PVF layer, these layers get embedded in a metal frame. Furthermore, the thermal transfer can be derived by the RC thermal circuit, which consists of the thermal resistances and capacitances. Figure 4.19 shows the thermal model of the layers in the PV panel.

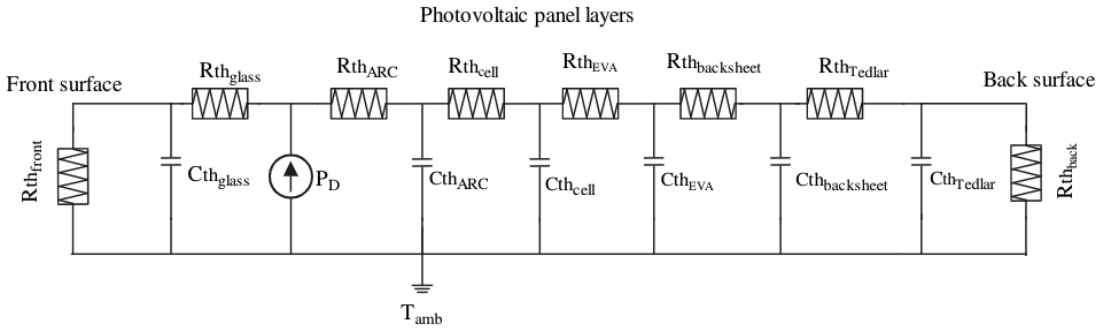

Figure 4.19: Photovoltaic thermal resistance network [80]

The thermal model in figure 4.19 describes the heat loss in each layer representing by the thermal resistances and capacitances. Each component can be evaluated using the functions of the material's sizing and thermal properties.

Research by Rossi et al [67] describes the occurrence of the hotspot as the small area in the cell and proposes the thermal model to represent the hotspot parameters. Figure 4.20 shows the equivalent thermal model use to estimate the temperature of the defected area under hotspot conditions.

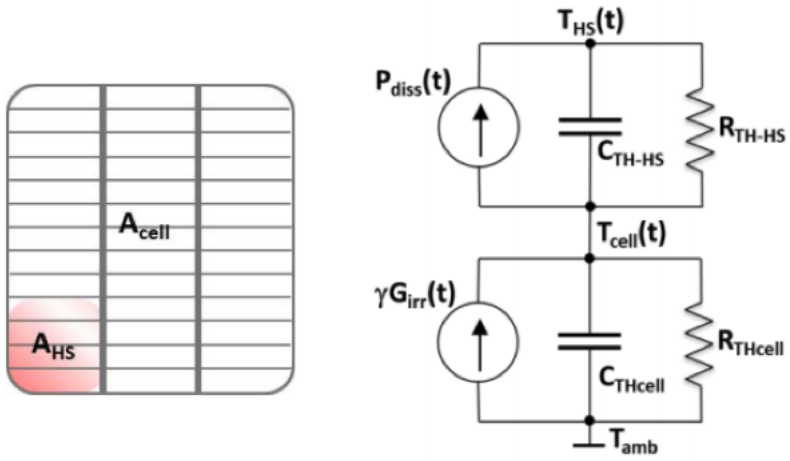

Figure 4.20: Equivalent thermal model to estimate the temperature of the defected area under hotspot condition [67]

From figure 4.20, The lower RC circuit consists of C_{THcell} and R_{THcell}, represents the PV cell temperature as a function of the cell's irradiation $\gamma G_{irr}(t)$. Moreover, the upper RC circuit composed by C_{TH-HS} and R_{TH-HS} models the represent of temperature in terms of power dissipation function $P_{diss}(t)$. The power dissipation can be estimated from the area under the I-V curve in reversed bias condition.

The value of parameters R_{THcell}, C_{THcell}, R_{TH-HS} and C_{TH-HS} depends on the material composing the upper layer of the PV cell. Equations 4.3, 4.4, 4.5 and 4.6 show the calculation of RC thermal properties used in the model. The equations also present that the property's value is related to the sizing of PV cell (including material's thickness and hotspot area), and the material properties (such as material's thermal conductivity, density, and heat capacity).

$$R_{THcell} = \frac{l}{kA_{cell}} \tag{4.3}$$

$$R_{TH-HS} = \frac{l}{kA_{HS}} \tag{4.4}$$

$$C_{THcell} = A_{cell} l \rho \varsigma \tag{4.5}$$

$$C_{TH-HS} = A_{HS} l \rho \varsigma \tag{4.6}$$

After calculating the RC thermal circuit parameters, equation 4.7 is used to estimate the temperature before and after the occurrence of the hotspot.

$$T_{HS}(t) = \begin{cases} T_{amb} + R_{THcell} G_{irr} & , t < t_{HS} \\ T_{amb} + R_{THcell} G_{irr} (\gamma + (1-\gamma) e^{-(\frac{t-t_{HS}}{R_{THcell} C_{THcell}})}) & \\ + P_{diss} R_{TH-HS} (1 - e^{-(\frac{t-t_{HS}}{R_{TH-HS} C_{TH-HS}})}) & , t \geq t_{HS} \end{cases} \tag{4.7}$$

From equation 4.7 assuming before the hotspot occurrence ($t < t_{HS}$), temperature estimation can be calculated according to the function of ambient temperature T_{amb}, thermal resistance of the defected area R_{THcell} and cell's irradiation G_{irr}. In simplicity, the temperature level mainly depends on the ambient temperature during operation. However, after the hotspot occurs ($t \geq t_{HS}$), there are several parameters involved in the temperature. The parameters can be explained as the exponential terms of the thermal RC circuits response. Also, the equation shows the proportional relationship to the temperature with the levels of irradiation and importantly, the power dissipation P_{diss} related to the shunt resistances value as explained.

After the estimation, the important point is to identify the degradation level regarding the hotspot's temperature. As reviewed, the temperature's damage threshold is introduced by the operating standard in each country and publications. Each work presents differently based on the temperature's level. For instance, research in [81] describes the indicator using the thermal breakdown in a cell's p-n junction. The high internal temperatures can reach above 400 °C, entering the cell's second breakdown voltage. Consequently, the breakdown leads to permanent cell damage. However, even if the second breakdown does not occur, high cell temperatures can lead to secondary degradation effects. Figure 4.21 presents the temperature's threshold for each degradation level.

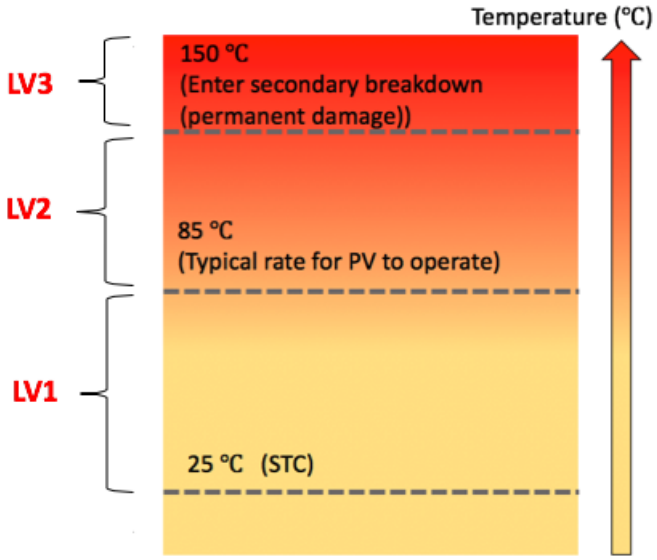

Figure 4.21: PV cell damage threshold identified by the estimated temperature [81]

Typically, PV panels are rated up to 85 °C, but hotspot can push the cell temperature far above the rated temperature. If the cell surface temperatures surpass 150 °C, the encapsulate and isolative material surrounding the cells can be damaged.

The major challenging points are mainly the determination of power dissipation, which needs more elaborate current and voltage sensors installation. Also, the calculation involves the PV cell material properties; in which the deep knowledge of material science is necessary. In this case, it has a high potential for further researches to develop the hotspot temperature estimation using the collaboration between electrical engineering and material science fields.

4.6 Conclusions

In conclusion, this chapter presents the improved hotspot model, which is derived from the elaborate analysis of the reversed bias effect in the PV cell scale as stated in the IEC 61215 standard. The new hotspot model develops from the voltage-controlled current source with the usage of the shunt resistance.

This chapter analyzes the effects of hotspot from the factors, including the shunt resistance, level of irradiation and total performance in the cluster's structure PV module. The analysis shows more development and compatibility of the hotspot's model, contributing to a more practical level with the PV's standard.

Importantly, the new hotspot detection algorithm is implemented to detect the hotspot in the cell's scale, using the concept of the increased bias current under reversed bias condition to detect the incline change of PV's current overtime (represent with the current's average slope). This concept is new and has never been introduced in other research works. The implementation and graphical results prove the efficiency and accuracy of the detection in different irradiation and shunt resistances. The algorithm shows fast detection within 5 seconds, representing the inclined average slope. Finally, the temperature estimation method is discussed using the RC thermal circuit. The main challenges are the determination of power dissipation, which requires more elaborate sensors installation and the material property parameters. Future works from this chapter are to analyze the PV material characteristic under hotspot conditions such as thermal distributions and heat transfer on each PV material structure.

Chapter 5

Conclusions and Future Works

5.1 Conclusions

This thesis emphasizes two main points, including (1) global MPPT under partial shading condition and (2) hotspot detection in the PV system. To elaborately answer the problem of determining the accurate MPP during partial shading conditions, the new global MPPT algorithm can effectively track the maximum power with the changes of irradiation and temperature. The proposed algorithm is implemented based on the concept of the slope calculation technique. Three parts of the algorithm include the main program, shading detection and irradiation estimation, and global MPPT. Moreover, studies using short-term and long-term operations prove the effectiveness of the algorithm. The algorithm contributes to the fast-tracking speed, sequences to lower the power loss, with more power generated.

As a consequence of partial shading in PV system, the problem of the hotspot is continuously analyzed. This thesis describes the effects of the hotspot, which not only decreasing the power but also causes damage to PV module. The main challenging point is the connection between electrical and material engineering perspective to implement the hotspot model.To answer the question, the hotspot model using a low shunt resistance model to express the degradation of the PV

performance. The model is analyzed and continuously improved by considering reversed bias condition and practical standard. By using the information achieves from the characteristic curves, the detection method using the inclined current change is presented. Since the degradation of the material is observed, more increase in current in hotspot's cell is shown. The inclined current that occurred from the reverse bias characteristic can be utilized as the indicator to detect the hotspot.

Therefore, to answer the main problem statement, the analysis of the characteristic curves is used to implement the methods represented as the algorithms. This thesis presents methods for the irradiation estimation, shading detection, global MPPT, and further develop into the hotspot detection method. The achieved analysis and results show a better operation of PV system, with better efficiency enhancement and maintenance.

5.2 Future Works

The proposed global MPPT is tested its performance under steady and rapid change of weather. Future works for the global MPPT include the test of the algorithm under specific weather conditions that is difficult for PV to operate; for instance, snow and rain. Potentially, the investigation of the algorithm with the standalone PV system can be further analyzed in terms of technical and economical perspectives. In other respects, future work for the hotspot is to study on the thermal transfer of the PV cell materials. More understanding of material characteristics can be applied and utilized for improving the temperature estimation technique.

Research Achievements

Research achievements during the doctoral degree course at Shibaura Institute of Technology, as of September 2020.

Journal Articles

[P.1] Gosumbonggot, J.; Fujita, G, "Partial Shading Detection and Global Maximum Power Point Tracking Algorithm for Photovoltaic with the Variation of Irradiation and Temperature", *Energies 2019, 12, 202*

[P.2] Gosumbonggot, J.; Fujita, G, "Global Maximum Power Point Tracking under Shading Condition and Hotspot Detection Algorithms for Photovoltaic Systems", *Energies 2019, 12, 882*

[P.3] Gosumbonggot, J.; Fujita, G, "Hotspot and Partial Shading Detection Algorithm for the Photovoltaic System Measured in Cell's Scale", *SEATUC Journal of Science and Engineering (SJSE), 2019*

International Conference Proceedings

[P.1] Gosumbonggot, J.; Fujita, G. "Power Dissipation Analysis of the Hotspot Cell in the Photovoltaic Module", in *Proc, of 2020 South East Asian Technical University Consortium Symposium (SEATUC 2020)* Bangkok, Thailand, February 2020

[P.2] Gosumbonggot, J.; Fujita, G, "Photovoltaic's Hotspot and Partial Shading Detection Algorithm Using Characteristic Curve's Analysis ", in *Proc, The*

2019 9th International Conference on Power and Energy Systems (ICPES) Perth, Australia, December 2019 **(Student Travel Award) (Selected Paper for *IET Renewable Power Generation)***

[P.3] Gosumbonggot, J.; Fujita, G, "The Algorithm to Detect and Differentiate Line-Line and Shading fault in PV System", in *The 3rd IEEE ICDCM (International Conference on DC Microgrids)* Matsue, Japan, May 2019

[P.4] Gosumbonggot, J.; Fujita, G, "The Algorithm of Hotspot Detection for Series-Parallel Connected PV Array", in *2019 South East Asian Technical University Consortium Symposium (SEATUC 2019)* Hanoi, Vietnam, March 2019 **(Best Paper Award)**

[P.5] Gosumbonggot, J.; D.D. Nguyen; Fujita, G, "Partial Shading and Global Maximum Power Point Detections Enhancing MPPT for Photovoltaic Systems Operated in Shading Condition", *53rd International Universities Power Engineering Conference (UPEC 2018)* Glasgow, United Kingdom, September 2018 **(Selected Paper for *Energies Special Issue: UPEC2018)***

[P.6] Gosumbonggot, J.; Fujita, G, "Global Maximum Power Point Tracking Algorithm for Photovoltaic Systems operated in Shading Condition with Variation of Irradiation and Temperature", *Vietnam-Japan Scientific Exchange Meeting (VJSE)* Sendai, Japan, September 2018 **(Best Oral Presentation Award)**

[P.7] Gosumbonggot, J.; D.D. Nguyen; Fujita, G, "Short-ranged Maximum Power Point Tracking Algorithm for Series Connected Photovoltaics in Partial Shading Situation", *2018 South East Asian Technical University Consortium Symposium (SEATUC 2018)* Yogyakarta, Indonesia, March 2018

References

[1] International Renewable Energy Agency. Available online: https://www.iea.org/topics/renewables/solar (accessed on 26 July 2019).

[2] New Energy and Industrial Technology Development Organization. Available online: https://www.nedo.go.jp/content/100884812.pdf (accessed on 26 July 2019).

[3] Asian Insiders. Available online: https://asianinsiders.com/japan-renewable-energy/ (accessed on 14 March 2020).

[4] H. Patel ; V. Agarwal. MATLAB-Based Modeling to Study the Effects of Partial Shading on PV Array Characteristics. *IEEE Trans on Energy Conversion.* **2008**, *23*, 302-310.

[5] International Electrotechnical Commission. IEC 61215-1:2016 Terrestrial photovoltaic (PV) modules - Design qualification and type approval - Part 1: Test requirements. *International Electrotechnical Commission* **2006**

[6] Solar Review. Available online: https://review.solar/solar-panel-hot-spot/ (accessed on 4 January 2020).

[7] D. S. Pillai; N. Rajasekar, A comprehensive review on protection challenges and fault diagnosis in PV systems. *Renewable and Sustainable Energy Reviews*, **2018** *91*, pp. 2855-2864

[8] M. Dhimish; P. Mather; V. Holmes, Evaluating Power Loss and Performance Ratio of Hot-Spotted Photovoltaic Modules. *IEEE Transaction on Electron Devices*, **2018** *65*, pp 5419-5427

[9] N. Femia; G. Lisi; G. Petrone; G. Spagnuolo ; M. Vitelli. Distributed maximum power point tracking of photovoltaic arrays: Novel approach and system analysis. *IEEE Transactions on Industrial Electronics* **2008**, *55*, 2610-2621.

[10] L. Gao; R. A. Dougal; S. Liu ; A. P. Iotova. Parallel-Connected Solar PV System to Address Partial and Rapidly Fluctuating Shadow Conditions. *IEEE Transactions on Industrial Electronics* **2009**, *56*, 1548-1556.

[11] Eftichios K. A New Technique for Tracking the Global Maximum Power Point of PV Arrays Operating Under Partial-Shading Conditions. *IEEE Journal of Photovoltaics* **2012**, *2*, 184-190.

[12] S. Daraban ; D. Petreus ;C. Morel ;M. Machmoum. A novel global MPPT algorithm for distributed MPPT systems. *2013 15th European Conference on Power Electronics and Applications (EPE)* **2013**, 1-10

[13] K. S. Tey ; S. Mekhilef. Modified Incremental Conductance Algorithm for Photovoltaic System Under Partial Shading Conditions and Load Variation. *IEEE Transactions on Industrial Electronics* **2014**, 5384-5392

[14] Y. Ji; D. Jung; C. Won; B. Lee ; J. Kim. Maximum power point tracking method for PV array under partially shaded condition. *2009 IEEE Energy Conversion Congress and Exposition* **2009**, 307-312

[15] T. L. Nguyen ; K. Low. A Global Maximum Power Point Tracking Scheme Employing DIRECT Search Algorithm for Photovoltaic Systems. *IEEE Transactions on Industrial Electronics* **2010**, 3456-3467

[16] D. Sera; L. Mathe; T. Kerekes; S.; V. Spataru ; R. Teodorescu. On the Perturb-and-Observe and Incremental Conductance MPPT Methods for PV Systems. *IEEE Journal of Photovoltaics* **2013**, 1070-1078

[17] B. Subudhi ; R. Pradhan. A Comparative Study on Maximum Power Point Tracking Techniques for Photovoltaic Power Systems. *IEEE Transactions on Sustainable Energy* **2013**, *4*, 89-98

[18] M. Miyatake; M. Veerachary; F. Toriumi; N. Fujii ; H. Ko. Maximum Power Point Tracking of Multiple Photovoltaic Arrays: A PSO Approach. *IEEE Transactions on Aerospace and Electronic Systems* **2011**, 367-380

[19] E. Koutroulis; F. Blaabjerg. A New Technique for Tracking the Global Maximum Power Point of PV Arrays Operating Under Partial-Shading Conditions. *IEEE Journal of Photovoltaics, vol. 2, no. 2* **2012**, 184-190

[20] P. Lei; Y. Li; J. E. Seem. Sequential ESC-Based Global MPPT Control for Photovoltaic Array With Variable Shading. *IEEE Transactions on Sustainable Energy, vol. 2, no. 3* **2011**, 348-358

[21] R. Alik; A. Jusoh ; N. A. Shukri. An improved perturb and observe checking algorithm MPPT for photovoltaic system under partial shading condition . *2015 IEEE Conference on Energy Conversion (CENCON)* **2015**

[22] A. Kapic; Ž. Zecevic;B. Krstajic. An efficient MPPT algorithm for PV modules under partial shading and sudden change in irradiance. *2018 23rd International Scientific-Professional Conference on Information Technology (IT)* **2018**

[23] M. E. Bas¸og lu ; B. Çakir. Experimental evaluations of global maximum power point tracking approaches in partial shading conditions . *2017 IEEE International Conference on Environment and Electrical Engineering and 2017 IEEE Industrial and Commercial Power Systems Europe (EEEIC / I&CPS Europe)* **2017**

[24] Spataru Sergiu Amoiridis; Anastasios, Beres; Remus, Ciontea; Catalin-Iosif Klein, Theo; Sera Dezso. Development of an intelligent maximum power point tracker using an advanced PV system test platform. *Conference Record of the IEEE Photovoltaic Specialists Conference*, **2013** 2953-2958

[25] ABB. Available online: https://library.e.abb.com/public/10bc5e66068c4f768a1d77fd853a7e4e/PVI-3.0-3.6-4.2BCD.00374ENRevG (accessed on 6 October 2018)

[26] SMA. Available online: http://files.sma.de/dl/15330/SB5000TL-21-DEN1551-V20web.pdf (accessed on 8 October 2018)

[27] Hiren P. MaximumPower Point Tracking Scheme for PV Systems Operating Under Partially Shaded Conditions . *IEEE Transactions on Industrial Electronics* **2018**, 1689-1698

[28] Jubaer A. An Enhanced Adaptive P&O MPPT for Fast and Efficient Tracking Under Varying Environment . *IEEE Transactions on Industrial Electronics* **2008**, 1689-1698

[29] Korey Sener P. A New MPPT Method for PV Array System Under Partially Shaded Conditions . *3rd International Symposium on Power Electronics for Distributed Generation Systems (PEDG)* **2012**, 437-441

[30] K. Kobayashi; I. Takano ; Y. Sawada. A study on a two stage maximum power point tracking control of a photovoltaic system under partially shaded insolation conditions. *2003 IEEE Power Engineering Society General Meeting* **2003**, 2612-2617

[31] K. Irisawa; T. Saito; I. Takano; Y. Sawada. Maximum power point tracking control of photovoltaic generation system under non-uniform insolation by means of monitoring cells . *Conference Record of the Twenty-Eighth IEEE Photovoltaic Specialists Conference - 2000* **2000**, 1707-1710

[32] B. Bekker ; H. J. Beukes. Finding an optimal PV panel maximum power point tracking method . *C2004 IEEE Africon. 7th Africon Conference in Africa* **2004**, 1125-1129

[33] D. Nguyen ; B. Lehman. An Adaptive Solar Photovoltaic Array Using Model-Based Reconfiguration Algorithm . *IEEE Transactions on Industrial Electronics* **2008**, 2644-2654

[34] R. Gules; J. D. P. Pacheco; H. L. Hey ; J. Imhoff. A Maximum Power Point Tracking System With Parallel Connection for PV Stand-Alone Applications. *IEEE Transactions on Industrial Electronics* **2008**, 2674-2683

[35] X. Yuan; D. Yang ; H. Liu. MPPT of PV system under partial shading condition based on adaptive inertia weight particle swarm optimization algorithm . *2015 IEEE International Conference on Cyber Technology in Automation, Control, and Intelligent Systems (CYBER)* **2015**, 2674-2683

[36] K. Ishaque; Z. Salam. A Deterministic Particle Swarm Optimization Maximum Power Point Tracker for Photovoltaic System Under Partial Shading Condition. *IEEE Transactions on Industrial Electronics* **2013**, 3195-3206

[37] B. N. Alajmi; K. H. Ahmed; S. J. Finney ; B. W. Williams. A Maximum Power Point Tracking Technique for Partially Shaded Photovoltaic Systems in Microgrids. *IEEE Transactions on Industrial Electronics* **2013**, 1596-1606

[38] Karim D. Backstepping sliding mode control for maximum power point tracking of a photovoltaic system. *Electric Power Systems Research* **2017**, *143*, 182-188

[39] Alireza R. Global Maximum Power Point Tracking Method for Photovoltaic Arrays Under Partial Shading Conditions. *IEEE Transaction on Industrial Electronics* **2017**, *64*, 2855-2864, doi: 10.1109/TIE.2016.2632679

[40] S. Moballegh ; J. Jiang. Modeling, Prediction, and Experimental Validations of Power Peaks of PV Arrays Under Partial Shading Conditions. *IEEE Transactions on Sustainable Energy* **2014**, 293-300, doi: 10.1109/TSTE.2013.2282077

[41] Mohammad Amin G. Partial Shading Detection and Smooth Maximum Power Point Tracking of PV Arrays Under PSC. *IEEE Transactions on Power Electronics* **2016**, *31*, 6281-6292, doi: 10.1109/TPEL.2015.2504515

[42] Y. Wang. High-Accuracy and Fast-Speed MPPT Methods for PV String Under Partially Shaded Conditions. *IEEE Transaction on Industrial Electronics* **2016**, *63*, doi: 10.1109/TIE.2015.2465897

[43] J. Ahmed. An accurate method for MPPT algorithm to detect the Partial shading Occurrence in a PV system. *IEEE transaction on industrial informatics* **2017**, *13*, doi: 10.1109/TII.2017.2703079

[44] R. Y. Kim. An improved global maximum power point tracking scheme under partial shading conditions. *Int. Conf. Electr. Mach. Syst.* **2013**, *2*

[45] A. Ramyar. Global maximum power point tracking method for photovoltaic arrays under partial shading conditions. *IEEE Trans. Ind. Electron.* **2017**, *64*, doi: 10.1109/TIE.2016.2632679

[46] L. Yi-Hwa. A particle swarm optimization-based maximum power point tracking algorithm for PV systems operating under partially shaded conditions. *IEEE Trans. Energy Convers.* **2012**, *27*, doi: 10.1109/TEC.2012.2219533

[47] M. Seyedmahmoudian. Simulation and hardware implementation of new maximum power point tracking technique for partially shaded PV system using hybrid DEPSO method. *IEEE Trans. Sustain. Energy* **2015**, *6*, doi: 10.1109/TSTE.2015.2413359

[48] Carrasco M.; Laudani A.; Lozito G.M.;Mancilla-David; F. Riganti Fulginei; Salvini A. Low-Cost Solar Irradiance Sensing for PV Systems *Energies* **2017**

[49] H.Huang. Cloud motion estimation for short term solar irradiation prediction. *2013 IEEE International Conference on Smart Grid Communications. (SmartGridComm)* **2013**

[50] Gosumbonggot, J.; Fujita, G. Partial Shading Detection and Global Maximum Power Point Tracking Algorithm for Photovoltaic with the Variation of Irradiation and Temperature. *Energies* **2019**, *12*, 202

[51] B. N. Alajmi; K. H. Ahmed; S. J. Finney ; B. W. Williams. A Maximum Power Point Tracking Technique for Partially Shaded Photovoltaic Systems in Microgrids. *IEEE Transactions on Industrial Electronics* **2013**, 1596-1606

[52] L. Gao; R. A. Dougal; S. Liu ; A. P. Iotova. Parallel-Connected Solar PV System to Address Partial and Rapidly Fluctuating Shadow Conditions *IEEE Transactions on Industrial Electronics* **2009**, 1548-1556

[53] D. S. Pillai ; N. Rajasekar. A comprehensive review on protection challenges and fault diagnosis in PV systems. *Renewable and Sustainable Energy Reviews* **2018**, 18-40

[54] J.Gosumbonggot; G. Fujita, Partial Shading and Global Maximum Power Point Detection Enhancing MPPT for Photovoltaic Systems Operated in Shading Condition. *2018 53rd International Universities Power Engineering Conference (UPEC)* **2018**, doi: 10.1109/UPEC.2018.8541880

[55] Mathworks, Average Model of a 100-kW Grid-Connected PV Array. Available online: https://www.mathworks.com/help/physmod/sps/examples/average-model-of-a-100-kw-grid-connected-pv-array.html (accessed on 21 June 2020)

[56] Monroe Infrared, PV (Photo-voltaic or Solar Panel) Safety & Operational Inspections. *Monroe Infrared Technology*, **2017**

[57] Mani G; Tamizh-Mani. Failure and Degradation Modes of PV Modules in a Hot Dry Climate; *NREL Golden, CO, USA 2018.* Available online https://www.energy.gov/sites/prod/files/2014/01/f7/pvmrw13_openingsession_asu_mani.pdf (accessed on 4 January 2019).

[58] Salazar, M. Hotspots Detection in Photovoltaic Modules Using Infrared Thermography. *In Proceedings of the ICMIT 2016, Bangkok, Thailand* **2016**, *5*, 19–22.

[59] P. Bharadwaj; K. Karnataki ;V. John. Formation of Hotspots on Healthy PV Modules and Their Effect on Output Performance. *2018 IEEE 7th World Conference on Photovoltaic Energy Conversion (WCPEC) (A Joint Conference of 45th IEEE PVSC, 28th PVSEC & 34th EU PVSEC), Waikoloa Village, HI* , **2018**, 676-680.

[60] S. Deng ; Z.Zhang; C. Ju; J. Dong ; Z. Xia; X. Yan; T. Xu; G. Xing. Research on hot spot risk for high-efficiency solar module. *Energy Procedia vol. 130*, **2017**, 77-86

[61] U. Hoyer; A. Burkert; R. Auer ;C. Buerhop-Lutz. Analysis of PV Modules by Electroluminescence and IR Thermography. *Proceedings of: 24th European Photovoltaic Solar Energy Conference and Exhibition - EUPVSEC* **2009**.

[62] A. Luque ;S. Hegedus. Handbook of Photovoltaic Science and Engineering. *in Chichester U.K.:Wiley-Interscience* **2003** 297-299

[63] M. Simon; E. L. Meyer. Detection and Analysis of Hot-spot Formation in Solar Cells. *Solar Energy Materials & Solar Cells vol. 94 no. 2* **2010** 106-113

[64] B. Hossam ; K. Itako. Real time hotspot detection using scan-method adopted with P&O MPPT for PV generation system. *16 IEEE 2nd Annual Southern Power Electronics Conference (SPEC)* **2016** 1-5

[65] J. Qian; C. E. Clement; M. Ernst; Y. S. Khoo; A. Thomson; A. Blakers. Analysis of Hotspots in Half Cell Modules Undetected by Current Test Standards. *in IEEE Journal of Photovoltaics vol. 9, no. 3* **2019** 842–848

[66] K. A. Kim; C. Xu; L. Jin; P. T. Krein. A Dynamic Photovoltaic Model Incorporating Capacitive and Reverse-Bias Characteristics" *in IEEE Journal of Photovoltaics, vol. 3, no. 4* **2013** pp. 1334-1341

[67] Rossi, D.; Omana, M.; Giaffreda, D.; Metra, C. Modeling and Detection of Hotspot in Shaded Photovoltaic Cells. *IEEE Trans. Very Large Scale Integr. (VLSI) Syst.* **2015**, *23*, 1031–1039.

[68] Yang, S.; Itako, K.; Kudoh, T.; Koh, K.; Ge, Q. Monitoring and Suppression of the Typical Hot-Spot Phenomenon Resulting From Low-Resistance Defects in a PV String. *IEEE J. Photovolt.* **2018**, *8*, 1809–1817.

[69] Alsafasfeh, M.; Abdel-Qader, I.; Bazuin, B. Fault detection in photovoltaic system using SLIC and thermal images. In Proceedings of the *2017 8th International Conference on Information Technology (ICIT), Amman, Jordan* **2017**; pp. 672–676

[70] Dong, F.; Hou, M.; Feng, H.; Jin, Z.; Tian, J. Research on the reconstruction method of PV module based on the door connection. In Proceedings of the *2016 IEEE PES Asia-Pacific Power and Energy Engineering Conference (APPEEC), Xi'an, China* **2016**; pp. 337–341.

[71] S., Roy; R., Gupta. Quantitative Estimation of Shunt Resistance in Crystalline Silicon Photovoltaic Modules by Electroluminescence Imaging in *IEEE Journal of Photovoltaics, vol. 9, no. 6, pp. 1741-1747*, **Nov. 2019**

[72] Wohlgemuth, J.; Herrmann, W. Hot spot tests for crystalline silicon modules. *In Proceedings of the Conference Record of the Thirty-First IEEE Photovoltaic Specialists Conference, Lake Buena Vista, FL, USA* **2005**; pp. 1062–1063.

[73] PVEducation. Available online: https://www.pveducation.org/pvcdrom/modules/modules-structure (accessed on 7 January 2019).

[74] K. A. Kim; P. T. Krien, Photovoltaic hot spot analysis for cells with various reverse-bias characteristics through electrical and thermal simulation. *2013 IEEE 14th Workshop on Control and Modeling for Power Electronics (COMPEL), Salt Lake City, UT* **2013**, 1–8.

[75] P. Bharadwaj; K. Karnataki ; V. John, Formation of Hotspots on Healthy PV Modules and Their Effect on Output Performance. *2018 IEEE 7th World Conference on Photovoltaic Energy Conversion (WCPEC) (A Joint Conference of 45th IEEE PVSC, 28th PVSEC & 34th EU PVSEC), Waikoloa Village, HI* **2018** , 0676–0680.

[76] S. Silvestre; A. Boronat; A. Chouder. Study of bypass diodes configuration on PV modules. *Applied Energy* **2009** , *86*, 1632–1640.

[77] Olalla, C.; Hasan, M.; Deline, C.; Maksimović, D. Mitigation of Hot-Spots in Photovoltaic Systems using Distributed Power Electronics. *Energies* **2018**, *11*, 726.

[78] K. A. Kim ;P. T. Krein; G. Seo; B. Cho. Photovoltaic AC parameter characterization for dynamic partial shading and hot spot detection. *2013 Twenty-Eighth Annual IEEE Applied Power Electronics Conference and Exposition (APEC)*, **2013**, 109-115.

[79] P. Sanchez-Friera; M. Piliougine; J. Pelaez; J. Carretero; M. S. de Cardona. Analysis of degradation mechanisms of crystalline silicon pv modules after 12 years of operation in southern europe. *Progress in Photovoltaics: Research and Applications*, **2011**, *vol. 19*, 658-666

[80] S. Armstrong; W.G. Hurley. A thermal model for photovoltaic panels under varying atmospheric conditions. *Applied Thermal Engineering* **2010** , *30*, 1488-1495

[81] K. A. Kim; P. T. Krien, Reexamination of Photovoltaic Hot Spotting to Show Inadequacy of the Bypass Diode. *IEEE Journal of Photovoltaics* **2015**, *5*, 1435–1441.